Spectral Time Domain Induced Polarization - Factors Affecting Spectral Data Information Content and Applicability to Geological Characterization

Azadeh Rezvani

Dissertations in Geology at Lund University,
Master's thesis, no 433
(45 hp/ECTS credits)

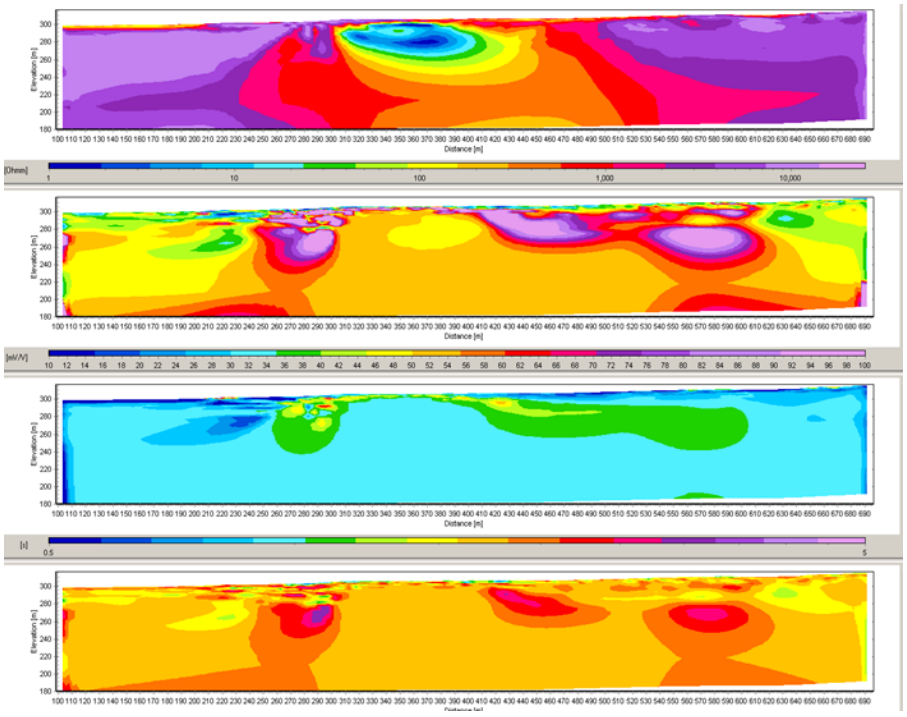

Department of Geology
Lund University
2015

Spectral Time Domain Induced Polarization - Factors Affecting Spectral Data Information Content and Applicability to Geological Characterization

Master's thesis

Azadeh Rezvani

Department of Geology
Lund University
2015

Contents

Cover Picture: Inversion models of resistivity, chargeability, Tau and C form one of the measurments of this survey in AarhusInv software. Azadeh Rezvani

Spectral Time Domain Induced Polarization - Factors Affecting Spectral Data Information Content and Applicability to Geological Characterization

AZADEH REZVANI

Rezvani, A., 2015: Spectral Time Domain Induced Polarization - Factors Affecting Spectral Data Information Content and Applicability to Geological Characterization. *Dissertations in Geology at Lund University*, No. 433, 38 pp. 45 hp (45 ECTS credits).

Abstract: The geo-electrical survey (resistivity and induced polarization) with different settings, arrangements, time base, spreads and waveforms (50% and 100% duty cycle waveform) was carried out over the Liikavaara deposit, near the Aitik mine, in northern Sweden and all the measured data was inverted in two different softwares: Res2Dinv and AarhusInv. Surveys of induced polarization (IP) often contain data of low quality, due to the high sensitivity against noise sources and coupling effects. Measured data with the new method (applying 100% duty cycle waveform), which is much faster than the conventional one (50% duty cycle waveform), present significant improvements in the quality of IP-data. It was also attempted to increase the data quality by separating current and potential cables and restrict the capacitive coupling, which normally occurs between transmitting current and potential receiving wires. Moreover, conceptual models from different measurements were correlated to boreholes close to the survey line, in order to find geological correlation between the models and logging data. There was also a possibility of modeling Tau and C parameters by the newly developed software (AarhusInv) which gave us more detailed information about the mineralization texture (grain size and grain size distribution). They were also compared in different measurements and it appears that Tau and C are sensitive to the duration of current injection. However, lack of reference data for interpretation, made the interpretation of these two parameters, difficult and ambiguous.

Keywords: Resistivity, Induced polarization, Geophysics, Geology, Liikavaar, AarhusInv.

Supervisors: Torleif Dahlin, Ulf Söderlund, Paal Ahnfelt (Boliden Mineral AB) and Per-Ivar Olsson (LTH)

Subject: Geophysics and Bedrock Geology

Azadeh Rezvani, Department of Geology and Engineering Geology, Lund University, Sölvegatan 12, SE-223 62 Lund, Sweden. Email: azaderezvani@yahoo.com

Spektral tidsdomän inducerad polarisation - faktorer som påverkar spektralt informationsinnehåll och tillämpningar för geologisk karakterisering

AZADEH REZVANI

Rezvani, A., 2015: Spektral tidsdomän inducerad polarisation - faktorer som påverkar spektralt informationsinnehåll och tillämpningar för geologisk karakterisering. *Examensarbeten i geologi vid Lund University*, Nr. 433, 38 sid. 45 hp.

Sammanfattning: Geoelektrisk undersökning (resistivitet och inducerad polarisation) med olika mätinställningar, elektrodkabelutlägg, mätkonfigurationer och vågform (50 % och 100 % arbetscykel vågform) genomfördes i Liikavaara område, nära Aitikgruvan i norra Sverige. Alla uppmätta data inverterades i två olika programvaror: Res2Dinv och AarhusInv. Mätningarna av inducerad polarisation (IP) resulterade i data av varierande kvalitet, på grund av metodens höga känslighet för brus och andra störningar. Uppmätta data med den nya metoden (100% arbetscykel vågform) medförde tydliga förbättringar avseende kvaliteten på IP-data. Dessutom är mätningen med 100% arbetscykel vågform mycket snabbare än den konventionella tekniken med 50% arbetscykel vågformen. För att ytterligare försöka öka datakvaliteten användes separata ström- och potentialkabelutlägg för att begränsa den kapacitiva kopplingen som normalt uppstår mellan sändande ström- och mottagande potentialledare. För att finna geologiska samband mellan modeller och loggningsdata korrelerades förväntningsmodeller från de olika mätningarna till borrhål nära undersökningslinjen. Det fanns en möjlighet att också modellera parametrarna Tau och C i den nyutvecklade programvaran (AarhusInv), vilket resulterar i mer nyanserad information relaterad till mineraliseringens textur (kornstorlek och kornstorleksfördelning). Dessvärre är referensuppgifterna för dessa två parametrar bristfälliga, vilket gör att det inte går att utvärdera hur väl det kopplar till geologin varför tolkningen blir osäker.

Nyckelord: Resistivitet, inducerad polarisation, geofysik, geologi, Liikavaara, AarhusInv .

Handeledare: Torleif Dahlin, Ulf Söderlund, Paal Ahnfelt (Boliden Mineral AB) and Per-Ivar Olsson (LTH)

Ämnesinriktning: Geofysik och berggrundsgeologi

Azadeh Rezvani, Geologiska institutionen, Lunds Universitet, Sölvegatan 12, 223 62 Lund, Sverige.
E-post: azaderezvani@yahoo.com

1. Introduction

1.1 Background

Sweden has a long history in mining and exploration. The Malmfälten ore district in the northern part of Norrbotten hosts one of the largest deposits of iron and copper. The Kiruna mine, which is classified as an apatite-iron deposit, and the Aitik porphyry copper-gold deposits are well-known mining districts in northern Sweden. The Aitik area is located approximately15 km southeast of the Gällivare iron-ore field and covers an area of around 80 km^2 (Estholm, 2014).

Two deposit types exist in the Aitik field: the Aitik deposit (currently mined as an open pit) and Liikavaara (not in production), which located 4 km east of Aitik and also is the focus of this survey. These two deposits differ substantially in physical properties. Whilst Aitik is properly disseminated, the Liikavaara appears to be significantly more massive (Malmqvist and Parasins, 1972). However, the Aitik mine covers distinctively larger area compared to the planed open pit mine in Liikavaara.

Geophysical exploration work in the Aitik area started in 1930's and a variety of methods were used for mineral prospection. The Aitik and Liikavaara deposits were discovered by Boliden in 1932 and the Aitik mine came into production in 1968. (Malmqvist and Parasins, 1972).

Ore in the Atik field is dominantly disseminated-copper with weak impregnations of pyrite and chalcopyrite in a gneissic host rock (Malmqvist and Parasins, 1972) and the goal of this survey is to test the electrical survey with different setups and applying two different types of waveforms (50% and 100% duty cycle waveform) over the mineralization zone and the host rock in Liikavaara. Since the conventional way of electrical measurements (applying 50% duty cycle waveform) are time consuming, the possibility of applying the new method (applying 100% duty cycle waveform) can be very efficient and fast in the field investigations, thus both methods are tested and compared in this study.

Both types of wave forms and the other detailed setups are described in the 'Method' section.

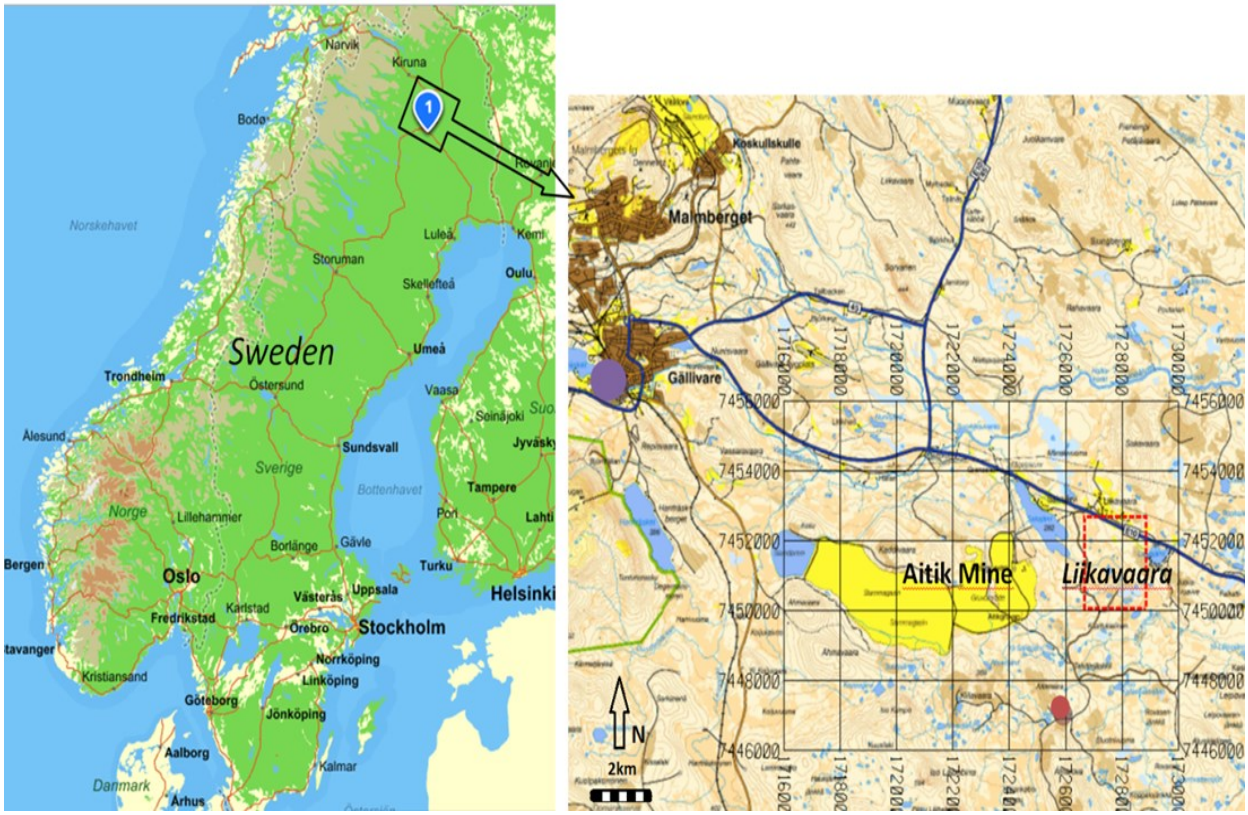

Fig. 1. Aitik ore field including the Aitik mine and Liikavaara deposit in the northern part of Norrbotten-North Sweden (Boliden AB, 2014; kartor.eniro.se) .

1.2 Aim of the project

The aim of this project is to test different electrical survey set-ups across the Liikavaara mineralization in order to answer the following questions:

- Is it possible to reduce the acquisition time by measuring the IP during the on time (applying 100% duty cycle waveform instead of 50% duty cycle wave form) whilst maintaining good data across the mineralization?
- Does separating current and potential cables reduce noise caused by coupling mechanisms?
- Is it possible to enhance data quality by applying different time base for the waveform?
- Is it possible to ascribe a certain geophysical signature to the geology along the survey line?

The tests include Resistivity and Spectral Time-Domain-Induced Polarization with the following setup:

- Single cable spread and separated cable spreads
- Different time base 1s, 2s, 4s for current on and off (only for multiple gradient array)
- Using different waveforms for IP measurement: 50% duty cycle waveform (standard IP mode) and 100% duty cycle waveform (Terrameter LS resistivity mode).

1.3 Study area

The study area is located near the village known as Liikavaara, ca. 16 km southeast of town Gällivare. The Liikavaara Cu-Au deposit is located just south of this village, on the other side of road E10 (Figure 2).

Figure 2. Liikavaara area located in 3 km northeast of the

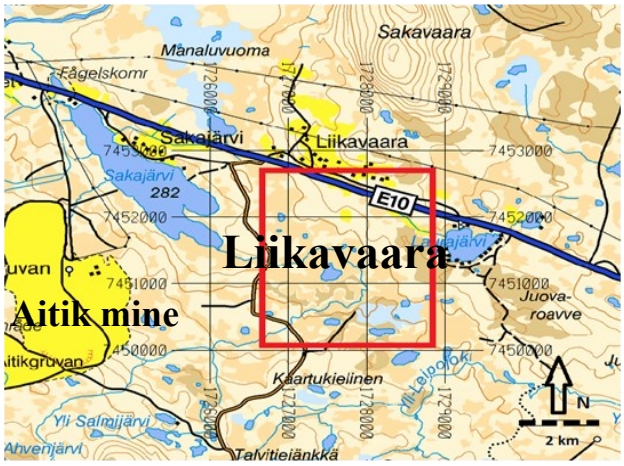

Aitik mine. The red square shows the Liikavaara district

(Boliden AB, 2014).

The area has poor access to outcrops due to extensive overburden coverage (glacial till and swamps) and is therefore dominated by flat topography. The deposit has previously been surveyed using different geophysical techniques such as EM (Electromagnetic Methods) and IP (Induced Polarization). In 2013, the consultant company Geovista carried out both refraction seismic and resistivity/IP surveys in order to construct a 3D model of possible deformation zones (Mattsson and Thunehed, 2013). In Figure 3, the outline of the planned open pit is marked with a yellow polygon and Geovista's survey lines are shown in red (resistivity) and green (refraction seismics).

The survey line selected for this thesis work was line number 3, as this line was the easiest accessible and still covered a central part of the mineralization. Processing and modeling of the measured data along this 800 m line were performed in softwears; Res2Dinv and AarhusIn / Workbench .

Figure 3. The outline of planned open pit mine in Liikavaara (yellow polygon) and the Geovista's survey lines in red (resistivity) and green (refraction seismic). Line 3 is selected for this study and correspondence to length of 800 m. Red dots are representing the existing boreholes (Mattsson and Thunehed, 2013)

2. Geology

2.1 Regional geology and setting

County Norrbotten is a central mining province dominated by Fe- and Cu- deposits. The bed rock was formed during the middle Precambrian (2.8 -2.7 Ga) (Estholm, 2014).

The mineral deposits mainly occurred in volcanoclastic units related to 1.9 Ga Svecofennian and the middle-upper part of the 2.2-2.0 Ga Karelian greenstones, which includes the base metal sulphide deposits (Cu, Zn-Pb) and iron formation (Wanhainen, 2005).The Norrbotten Archean basement rocks are dominated by granitoid gneisses overlain by Paleoproterozoic greenstones, porphyries and sedimentary successions (Martinsson, 2004) .The large scale tectonism in the north Sweden has a complex history of repeated extensional and compressional tectonic events associated with magmatic and metamorphic events. The main events are:

1. Extension connected to Karelian continental rifting event at ca. 2.1 Ga which generated the deep crustal scale fault systems and extensive areas of rift -related basalts.

2. Repeated events of *Svecofennian* large-scale deformation, from 1.93 till 1.87 Ga, including subduction and creation of oceanic island arcs which led to strong reworking of older crust and generation of juvenile crust. Specifically in the northern Norbotten the calc-alkaline, andesite dominated volcanic succession, such as the *Porphyrite Group*, and the comagmatic intrusive Haparanda Suite represent *Svecofennian* arc magmatic activity (Wanhainen, 2005).

The main events of deformation and metamorphism of thick volcanic and sedimentary rocks occurred first at 1.88 Ga and then at 1.80-1.79 Ga. The metamorphic grade varies from upper greenschist to upper amphibolites facies at low to intermediate pressures (Wanhainen et al., 2012).

2.2 Local geology (the Aitik field)

Based on the structural boundaries and the copper grade, the Aitik deposit is divided into three main sections: footwall, ore zone and hanging wall. The hanging wall is mainly composed of feldspar-biotite-amphibolite rocks with no signs of mineralization. The ore zone consists of garnet-biotite schist towards the footwall and quartz- muscovite sercite schist towards the hanging wall. The hanging wall and ore zone are separated by a thrust. The footwall comprises quartz monzodiorite, micro-quartz monzodiorite and feldspar-biotite-amphibole gneiss

The majority of rocks in the Aitik deposit belong to two groups of igneous units:

The Haparanda suite which is formed in a volcanic arc setting during the subduction of oceanic crust beneath the Archean Craton at ca. 1.9 Ga and the Porphyrite group which is considered comagmatic with the Haparanda suite. Both groups have later been metamorphosed at amphibolite facies to schist and gneiss (Wanhainen, 2005).

2.2.1 Origin and Cu-Au deposits types in Aitik

The Aitik deposit was first classified as being of sedimentary origin (Zweifel, 1976). Later studies by (Monro, 1988) suggested that the deposit is a porphyry copper type of a magmatic–hydrothermal origin. However, Wanhainen (2005) has proposed that it might have a more complex origin since not all the features of the ore zone are typical for porphyry type.

Magmatic hydrothermal Cu-Au ore bodies generally can be classified as two main types:

Porphyry-type deposits which are mostly attributed to subduction- related island arcs or continental margin settings, and distributed in time from Archean to present. The common mineralization style in these types are disseminated, vein and quartz stockwork and the main host rocks are intermediate porphyritic intrusions and intermediate volcanic/sedimentary rocks.

IOCG-type (iron oxide-copper-gold) deposits could form in various geological settings with associated alteration and mineralization processes. However, Hitzman (2000) has considered two principle tectonic environments for these deposits: intra-continental orogenic collapse/magmatism and extension along a subduction-related continental margin. IOCG deposits are typically Archean to Pliocen in age and associated with oxidized igneous activity. The main host rocks are felsic-intermediate volcanic /sedimentary rocks and felsic intrusions (Wanhainen, 2005).

Wanhaine (2005) proposed that the Aitik deposit represents metamorphosed Palaeoproterozoic *porphyry copper deposit* that was affected ca.100 Myr later during a regional *IOCG-type hydrothermal* event. This interpretation was based on a petrology, mineralogy, fluid inclusion and geochemistry of the intrusive and volcaniclastic rocks in this area. In fact the early porphyry type copper followed by tectonic and metamorphic events (1.8 Ga) which caused releasing of CO_2 and aqueous salinity fluids during these events. These aqueous fluids led to formation of IOCG mineralization and the porphyry copper deposit has been overprinted by IOCG mineralization. Consequently the Aitik deposit is representing a mixed ore system. Moreover extensive Na-Ca alteration during these tectonic events could probably help to extension of copper and gold mineralization in the deposit (Wanhainen et al., 2012).

2.2.2 The Liikavaara Cu-Au deposit

Zweifel (1976) has divided the Liikavaara zone into two units; upper and lower formations. The lower formation is mainly composed of feldspar quartzites, phyllitic feldspar quartzites and congolomerates. The upper unit is characterized by meta-arenites (of greywacke type) and amphibolitic rock.

In the Liikavara deposit, as in the Aitik zone, chalcopyrite ($CuFeS_2$) is the most valuable mineral to the mine.

The ore zone is abundant with chalcopyrite ($CuFeS_2$) and pyrrhotite (Fe_7S_8) and the Cu content generally varies between 0.2 - 1 % on the meter scale, however it may change a lot in some parts and reach up to 5 %. According to Zweifel's (1976) report the mineralized zone has almost the same width from surface down to 240 m but the average grades of Cu content is decreasing with depth.

Galena (PbS) and sphalerite (Zn,Fe)S are also common minerals but the Pb and Zn contents are generally low (below 1%). Pyrite (FeS_2) and magnetite (Fe_3O_4) are less common and magnetite occurs between pyrite and pyrrhotite as a rim around pyrite. Scheelite ($CaWO_4$) is also observed in some parts of the mineralization and is associated with quartz and calcite veinlets. These veinlets are the most common gangue minerals (with varying amounts of sericite, biotite and chlorite) and quartz veinlets cut the Cu mineralization in several parts and continue outside the ore zone. Fluorite, tourmaline and apatite are accessory minerals in the mineralized zone (Zweifel, 1976).

The main Liikavaara mineralization zone occurs within a unit containing predominantly biotite schists, and the bedrock varies to biotite gneisses, biotite quartzite and biotite-amphibole schist or gneisses in different parts. The hanging wall consists of a thick conglomerate unit and the footwall of an andesitic unit with a significant input of turbidites. The mineralized zone sits between the hangingwall / footwall complex, and weakly extends into the footwall.

Zircon and apatite are quite abundant and tourmaline is present disseminated in the bedrock. There is a relatively high Mg and Ca content which suggests the formation of biotite partly by Mg metasomatism (Zweifel, 1976).

2.3 Borehole / log documentation

2.3.1 Core samples

There are some boreholes which are relatively close to our survey line, thus the corresponding cores and borehole loggings are considered as our reference for interpretation and geological correlations. The cores were collected by Boliden AB in 2010. Two of these cores (Core AIA 370 and AIA367) were recently studied in a bachelor project (Estholm, 2014) and documented by graphic logging, thinsections and geochemical sampling. Thus there is an informative documentation with detailed geological characterization on these two boreholes (Estholm, 2014).

Core ***AIA 367:*** This sample is 120 m far from the survey line (7452961 N, 0762540 E; see Figure 3) and it has been collected from the footwall, comprising the interval of 5.7 m to 160 m depth.

Core ***AIA 370:*** This borehole is located 260 m away from our line (7452966 N, 0762128 E; see Figure 3). This core sample is 365 m in length and comprises both the hanging wall and highly altered mineralization zone.

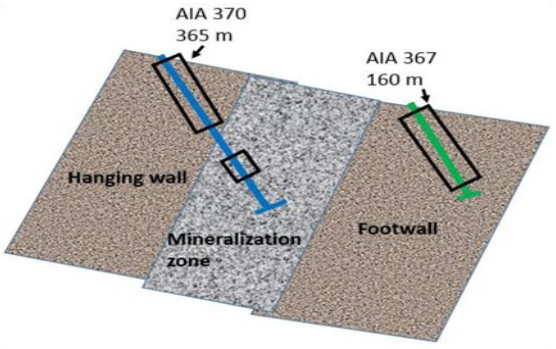

Figure 4. A schematic sketch of the host rock and sampling sections (Estholm, 2014).

2.3.2 Logging data

Logging data are available for all boreholes in this area. Four of them (365, 364, 363, 331), which are quite close to our survey line, are chosen for interpretation and correlation between measured responses and Lithology /mineralogy of the corresponding depth.

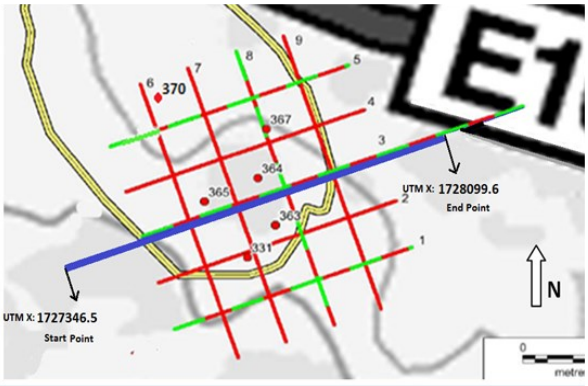

Figure 5. Survey line and the boreholes which are used in this study (Mattsson and Thunehed, 2013).

The lithology, depth and the common structure of borehole 365, 364, 363, 331, 367 and 370, which are marked with red circles in the map (Figure 5), are summarized in the tables 1 to 5 in the appendix.

3. Methods and fundamental concepts

3.1 Resistivity

Resistivity is defined as the ability of materials to act as an isolator in presence of electrical current flow.

Since 1900s the electrical resistivity method is one of the common geophysical survey techniques for determining the subsurface resistivity distribution which is can be useful for different purposes, such as mining industry, geotechnical investigation or environmental studies.

The ground resistivity mainly depends on the geological parameters such as the mineral composition, mineral structure, fluid content, porosity and degree of water saturation in the rock. Normally we have a range of resistivity values for a specific lithology, some of them are illustrated in Figure 6. However, there are some resistivity intervals which are attributed to more than one lithology and this is why the interpretation can be difficult without access to other

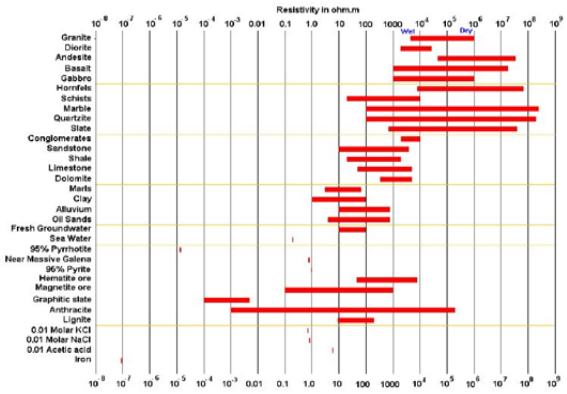

type of data (Loke, 2014; Reynolds, 2011).

Figure 6. Resistivity of some common rocks and minerals (Loke, 2014).

The resistivity measurements are made by injecting an electrical current into the ground through two current electrodes, and then measuring the induced potential-field gradient voltage between two receiver electrodes as it is shown in Figure7. From the known current (I) and the measured voltage (V), resistance (R) will be calculated by Ohm's Law:

R= V / I (3.1.1) Then the apparent resistivity (ρ_a) can be calculated, which is defined as:

$\rho_a = K\ V / I$ or $\rho_a = K\ R$ (3.1.1)

Where ***K*** is the geometric factor and depends on the electrode arrangement (Loke, 2014).

There are three main types of arrays (electrode arrangement) which are common to be used in the resistivity survey; Wenner, Schlumberger and dipole-dipole arrays. Each array has its own geometric factors (Reynolds, 2011).

The depth of investigation is mainly controlled by the distance between the pair of current electrodes and the pair of potential electrodes in which for more penetration, longer distances between current electrodes will be needed, but it should be considered that longer cables can produce undesirable inductive coupling effect, which can affect the data quality (Reynolds, 2011). Different types of coupling effects will be discussed in the *coupling effect* section in more details.

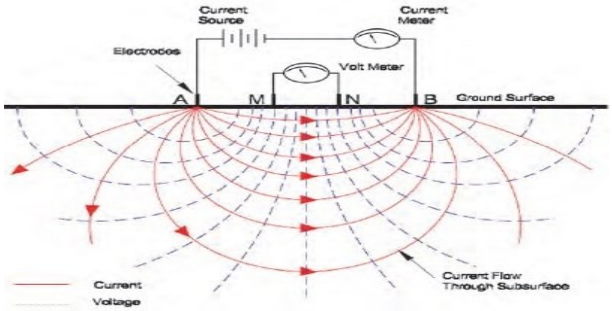

Figure 7. Basic concept of electrical resistivity measurement (Sharma, 1997)

3.2 Induced Polarization

Induced polarization (IP) measurement employs the same method as resistivity but it can also provide information on the energy storage capacity of the medium which is known as *Chargeability* (Butler, 2005). The IP phenomenon was first reported by Conrad Schlumberger in 1913. During resistivity measurement he noticed that when the current was turned off, the potential difference measured between the potential electrodes, did not drop immediately to zero.

First it dropped sharply and then it gradually decayed to zero. In fact the ground gradually discharge the electrically polarized energy and return to equilibrium after a given interval of time, this time interval mainly depends on both instrumental and geological factors, thus it is diagnostic to the nature of subsurface material and rock type (Reynolds, 2011) (Wightman et al., 2003). The main application of IP survey is in mining industry and mineral prospection for disseminated metallic ores, especially porphyry coppers, bedded lead/zinc and sulphide-related gold deposits (Reynolds, 2011).

Butler (2005) provides a list of common IP sources:

1. Metallic luster minerals (Pyrite, chalcopyrite, graphite and galena)
2. Disseminated sulfide
3. Layered silicates
4. Clays and other alteration products (kaolinite, chlorite, ilite, montmorillonite)
5. Organic materials (green waste, anoxic carbon-rich deposits)
6. Other minerals (ilmenite, hematite, etc.)

In the conventional IP measurement which always acquires data with resistivity measurement simultaneously, there are two pairs of current electrodes for introducing current into the ground, then the current will be turned off and two receiver (potential) electrodes will measure the differential voltage during the off time. The resulting voltages as a function of time (time-domain IP), frequency (frequency-domain IP) or phase (phase-domain) will be analyzed as induced polarization effect (Butler, 2005; Reynolds, 2011). However, research and development is in progress regarding the possibility of measuring IP effect during the on-time (Olsson et al., 2014) which will be explained in more details in the *waveform* section.

In general, IP data can be measured in four different modes; frequency domain, time domain, phase domain and spectral IP (Reynolds, 2011)

Time domain IP data are traditionally generated by measuring the rate of decay in the residual potential in the rock/soil after the current pulse has been interrupted. In this work a novel method of measuring time-domain IP during the on-time is also tested.

Frequency domain is defined as the effect of alternating currents with varying the frequency on the measured value of resistivity (Anderson et al., 2008; Wightman et al., 2003), whereas phase domain IP is the usage of phase lag between current and measured potential to distinguish the subsurface minerals.

The spectral IP method in frequency domain comprises measuring of amplitude and phase relationship between the injected current and measured potential over a wide range of frequencies, normally between 10^{-3} Hz to 4 kHz , the result will be a diagnostic IP response spectrum (Butler, 2005; Reynolds, 2011).

If the frequency dependence is plotted as a binary function in the form of logarithms to base 2, the behavior between the lower and upper frequency limits can be defined as the time constant of the IP response which is known as ‘‘relaxation time’’ (Ꞇ) in Cole-Cole model (Fiandaca et al., 2013; Reynolds, 2011).

The time constant, Tau (Ꞇ) and frequency exponent (C) are measurable physical properties which describe the shape of the decay curve. The behavior of Tau and the C will be dictated by the texture of mineralization. The mineralization texture is characterized by the grain size and grain size distribution of the polarisable particles within each group of ore grains and it is not much dependent on the type of metallic mineral which are present in the ore body. For example if the polarisable mineral is coarse grained, the relaxation time (Ꞇ) is larger than the fine grained mineralization. These spectral IP parameters (Ꞇ and C) normally are used to determine the mineralization texture of an orebody and separation of primary mineralization zones (veinlets of ore) from disseminated ore. For example where we have a long zone of sulfide or iron oxide formation, spectral IP can determine where the metal concentration increases based on the variations in the spectral texture and relaxation time (Ꞇ).

Moreover, if we have a pyrite zone, any changes in texture along this zone can indicate the presence of gold, copper or zinc. The C parameter ,with maximum value of 0.5, can be also helpful for distinguishing the massive sulfides and the grain size distribution, for most of the massive sulfide C parameter is in the range of 0.25 -0.35 (Reynolds, 2011).

In this survey we have measured Spectral IP in time-domain which is based on measuring the IP decay in many time windows and inverting the data for the spectral IP parameters (chargeability, Ꞇ and C) in the AarhusInv software.

3.2.1 Chargeability

As is mentioned before, when the injected current to the ground is suddenly ceased, the voltage V_0 between two electrodes drops abruptly to a small polarization voltage Vp and then, gradually to zero. *Chargeability* is formally defined as the polarization voltage (Vp) which is developed across a unit cube of the ground material and it is energized by a unit current. The *apparent chargeability* of the ground is defined as the ratio of Vp / V_0, which is a pure number and does not have any unit, but in order to avoid very small values it is multiplied by a thousand and cited in milivolts per volts (mV/V). It is also possible to measure the area under the decay curve using integration for calculating the apparent chargeability, the result depends on the length of the integration period and delay time, in this case chargeability will be quoted in millisecond (ms) (Milsom and Eriksen, 2011).

Chargeability can be affected by different factors such as grain size, type of material, ion concentration, non-ionic fluids etc. More over there is a wide range of variability which can be expected for different types of rocks or material, implying that it is

difficult to use values of true chargeability obtained by inversion of IP data to determine the exact type of rock in the ground. Therefore, designation of material type just on the basis of chargeability data is not reliable (Jones, 2007). The following tables (Telford et al., 1990; Loke, 2104) provide a general guide to possible chargeability of some different materials.

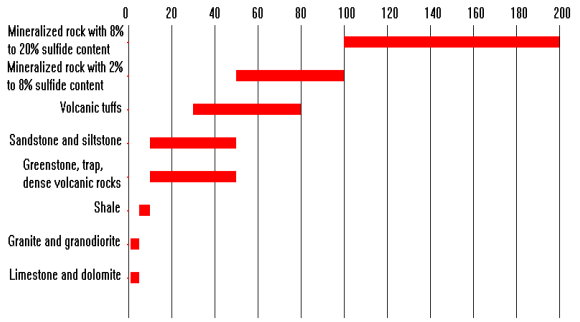

Figure 8. The chargeability values for some rocks and minerals in mV/V (Loke, 2014).

Minerals	Chargeability (ms.)	Chargeability (mV/V)
Pyrite	13.4	13.7
Chalcocite	13.2	13.5
Copper	12.3	12.6
Graphite	11.2	11.4
Chalcopyrite	9.4	9.6
Bornite	6.3	6.4
Galena	3.7	3.8
Magnetite	2.2	2.2

Table 6. Chargeability of some minerals at 1% concentration in the samples. Injection current = 3s and Integration time =0.02s – 1s (Telford et al., 1990)

Based on the other tables from Telford's paper (1990) there is a general increase for chargeability values with increase in the sulfide content.

3.2.2 Negative IP effects

Negative induced polarization is defined as the vectorial electrical field relationships during the polarizing and depolarizing cycle over a polarizable body (Sumner, 1976). This phenomenon happens when the primary current direction between the potential electrodes M N (measurement of ΔV_{DC}) is not as the same current direction during the off-time (measurement of ΔV_{IP}) (Bertin, 1976). Sumner (1976) explained that during a current injection, a surface charge forming on a polarizable body (known as the charge cycle) then during the discharge cycle, when these charges flow back to return to the electric neutrality, if the potential electrodes detect a reversal in the flow direction this will be reported as the negative IP response.

Negative apparent chargeability can occur as a result of the geometrical distribution of chargeable material, and it is typically seen for longer electrode separations in case of near surface layers with chargeable material. This effect is more usual adjacent to bodies of limited lateral extent, and it can be more significant in the case of outcropping polaraziable body or bodies with a shallow overburden (Bertin, 1976; Sumner, 1976).

In this study the mineralization target is limited in the lateral extent and quite shallow overburden is reported (Mattsson and Thunehed, 2013), thus we are expecting negative IP responses in the measurement over the mineralization zone.

3.3 Electrode arrays

Different types of electrode configurations are designed for measuring differential potential in resistivity and IP surveys. There are at least 102 different surface and down whole array types in which most of them are rarely used. There are three arrays which are commonly used for the electrical surveys:

1. *Wenner* arrays : Standard Wenner , Offset Wenner
2. *Schlumberger* array : Standard Schlumberger (Brant array and *Gradient array*)
3. *Dipole-dipole* arrays*:* Normal (Azimuthal, Radial, Parallel, *Pole-Dipole array*), Equatorial, Square

These different styles of electrode configurations have particular advantage, disadvantages, usages and sensitivities. Depends on the purpose of the survey and space availability, different arrays can be used (Reynolds, 2011). Two arrays which are used in this study are described in more details.

3.3.1 Multiple-Gradient

The multiple gradient array electrode configuration is one of the best electrode arrays regarding the resolution of subsurface structure. When gradient array is combined with multiple current-electrodes then, more than one channel can be measured at the same time and it is so called multiple gradient. This array can be used for the multi-channel data acquisition systems such as ABEM Terameter LS, in which many data points can be recorded simultaneously or sequentially at different locations for each current injection by each two current electrodes. The electrode configuration for multiple gradient array is shown in the Figure 9 (Dahlin and Zhou, 2006).

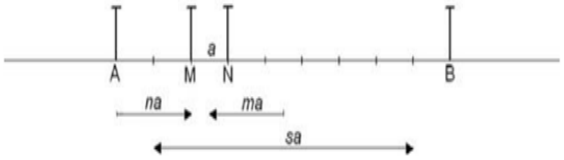

Figure 9. Simple sketch of electrode positions in multiple gradient array. The current electrodes A B with a separation of **(s+2)a** and potential electrodes M N with spacing **a**

(Dahlin and Zhou, 2006).

In Figure 9 *s* is the separation factor and it is defined as the maximum number of potential readings for a current injection and n-factor is defined as the smallest relative spacing between a current electrode and a potential electrode (here A M) and m-factor is the midpoint (midpoint of sensitivity and the plot point in the pseudosection): $m = (X_{MN} - X_{AB}) / a$ Where X_A, X_B, X_M, X_N are the positions of the current and potential electrodes and $X_{MN} = (X_M + X_N) /2$ and $X_{AB} = (X_A + X_B) /2$ (Dahlin and Zhou, 2006).

Apparent resistivity for this array is $\rho_a = K \times (V/I)$ where K (geometric factor) can be calculated for the known 'a', 's' and 'n'. Table7 in the Appendix illustrates the geometry factor and median depth of investigation for different values of a, s and n for multiple gradient array (Dahlin and Zhou, 2006).

3.3.2 Pole-Dipole

This array has a better penetration depth compared to the multiple gradient array. In pole-dipole array one of the current electrodes is placed in "infinity", where infinity is defined as a distance of about 5 to 10 times the length of the array (Dahlin and Zhou, 2006). The electrode configuration for pole-dipole array is shown in Figure 10.

Apparent resistivity for this array is: $\rho_a = K \times (V/I)$ where K is the geometry factor and it can be calculated by $K= 2\pi \times b (b + a) / a$ (Morrison and Gasperikova, 2012).

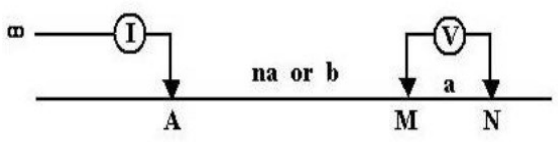

Figure 10. A simple sketch of pole-dipole array. One of the current electrodes(A) with spacing of na from potential electrodes (MN) and the other one (B) is located in infinity (Morrison and Gasperikova, 2012).

3.4 Noise and Coupling effect

Measuring Time domain IP with multi-channel multi electrode systems is a common method in exploration industry. In order to obtain a high level of accuracy in the Spectral IP measurement, noise (including current electrode variations, self-potentials and telluric currents) and electrical distortion (electromagnetic inductive coupling or capacitive coupling) needs to be minimized during the measurement. Furthermore data filtering is generally needed in which apparently distorted data are removed before the inversion and interpretation.

3.4.1 Noises

If the current electrodes vary for every potential reading, changing of the current flow and the frequency can cause distortions within the waveform of the applied current. To compensate for this distortion, multichannel measurement can be applied for measuring the voltage. In this way 6 (or more) pairs of potential electrodes are used simultaneously and each pair's signal waveform phase and their magnitude is directly compared with the injected current, these multichannel systems will also increase the speed of measurement. Furthermore when current flows in the cable, it can induce a current into the ground which can distort the IP responses. Pipelines or railways have also noise effect in the IP survey (Reynolds, 2011).

During the measurement some noise signals can be constrained by filtering within the instrument and also before the inversion with the help of specially designed software such as Aarhus Workbench, which gives the possibility of checking the data quality and deleting noisy IP curves or negative chargeability data.

3.4.2 Coupling effects

Generally there are two main components of electromagnetic coupling; Inductive coupling and capacitive coupling. Inductive coupling occur when energy is coupled from one circuit to another through a magnetic field and it is most likely to happen when the impedance of the source circuit is low (Paul, 2006).

Capacitive coupling is defined as the current leak from a high potential surface / conductor to a low potential surface / conductor. It increases with the increase of frequency and the cable length. High electrode resistance can make it worse, because a larger output voltage will be required to transmit the desired current and at the same time less current can be transmitted due to the high resistivity, which makes the measured signal weaker. It is proposed that the electromagnetic coupling (capacitive coupling) in the multi core electrode cables is the main

reason for creating this problem (Dahlin and Leroux, 2012).

There are three types of common capacitive coupling which may occur during the IP/Resistivity measurement; between transmitter and receiver cables, between soil and cable and between two receiver cables. Shielded cables can help in some extend to reduce this effect but it is proposed by Dahlin and Leroux (2012) that separation of current and potential circuits by using separate multi-conductor cable spreads can significantly reduce the capacitive coupling and improve the data quality. Since the total capacitance is in proportion with the distance between the current and potential circuit, increasing of this distance from couple of millimeter to some decimeter/meter can have a significant influence on the capacitive coupling effects reduction (Dahlin and Leroux, 2012; Reynolds, 2011).

In this study we have tested separation of current and potential cables in our measurements, in order to compare any differences in the results with the single spread.

3.5 Wave forms

The conventional way of measuring time domain IP and direct current resistivity is carried out by using 50 % duty cycle square waveform in the current injection sequence. In this way there are sequences of on-time (when current is transmitted) and off-time (when the current is terminated), a general model for 50 % duty cycle waveform is illustrated in Figure 11.A.

The resistivity is measured during the on-time and the IP is determined based on the potential decay curve during the off-time. It is proposed that there is a possibility to measure the DCIP during the on-time, and reduce the acquisition time to almost half by using 100% duty cycle waveform. In this type of waveform there is no turn-off in the current injection and there is no off-time in the sequences (Figure11.B). More over the signal-to-noise ratio (S/N) of the IP measurement will be theoretically improved by a factor two. However, for the 100% duty cycle waveform measurement, it is important to have a stable and constant current transmission, since unstable current can affect the IP decay curves which are measured during the on-time and we may need to filter many of them before inversion (Olsson et al., 2014).

In this survey both waveforms were used for IP and resistivity measurements on the same field setup, in order to compare the results and to conclude whether we can replace the 50% duty cycle waveform by 100% duty cycle waveform for DCIP measurements or not.

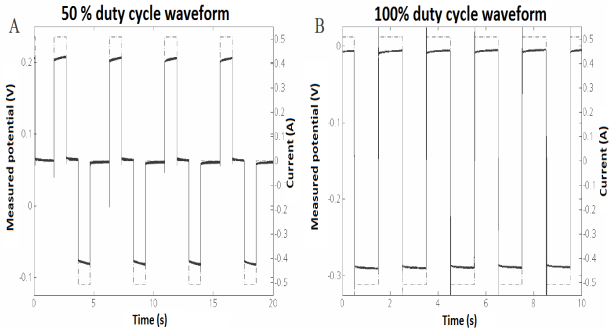

Figure 11. Modeled waveforms for 50 % (A) and 100% (B) duty cycle waveform by P-I. Olsson (2014). Current is illustrated as dashed line and potential as solid line (Olsson et al., 2014).

4. Field work

4.1 Field site

The field work was performed in August 2014 under rainy and cloudy weather conditions. The study area at Liikavaara is a quite flat forested area with small topographical changes and it is mainly following the bedrock surface along the measured profile. The soil cover is relatively thin and covered by thick wet grasses and swamps. There are no bedrock outcrops in the area.

4.2 Equipment / Instrument

The whole survey was carried out with ABEM Terrameter LS and an ES10-64C relay switch unit, during seven days of field work. The Terrameter LS is a state of-the-art data acquisition system, developed by ABEM, for multiple-electrode geoelectrical imaging and it can measure self-potential (SP), resistivity (RES) and time domain induced polarization (IP) (ABEM, 2012).

In this survey we took advantage of resistivity and Spectral-Time domain IP measurements. The Terrameter LS used here has 12 measuring channels (input channels) with measurement range of 2.5 V, 15 V and 1000 V. In this survey 7 channels were used during the multiple gradient array measurement, which means up to 7 sets of current and potential electrodes can be measured simultaneously, whereas the number of measuring channels varied between measurements for the pole-dipole array. Other equipments which were used for the survey:

- Electrode cables

- Stainless steel electrodes

- Cable joints

- Cable jumpers

- Interlink extension cables

- Car battery as the power source

- Johnson revert (starch based polymer intended for stabilizing boreholes during drilling) for improving the electrode contacts

4.3 Navigational data

A Global Navigation Satellite System (GNSS) system was used for navigation and positioning of the electrodes. The electrodes were positioned using a Trimble high-precision Real Time Kinematic (RTK) system, supplied by Boliden Mineral (Trimble R8). Each electrode station was determined with respect to plane coordinates (x,y) in RT90 2.5 gon V and in elevation relative to RH70. Only fixed signal solutions were accepted and were obtained at every station (with two exceptions). Horizontal precision for every pair of coordinates was normally at centimeter scale (0.005-0.020 m) and vertical precision normally at decimeter scale (0.015-0.05 m), depending mainly on wood coverage. These precision intervals applied to fixed signal solutions, floating solutions were slightly worse, yet acceptable, for 1-2 electrode stations.

4.4 Measurement setup

In all the measurements by Terrameter LS the transmitted current was in the range of 10mA as minimum and 500mA as the maximum output current. With this instrument the electrode contacts are estimated before running each measurement, so electrodes with poor ground contact or disconnected electrodes can be identified and they can be improved either by adding another electrode or a contact improvement agent such as e.g. Johnson revert before the measurements start.

The acceptable value for electrode contact resistance can be set by the operator and depends on the geological features of the area; the maximum value that could be accepted for our measurements was 10kΩ.

As is mentioned before, two different current cycles (waveforms) were used, one with 50% duty cycle wave form as IP mode, with +/0/-/0 sequence and the other with 100% duty cycle wave form as RES mode, with +/-/+/- sequence. The chargeability was measured in maximum 12 time windows with different time base 1 s, 2 s and 4 s.

4.5 Electrode arrays

As is mentioned before, the resistivity and IP measurements were carried out with two main electrode configurations. The multiple gradient array measurements with different length of survey lines (405 m, 600 m, 800 m), and different electrode spacing (5 m, 10 m) were performed first. The pole dipole array measurements with 405 m long spread and 5 m electrode spacing were carried out next.

4.6 Electrode cable spread

All the measurements for the selected arrays were performed with both single spread and separate spread in different time base in order to compare any differences in the data quality. The single spread is the conventional way of carrying out resistivity tomography measurement, in which one set of multicore electrode cables can be used for both transmitting current and receiving potential. In the conventional measurement setup generation of undesirable capacitive coupling is expected; whilst separating the current transmission cables and potential receiving cables can decrease this effect (Dahlin and Leroux, 2012).

In this study we tried to apply both types of spread in different measurements, in order to compare the data quality and finding out if there will be any significant improvement in the separate spread measurements. For the separate spread we laid down two sets of parallel cables with 0.5m - 1m distance in between. One set of cable was connected to Terrameter LS and the other cable set was connected to the relay switch ES 10-64C.

4.7 Multiple gradient array

4.7.1 Single spread

The survey started with a 400 m single spread, using a roll along method, with 4 s on-off time in the IP mode (50% duty cycle waveform). Four cables were employed during the full measurement spread with overlapping of the last and first take-outs. All the take-outs in cable number 2 and 3 were used (5 m electrode spacing), but only odd-number take outs in cable 1 and 4 (10 m electrode spacing) (Figure 12). This measurement consists of 3 steps in which in each step we changed the station of the Terrameter. The first station was considered as x= - 20 and cable # 1 was not connected, so we had 3 connected cables and 51 electrodes to be measured (Figure 12- I). In the next step Terrameter was moved 100 m forward and we rolled along cable #1 to the end of cable # 4, the new station was x=0 with 4 connected cables and 61 electrodes to be measured (Figure 12- II). The next station was x=20 and one more time we moved the Terrameter 100 m forward, in this station all the cables were connected with the same arrangement as previous step (Figure 12- III). The measurement continued with one more station change by 100 m which was station x=40 (Figure 12- IV). In total, 600 m was covered in these four steps.

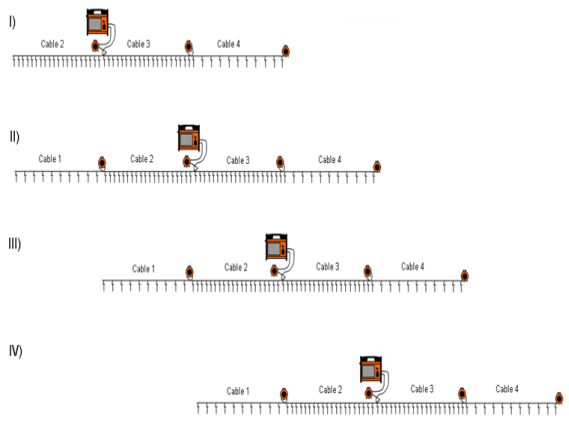

Figure12. Multiple Gradient - 600 m roll along, single cable with 5 m electrode spacing, 50% duty cycle waveform, on/off time 4s.

The final measurement with single spread in multiple gradient array was the extended one with 800 m long layout and 10 m electrode spacing. A total of 8 electrode cables and 81 electrodes were connected. The relay switch ES10-64C was located at the 2nd station and Terrameter LS were located at the 6th station, each had separate power sources and they were connected together with the Interlink extension cables (Figure13).

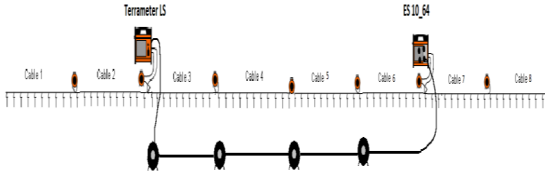

Figure 13. Multiple Gradient array, 800 m XL, 10 m electrode spacing 50 % duty cycle waveform, on/off time 4s. Terrameter LS and ES10-64C are powered separately and they are connected to each other with 4 sets of Interlink extension cables.

4.7.2 Separated spreads

For the 405 m long separate spread, 8 electrode cables and 82 electrodes with 5m electrode spacing were used. The general arrangement was as same as the single spread with 4 connected cables, we just had another set of cables which were laid down parallel to the first cables. One cable set was connected to ES10-64C and the other was connected to the Terrameter LS (Figure 14). Every second take-outs were used in these cables. In order to centralize the target (mineralization zone) in the pseudosection, the starting point was selected 200 m ahead of the previous measurement's start point and the cables extended till 605 m. In this separated spreads arrangement three different time bases 1s, 2s and 4s were applied and for all these different time bases, the measurement carried out with both 50% and 100% duty cycle waveforms.

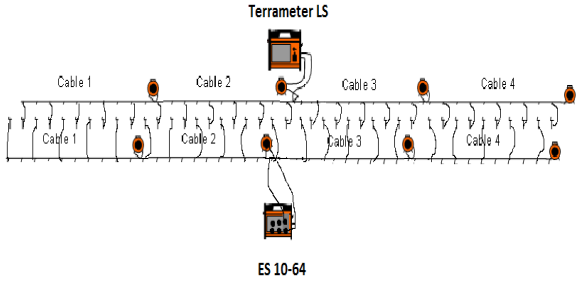

Figure 14. Separated spreads – 405 m long, 5m electrode spacing. 4 sets of cables are connected to ES10-64C and transmitting current the other cable line is connected to Terrameter LS and measuring potential. Both 50% and 100% duty cycle waveforms were tested in this arrangement for different on/off time.

4.8 Pole-dipole array

4.8.1 Single spread

In this array 4 cables and 81 electrodes, with 5 m electrode spacing were arranged and the whole length of the measuring line was 400 m. As it mentioned before, for this array one of the current electrodes is placed at "infinity" which can be defined as the distance of about 5 to 10 times the length of the array and for this survey line it would be between 2000 to 4000 m. We placed the remote current source 2.5 km far away from the Terrameter LS, which can be considered as the 'effective infinity' distance (Figure 15). The single remote electrode was connected to the Terrameter by a 3km long cable through input C_2. 2s on/off time and 50% duty cycle waveform (IP mode) were applied for this measurement.

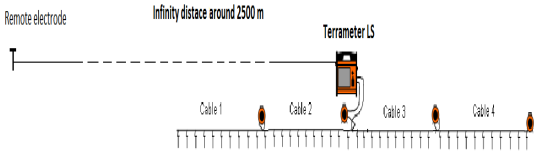

Figure 15. Pole-Dipole array, single spread, 400 m long, 5 m electrode spacing, 2s on/off time, 50% duty cycle waveform. The remote electrode is placed in an effective infinity which is around 2.5km and connected by a long cable to Terrameter LS.

4.8.2 Separated spreads

The general arrangement was same as the single spread in pole-dipole array, we only added four sets of cables parallel to the existing one and connected them to the relay switch ES10-65C in order to separate the current and the potential circuits. The length of the survey line was 405 m with 82 electrodes and 5 m electrode spacing. Measurements were made with 2s on-off time, in both the 50% duty cycle waveform (IP mode) and the 100% duty cycle waveform (RES mode). The same remote electrode was used as the infinity distance for this array (Figure 16).

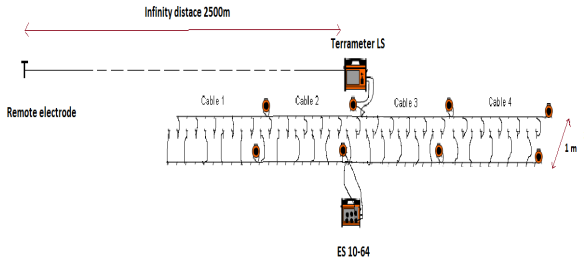

Figure 16. Pole-dipole array, separate spread, 405 m long, 5 m electrode spacing, 2 s on / off time, with both 50 % and 100 % duty cycle waveforms. The remote electrode is placed in an effective infinity (around 2.5 km) and connected by a 3 km long cable to Terrameter LS.

5. Results and interpretation

5.1 Data processing

As is mentioned different measurements with different arrangements and settings were tried out on the survey line, all of them are summarized in the following table (Table8).

We collected data from east towards the west of the area, whereas the previous survey on this line has been measured from west to the east. In order to be able to compare the results conveniently, we reversed all the data sets and coordinates, and then processed the data.

The inversion process was done via two different geophysical software; Res2Dinv and Aarhus-Workbench. Res2dinv creates model sections of resistivity and chargeability (m_0), whereas Aarhus-Workbench models also include the spectral IP parameters C and Tau.

As the first step, for evaluating the data quality of the measured data, we plotted them as peseudosections of apparent resistivity and apparent chargeability in Erigraph.

This software uses linear interpolation which reveals the outliners clearly, therefore it can give a general overview of the measured data.

Exporting the measured data from the Terrameter LS to PC via Terrameter LS Toolbox (companion software for the instrument from ABEM) was the next step. All data were exported to DAT. file format with two different types, one with summarized IP windows which used for Res2Dinv and the other with exporting all IP windows for AarhusInv/ Workbench.

The latest version of Res2Dinv (Res2dinv x 64 version.4.03.32.) was applied for this inversion. Robust inversion (L1 – norm type) was selected for all the cases, this norm type is used when there are strong resistivity contrast in the data (Dahlin and Leroux, 2012). The inverted models for IP and resistivity are illustrated in the 'Appendix' section.

For the quality checking of the IP decay curves, we plotted them in Workbench. Curves which show negative chargeability were deleted for 50% duty cycle waveforms, but we tried to keep the negative chargeability data in the 100% duty cycle waveforms. Noisy curves were also deleted manually. In some cases Auto filtering were applied as well, in which curves with a specified maximum slope change can be deleted. However, in the shorter time base (specialy1s) we may lose some part of the curves since the IP windows are more restricted to the shorter time and the slope is much sharper. After filtering the decay curves in Workbench, we ran the inversion in smooth mode (L_2 - norm type). This software creates model sections for resistivity, chargeability, tau (τ) and C parameters. Moreover the measured data with 100% duty cycle waveform can be inverted in this software whilst it is not possible in Res2Dinv.

Sections illustrating the 2D inversion models in AarhusInv are included in Appendix of this report.

Profile name	Array type	spreads	Waveform	Time base	Length	Measuring time (h)
A (roll along)	Multiple gradient	single	50 %	4 s	600 m	6 + 3:30
B	Multiple gradient	single	50 %	4 s	800 m	3:58
C	Multiple gradient	Separated	50 %	4 s	405 m	2:33
D	Multiple gradient	Separated	100%	4 s	405 m	1:50
E	Multiple gradient	Separated	50 %	2 s	405 m	1:24
I	Multiple gradient	Separated	100%	2 s	405 m	1:00
F	Multiple gradient	Separated	50%	1 s	405 m	00:50
J	Multiple gradient	Separated	100%	1 s	405 m	00:34
PD 1	Pole-dipole	single	50%	2 s	400 m	3:35
PD 2	Pole-dipole	Separated	50%	2 s	405 m	4:21
PD 3	Pole-dipole	Separated	100%	2 s	405 m	2:33

Table 8. Table of measurement for different profiles

5.2 Raw data presentation

5.2.1 Pseudosections

Pseudosections of apparent resistivity/chargeability displayed in Erigraph software for profile C.

These pseudosections give a general impression of data quality in the measured data and hint us to what we may expect in the inverted models, also suggested pseudo depth show the approximate penetration depth for each measurement.

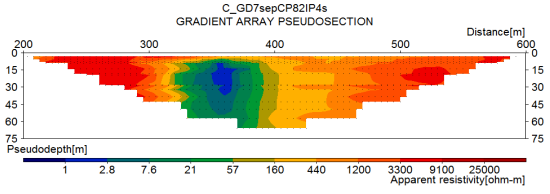

Figure 17. Pseudosection of apparent resistivity for profile C. The high conductive zone between 300 and 400 m suggests the approximate interval of the mineralization zone.

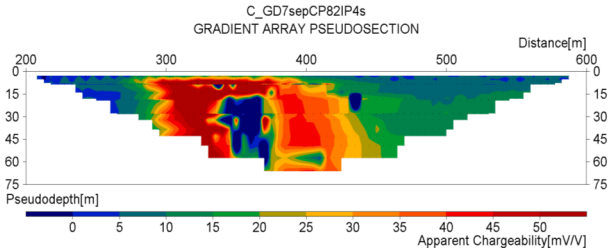

Figure 18. Pseudosection of apparent chargeability for the same profile (C). The high chargeable area around the high conductive zone is noticeable in the pseudosection.

Almost a same pattern can be seen in the inverted models from the other measurements (see Appendix).

5.2.2 Full waveform data

Terrameter LS Toolbox (ABEM) provides the possibility of plotting the full waveforms in different measurements. Profile C and profile E are illustrated in Figure 19. On the right side of each figure the number of used channels is shown and in this specific measurement seven channels were applied simultaneously for measuring potential

Black lines show the transmitted current (TX current) and the colored lines are the measured potentials from different channels.

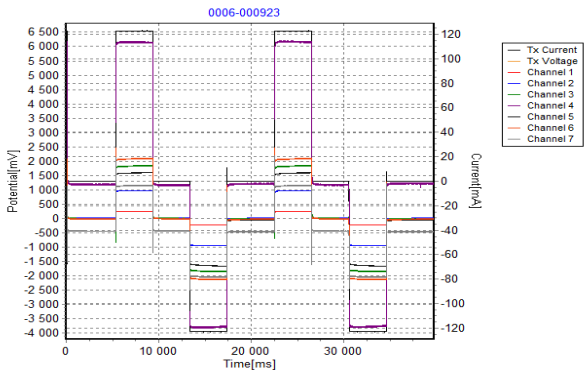

Figure 19. Full waveform during a single measurement in 50% duty cycle waveform (profile C; 4 s on-off time).

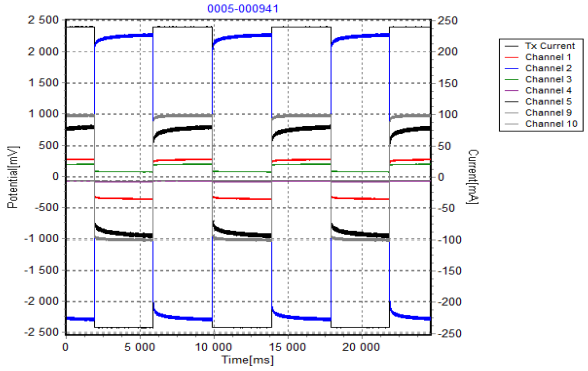

Figure 20. Full waveform during a single measurement in 100% duty cycle waveform (profile D; 4s on-time).

5.2.3 IP curve Presentation in Workbench

The IP curves over the mineralization zone and the host rock are shown in the following Figures.

Negative apparent chargeability and noisy curves are seen mostly over the mineralization zone which can be due to the high conductivity of the ore minerals. When a highly conductive polarizable body is present in the subsurface (specifically when it is close to the surface) the depolarizing current will be internally short out through the conductive body (Sumner, 1976) and as the result the potential difference readings (ΔV_{IP}) between every two potential electrodes will be very small values. This can lead to disturbed IP curves as it is seen in Figure 22, 23 and 25. Another reason can be the effect of electromagnetic coupling (inductive coupling and capacitive coupling) which can be more significant over the high conductive zones.

As is mentioned before, the capacitive coupling may happen in three different ways and the separation of the current transmission and potential receiving cables can only help to reduction of one type of these coupling effects (between transmitter and receiver cables). Thus we may still see disturbed curves even in the separated spreads.

Decay curves over the mineralization zone are disturbed almost in all the measurements. However, in the single spread data set the disturbance of curves happen in a wider range than the separated spreads data and it is more likely that the coupling effects happened between transmitter and receiver wires as well as the ground and the cables in these single profiles (see Figure 22, 23-right).

Decay curves over the host rock (high resistive area) show a high quality of IP data almost in all the measurements. In the single spread we can still see some signs of disturbance specifically in the first time windows in profile A, B and PD-single. Disturbed or deleted curves with poor quality are marked with red circles in the single spreads and compared with the same depth interval in the separated one over the host rock in Figures 21 and 23-left. In profile B- 800 m, we can see even worse data quality compared with the profile A- 600 m, and this is because of the long cable length applied for this measurement which makes the capacitive coupling stronger.

Generally the pole-dipole measurements have a smaller level of signal to noise ratio and the result curves are much noisier in comparison with the multiple gradient array (Figure 23). However, applying 100% duty cycle waveform for this array improved the quality of the IP curves and decreased a noticeable number of noisy curves, specifically IP curves measured over the host rock (see Figure 24 and 25).This noticeable reduction in the number of noisy curves can be seen in all the measurements with 100% duty cycle waveform. This can be due to a higher signal to noise ratio which was expected from this type of waveform (Olsson et al., 2014)

In the 1s on-time measurement the end of the decay curves reached negative values. This can be due to the very short injection time (1s) in which the current will reverse the polarity, before the signal decay is completed.Another reason can be the variation of background potential level (telluric current or polarized potential from the previous measurements). This can be compensated in the instrument software or during the signal processing (for 100% duty cycle). Some noisy curves and curves with negative chargeability are filtered through Workbench, these curves are colored in grey. In the plots (in Figure 25) however, we tried to keep the negative IP data in the 100% duty cycle waveform measurements, since we got a better residual in the inverted model.

Decay curves of 50% duty cycle waveforms:

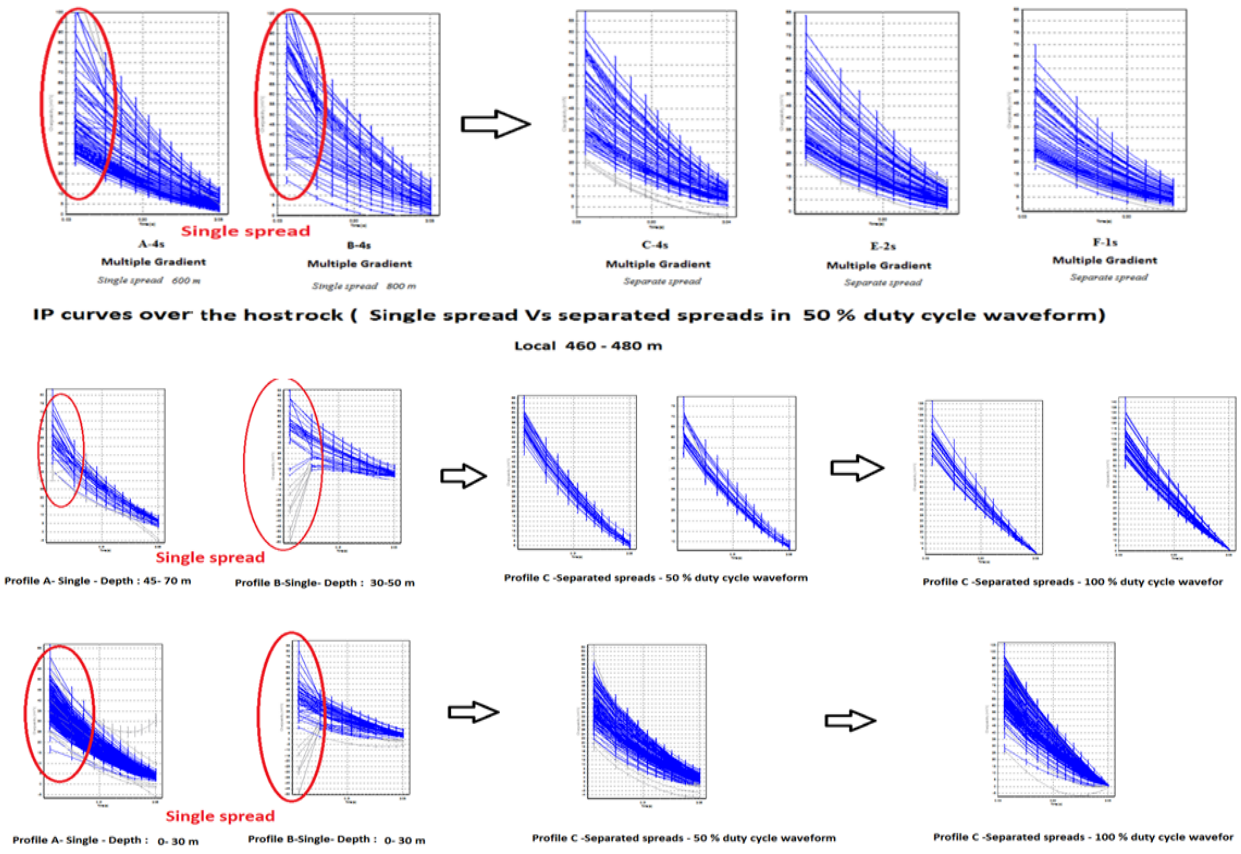

Figure 21. Multiple-gradient array, IP curves over the host rock (local 460-480 m and 500-600 m) for different time bases, waveforms and different spreads.

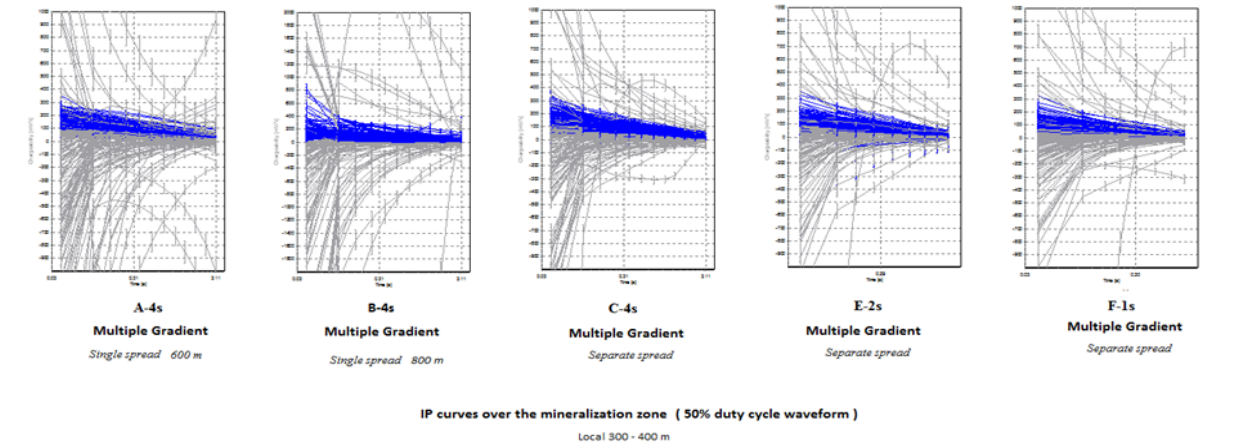

Figure 22. Multiple-gradient array (50%), IP curves over the mineralization zone (local 300-400 m) for different time bases and different spreads.

5.3 Interpretation of inverted data

Generally resistivity data are considered to be more related to the geology and the subsurface structures, whereas the IP data are more suitable for representing of distribution of metallic ores. Thus they should be interpreted separately and from different points of view. For example thickness of overburden or depth of oxidation can be seen is the resistivity data whilst IP data provides information about the mineralization areas (Sumner, 1976).

5.3.1 The general overview of the site:

Profile **A**: Single spread, 4s, 50% duty cycle waveform, Profile length: 600m

Profile **B**: Single spread, 800m XL, IP 4s, 50% duty cycle waveform, Profile length: 800m

A general overview of the site is shown in these two sections. There is a huge resistivity difference between the mineralization zone (highly conductive zone), around 1 Ω m, and the bed rock that exceeds 20,000 Ω m. In Figure 26 and 27 the extent of the mineralization zone is seen in green and blue, which can be a sign of massive sulphide (local between 305 to 450 m, UTMX between 1727635.95 to 1727771.843) and widens down to 130 m depth and then gradually changes to orange/red, which can refer to a gradual decrease in the sulphur content in depth and towards the surrounding host rock. The inverted models from both softwares are presenting almost a similar interval for the mineralization zone and border of the host rock.

In the AarhuInv models there are gradual changes of the very high conductive area in the core of the mineralization zone outwards to the host rock, this delicacy cannot be seen in the Res2Dinv models, which is due to different norms that were applied for inversion in these two softwares. Norm-L_2 which applied in AarhusInv, makes the models smother and any changes in the resistivity or chargeability can be seen in a gradual form, whereas sharp changes is one of the features which can be seen in norm- L_1. These different norms also cause some differences in the model scales, colours and corresponding values for resistivity or chargeability in these two softwares.

5.3.1.1 DC models

I- AarhusInv:

Figure 26 -A

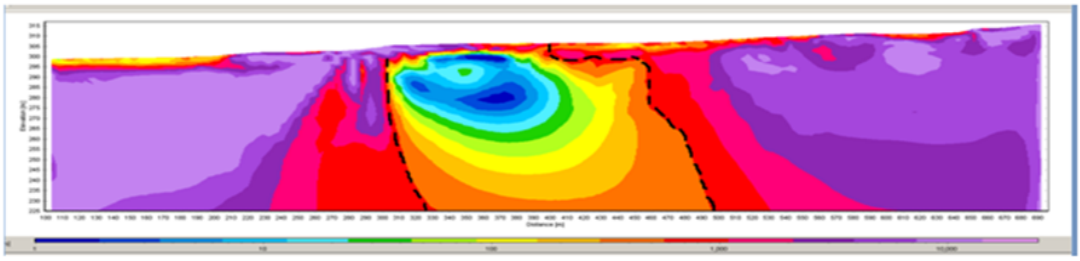

Figure 26 -B

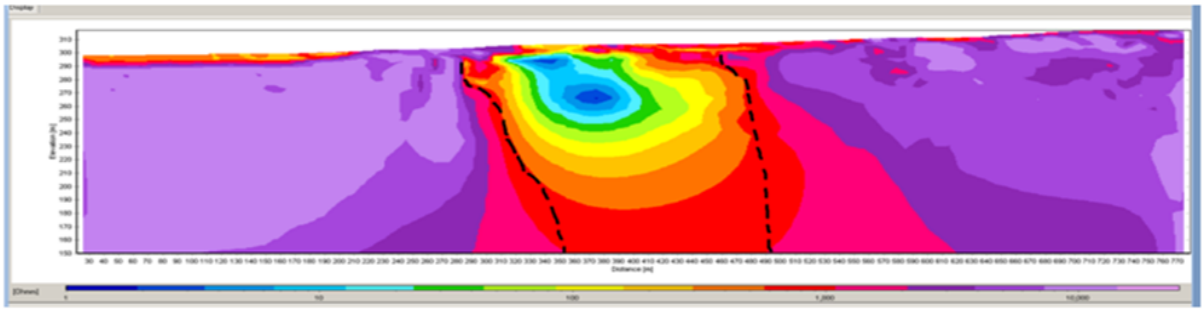

Figure26. AarhusInv resistivity model for profile A and B. Mineralization zone is marked by dashed line. Approximate penetration depth model: 85 m for the 600 m (A) and 160 m for the 800 m (B).

II- Res2Dinv:

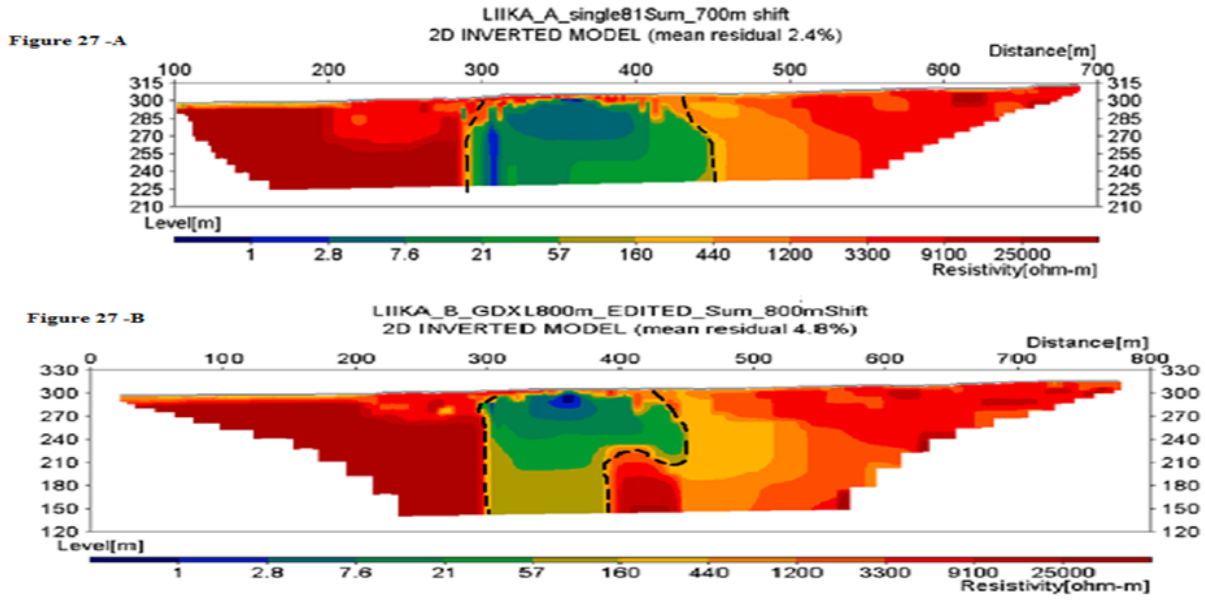

Figure27. Res2Dinv resistivity model for profile A and B. Mineralization zone is marked by dashed line. The approximate penetration depth: 85 m for the 600 m (A) and 160 m for the 800 m (B).

5.3.1.2 IP models

In the IP models inverted in AarhusInv the mineralization zone (local 305 - 450 m) with relatively high sulphur contents produces moderate IP response, compared with the surrounding areas, and the reason can be that; this highly conductive polarisable body can internally short out the depolarizing current and as the result we will have a considerably diminished observable IP response (Sumner, 1976). Whilst in the area with disseminated sulfides with lower sulfur content (low- moderate conductivity) the IP response will be recorded without any short circuits problem.

As it is seen in all the IP models, the mineralization zone does not show a very high IP response while we can see high chargeable features in the surrounding areas (local 240 to 305 m; XUTM 1727575.036 to 1727635.95 and local 410 to 620 m; XUTM 1727735.006 to 1727931.436) deep down to 70 m depth, as well as in the shallow parts, above the mineralization zone. These high chargeable features, which are not showing high conductivity, can be the result of disseminated ores (sulphides) which are dispersed around the concentrated ore zone.

In other words, this can be a halo of fragmented conductive materials which are dispersed in a high resistive host rock as its back ground. Since they are disseminated ores and not connected to each other like the solid ore zone, conductivity is not continuous in these parts, so there is less possibility of internally shorting out the depolarization currents and as the result higher IP response can be observed. The dashed lines on the IP models are the areas that we suppose are representing the disseminated sulphides. There are some differences in the chargeability scale values between Res2Dinv and AarhusInv models, which can partly be explained by different norms which were applied for the inversions in these two softwares (norm- L_1 applied in Res2Dinv and norm- L_2 in AarhusInv).

These chargeable features are more prominent in the AarhusInv models, and most of the models from different measurements confirm these anomalies. Whilst in the inverted models by Res2Dinv for the 800 m long profile, it is quite difficult to identify the chargeable zone, see Figure 29.

I- AarhusInv:

Figure 28 -A

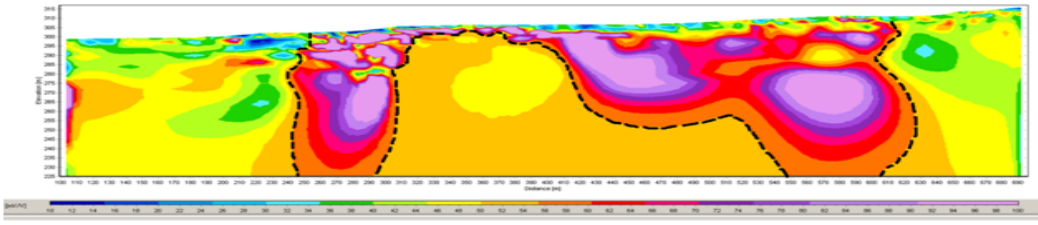

Figurw 28 -B

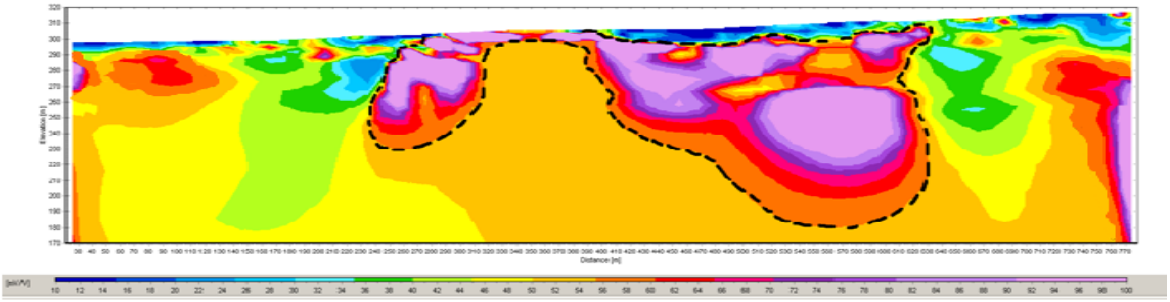

Figure 28 . AarhusInv IP model for profile A and B. High chargeable zones are marked by dashed lines which are supposed to be the disseminated sulphides. Approximate penetration depth model: 85 m for the 600 m (A) and 160 m for the 800 m (B).

II- Res2Dinv

Figure 29 -A

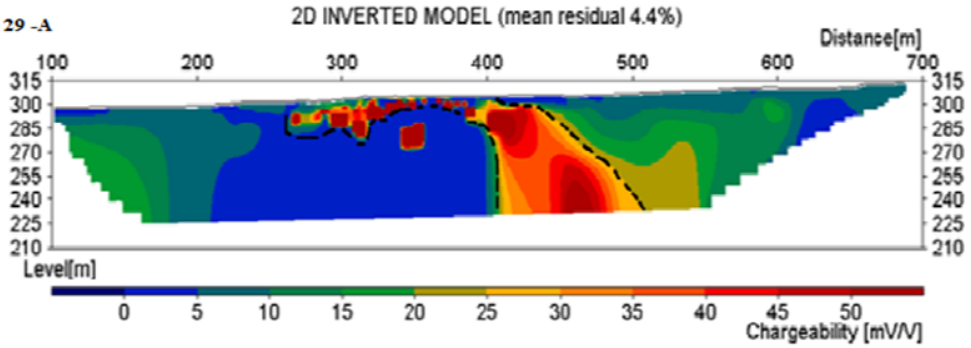

Figure 29 -B

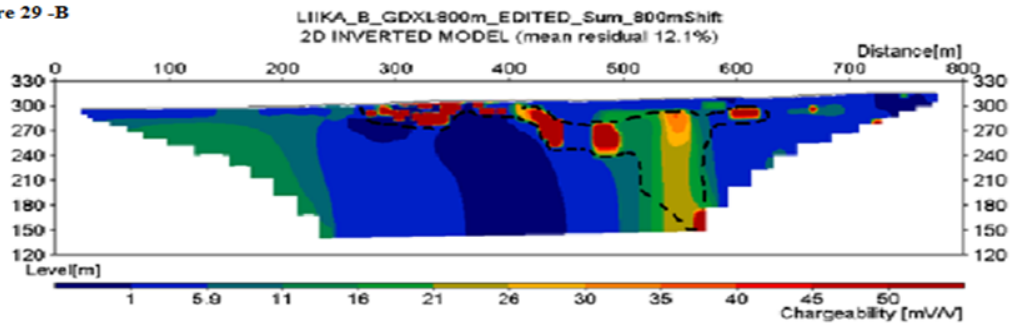

Figure 29. Res2Dinv IP model for profile A and B. High chargeable zones are marked by dashed line. Approximate penetration depth model: 85 m for the 600 m (A) and 160 m for the 800 m (B).

5.3.2 Correlation of mineralogy / sulphur content with the models:

In the following Figures sulphur content for borehole number 365, which is close to the survey line and partly covers the mineralization zone, is compared with borehole 364 which mostly covers the host rock (footwall). The slope of the drillings varied between 34 – 52 degrees for borehole 365 and between 44- 56 degrees for borehole 364. Thus we consider the mean value for the slope of drillings in the sketches (Figure 30, 31and 32).

The high sulphur contents in depth interval of 8.6 -13 m, 13-18, 48-53 and 88-92 matches well with the very high conductive zones. However in the depth of 180-181 m the corresponding depth shows relatively low conductivity and probably lower sulphur content, but the chemical analysis indicates 1.96% of sulphide which a is quite high percentage (Figure30 and 31). Based on the logging of borehole 365 this depth is corresponding to a dyke intrusion and this relatively high sulphur content is restricted to the presence of this dyke and it is not seen in the other parts of host rock. This can be also due to the distance of the borehole from the survey line which is approximately 20 m, and since the distribution of sulphide is not necessarily homogenous in the mineralization zone we may not expect an exact match of these statistics with the models. Low resolution of the models can be another reason. Nevertheless, a first-order interpretation is; the lower resistivity values, the higher sulphur contents are expected at the corresponding depth.

In profile I (Figure 32), which is more focused on the mineralization zone, the very high sulphur contents (2.6% and 3.7%) are indicating medium anomalies, coloured mostly in yellow, which can be seen in different depths whilst the very low resistive zone, coloured in blue, is corresponding to relatively low sulphur content (below 1.5 %). This can be due to the variety of different sulphide types which makes some parts more conductive. For example pyrrhotite (iron sulphide) is much more conductive comparing with pyrite (FeS_2) or chalcophyrite ($CuFeS_2$) (see Figure 6). Thus the high conductive area (coloured in blue) which does not show very high sulphur content can be due to the different component of sulphides. For instance it can be a combination of higher proportion of pyrrhotite and lower pyrite or chalcopyrite, which in total does not show high sulphur content in the chemical analysis, but the resistivity models represent it as a very high conductive area (based on Table 1 in Appendix).

Moreover the proportion of copper to iron (Cu/Fe) is electrically important, the copper rich samples are more resistive and iron rich samples show more conductivity (Pridmore and Shuey, 1976). Thus, we can assume that the high conductive zone in the central part of the mineralization segment contains more iron rich minerals (sulphides) and by getting further from the core of the zone, copper / iron ratio is increasing (lower iron and probably higher copper or it can just be the result of lower iron) until the edge of the host rock wall. Presence of higher Fe_2O_3, MgO, CaO in the mineralization part and lower percentage in the host rock are approved in the geochemical analysis of the selected core from borehole 370 (245 m far away from our survey line) (Estholm, 2014), however copper content is not documented in the geochemical analysis of this report.

Profile B-AarhusInv; single spread, 4s, 50% duty cycle waveform, 800 m:

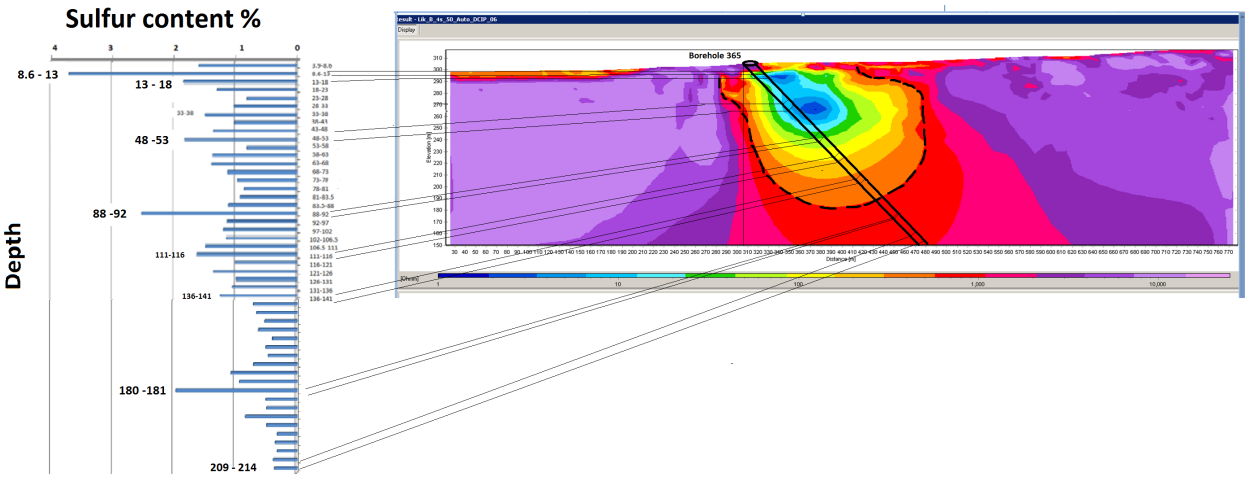

Figure 30 . Comparison of the sulfide content from borehole 365 (located in 20 m northern part of our survey line) with the inverted model from profile B in AarhusInv. The mean slope of the drilling is drawn in this sketch.

Profile B- Res2Dinv:

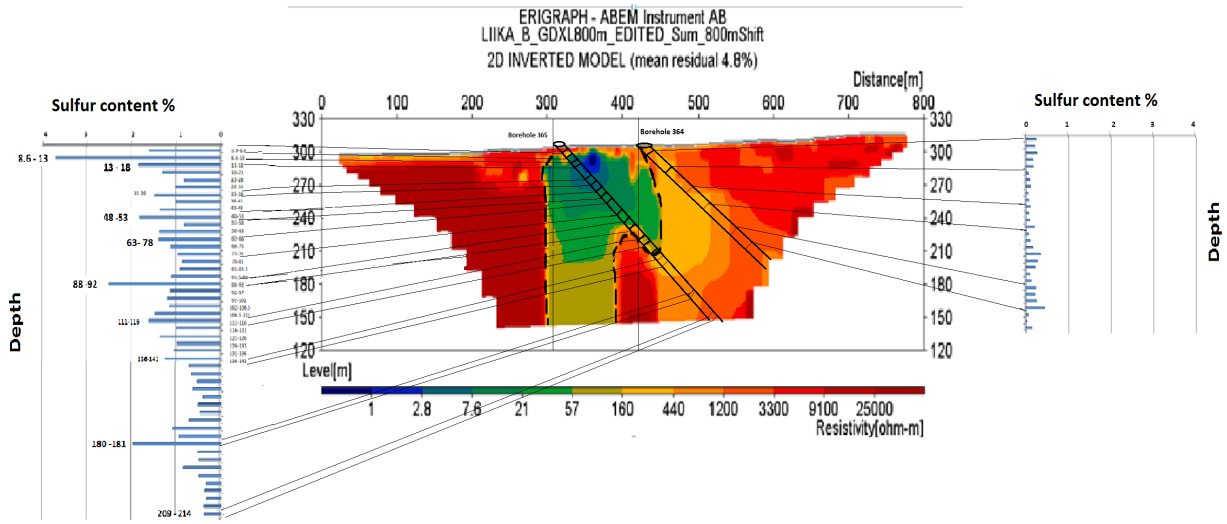

Figure 31 . Comparison of the sulfide content from borehole 365and 364 (located in 20 m and 30 m northern part of our survey line) with the inverted model from profile B in Res2dinv. The mean slope of these drillings are drawn in the sketch

Profile I: Separate spread, 2s, 100% duty cycle waveform, 405m :

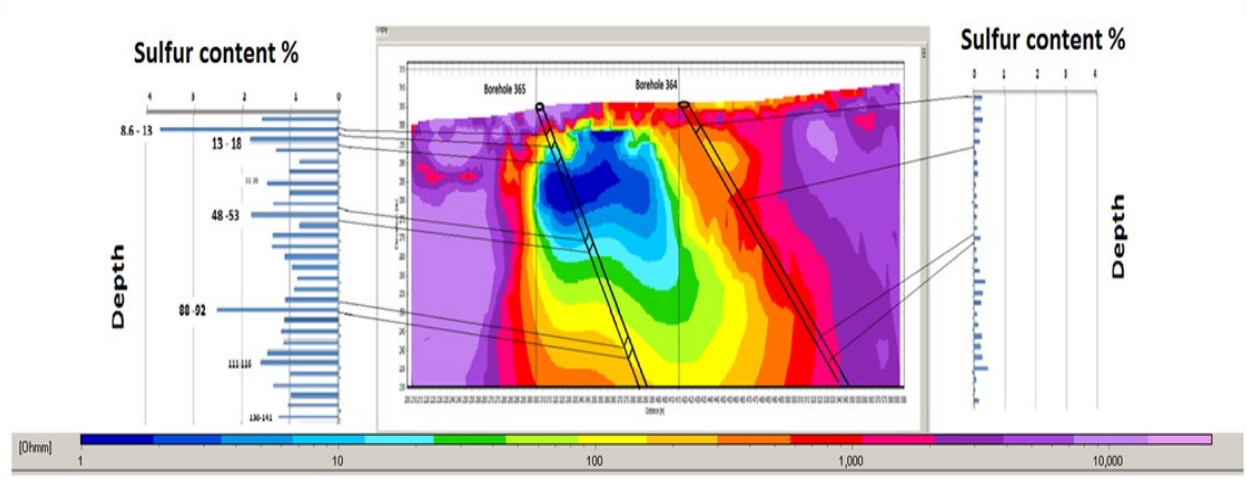

Figure 32 . Comparison of the sulfide content from borehole 365and 364 (located in 20 m and 30 m northern part of our survey line) with the inverted model from profile I in AarhusInv. The mean slope of these drillings are drawn in the sketch.

5.3.3 Comparison of residual / data quality

The same default settings were used for all the inversions in Res2Dinv, so it is possible to compare the residual differences of different data sets inverted in this software.

Whilst, in AarhusInv, different settings and filtering methods were applied for each single inversion. These differences in the inversion settings can affect the calculated residual, specifically when some curves with very high resistivity/chargeability values are kept in the data set. This can make a noticeable change in the standard deviation and also misfit between the measured data and the modelled section. Thus, comparing only residuals cannot be the most reliable way to find out which profile has a higher data quality, especially in AarhusInv.

5.3.3 .1 Multiple gradient array

AarhusInv:

- **Single spread: Profile A and B**

Since the roll along method was used for profile A, a larger number of data were measured for this profile which also gave a better data coverage over the mineralization zone. Although the residuals for both profiles are quite similar, there was less need of filtering in the raw data for profile A.

In the profile B (800 m long) we expected more coupling effect due to the long cable length and also weaker signal to noise ratio because of the larger electrode spacing which were used for this measurement.

As it expected, noticeable number of data needed to be deleted, which could be the result of these effects.

- **Separated spreads: Profile C, E, F**

In the 4s measurement we got an acceptable residual from the very first inversion. Whilst in 2s and 1s measurements more than four inversions were run with different settings and filtering methods and in the end the one with the lowest residual was selected for presenting in the appendix. The 100 % duty cycle waveform in all three time bases required less filtering in the raw data, regardless of keeping or deleting the negative IP curves. Moreover the measuring time in 100 % duty cycle waveforms were almost half of the same measurement in 50 % duty cycle waveform.

Single-50%	Residual (DC./IP)	Negative IP curves	No of data	No of filtered data	Measuring time (h)
A- 4s	DC: 11.02 % IP:2.37 %	Deleted	2383	227 (9%)	6 + 3:30
B- 4s	DC: 11.83 % IP:2.21 %	Deleted	1299	(20%)	3:58

Table 9 . Comparison of data quality in profile A and B (single spreads– 50% duty cycle waveform) with different profile length, AarhusInv.

1s	Residual (DC./IP)	Negative IP curves	No of data	No of filtered data	Measuring time (h)
50% duty cycle	*DC: 3.4 IP:3.49	Deleted	1138	*153 / 95 (13%)	00:50
100% duty cycle	*DC:2 IP:4.19	Kept	1138	*111/ 82 (9.7%)	00:34

2s	Residual (DC./IP)	Negative IP curves	No of data	No of filtered data	Measuring time (h)
50% duty cycle	*DC: 4.2 IP:2.76	Deleted	1138	*158/ 72 (13%)	1:24
100% duty cycle	DC: 7.6 IP:2.95	Kept	1138	114 (10%)	1:00

4s	Residual (Res./IP)	Negative IP curves	No of data	No of filtered data	Measuring time (h)
50% duty cycle	DC: 5.7 IP:3.11	Deleted	1138	112 (9.8%)	2:33
100% duty cycle	DC:6.25 IP:2.29	Kept	1138	112 (9.8%)	1:50

Table 10. Comparison of data quality in profile C, E and F (separated spreads) with different time bases and waveforms- AarhusInv. Note: The DC values which are marked with * are collected from another inversion results that we got a better residual with more filtering, in these cases both models are illustrated in the Appendix.

- **Single spread : Profile A and B**

In the inverted model by Res2Dinv the 800m long profile shows a higher residual and capacitive coupling can be the main reason for this problem, as is mentioned before coupling effect increases with the increase of the cable length, specifically when the current and potential wires are not separated, and as the single spread were applied for this measurement, high residual and noisy IP curves were expected.

Moreover, larger electrode spacing leads to smaller signal (smaller signal to noise ratio) and a higher geometric factor, which means lower potential differences will be measured between each two electrodes. Thus, 10 m electrode spacing in profile B compared with 5 m electrode spacing in profile A, will include larger geometric factor, smaller S/N ratio and consequently smaller potential readings, which can be another reason for explaining these residual differences.

Single spread-50% duty cycle	Residual (DC./IP)	
4s (600 m)	DC: 2.4 %	IP:4.4 %
4s (800 m)	DC: 4.8 %	IP:12.1 %

Table 11. Comparison of data quality in profile A and B (single spreads) with different profile length-Res2Dinv.

- **Separate spread :Profile C, E, F (405 m)**

Comparing three measurements in different time base; the residual differences are not significant and the inverted models are quite similar. Even though the measurement in 4s shows the best residual in both IP and DC, it should be considered that it was the most time consuming measurement in the field.

Separated spreads-50% duty cycle	Residual (DC./IP)	
4s	DC: 3 %	IP:4.4 %
2s	DC: 3.1 %	IP:4.7 %
1s	DC: 3.4 %	IP:6.3 %

Table 12. Comparison of data quality in profile C, E and F (separated spreads) with different time bases-Res2Dinv.

5.3.3.2 Pole dipole array

- **AarhusInv**:

Generally, due to the higher sensitivity of this array to noise, these data sets required more filtering in the raw data than the multiple-gradient array.

Since different protocols were applied for different spreads the numbers of data sets are not equal. Thus the ratio of the filtered data can be compared instead.

There was another problem with the separated spread-50% data; that we got a huge number of negative resistivity. Since the measuring was performed in a different day with single-50% and separed-100% there is a possibility of wrong connections in some cables in that measuring date. However, all the negative data were deleted before the inversion ran.

The 100% duty cycle waveform measurement data were inverted twice, once with and once without negative IP curves, and better residual was reached for the inversion with deleted negative data.

In the 100% duty cycle waveform lower number of data was filtered in comparison with the other measurements in 50% duty cycle waveform

- **Res2Dinv:**

The IP residual is quite high in both spreads, especially for the IP in the single spread with 26 % which means the inverted model is not well matched with the measured data and the possibility of getting artifacts is much higher, thus the model from separated spreads measurement is more reliable. However, even though the single spread still shows a better DC residual, the models and anomaly intervals are quite similar.

PD-2s	Residual (Res./IP)	Negative IP curves	No of data	No of filtered data	Measuring time (h)
Separated spreads 50% duty cycle	DC: 4.88 IP:2.6	Deleted	1717	396 (23%)	4:21
Separated spreads 100% duty cycle	DC: 8.28 IP:2.76	Deleted	2684	529 (19 %)	2:33
Separates spreads 100% duty cycle	DC: 12.45 IP:3.47	Kept	2684	430 (16 %)	2:33
Single spread 50% duty cycle	DC:7.75 IP:2.34	Deleted	1332	(22%)	3:35

Table 13. Comparison of data quality in pole-dipole array with different spreads and waveforms-AarhusInv.

Pole dipole-50% duty cycle	Residual (DC./IP)
2s -Single	DC: 6.7 % IP:26 %
2s -Separated	DC: 11.8 % IP:11 %

Table 14. Comparison of data quality in pole-dipole array with different spreads and waveforms-Res2Dinv.

5.4 Tau and C Parameters

The time constant Tau and frequency exponent C are measurable physical properties which describe the shape of the decay curve. The behaviour of these two parameters is mainly controlled by the mineralization texture (grain size and grain size distribution) regardless of the type of metallic mineral which are present in the ore body. As it is seen in Figure 34 and also the other models from different measurements (see Appendix) C and Tau models presenting almost a similar pattern, thus we can expect a quite homogenous texture in all the areas without anomaly which are illustrated in a plain colour in both models (light blue in Tau and yellow in C).

Reynolds (2011) suggested a distinctive chargeability-relaxation time behaviour for massive sulphide bodies, but due to the same reason of not reaching significant chargeability response over the mineralization zone, the relaxation time and C are not presenting high values over the ore zone and in the surrounding areas instead there is a halo of anomaly around the ore zone, which are marked with dashed line in Figure 33. In these areas different textures and likely disseminated ore can be expected. Also higher values in the relaxation time (Tau), which is approximately 45 m below the surface, can refer to the presence of more coarse-grained disseminated ore compared to the lower values of Tau (Reynolds, 2011).

This can be partly confirmed by the graphic logging of core 367 (local 460 m) which shows coarser grain size in the depth interval of 15 m to 41 m (Estholm, 2014).

However, we selected the model which shows quite huge anomaly in Tau and probably more reliable one (C-4s-separated spread), otherwise the graphic logging may not be matched well with the models from the measurements in shorter time.

Reynold (2011) also suggests that any changes in the texture in the pyrite zones can indicate the presence of gold, copper or zinc. Thus we may expect these minerals mostly in the halo of presented anomaly in C and Tau.

We also tried to find a correlation between these anomalies and any structural changes based on the logging data from borehole 365, 364 and 363 and as the result ‘Fracture’ is the most common structure found in the depth intervals which are corresponding to the high anomalies for C and Tau in all these three boreholes, whilst it is quite rare or weak in the areas which are presenting plain colour (no anomaly) in both parameters. It is likely that these fractures are filled with sulphides and caused theses anomalies as a halo of disseminated sulphides around the ore zone.

The data qualities for these parameters are compared for different measurements in Figure 34 and 35. Parameter C presents almost a similar pattern as chargeability models (see appendix). The anomalies for parameter C differ a bit for different time bases. This can be seen in the following Figures; all the measurements in 4s on-off time, regardless of single or separated spreads, represent almost a same depth for the anomalies, whilst measurements with shorter time bases (2s and 1s) present the anomalies in shallower depth (5 to 10 m shallower). This is more prominent in the relaxation time (tau) models, where anomalies are restricted to shallower areas by decreasing the time base (Figure 34).

Since most of the data sets in 4 second confirm the depth of anomalies ca 30-45 m for Tau and ca 65 m for C, we can assume that shorter on-off/on time can decrease the data quality in Tau and partly in C due to two main factors: 1) decreasing signal level (lower S/N) with shorter acquisition time, and the tau/C differences may be covered by ambient noise and 2) with shorter acquisition time ranges, the resolution on the spectral parameters decreases, without changes in the relative noise content.

Single or separated spreads and different types of waveforms do not have a significant effect on these two parameters. However, Tau still shows some sensitivity for different waveforms. In the pole-dipole the 50 % duty cycle shows an artificial tail for C this tail can be seen in chargeability model as well (see Figure 37).

Although different injection times appear to influence on the models of Tau and C, it does not show any remarkable effect on the final models in resistivity and IP (see Figure 38).

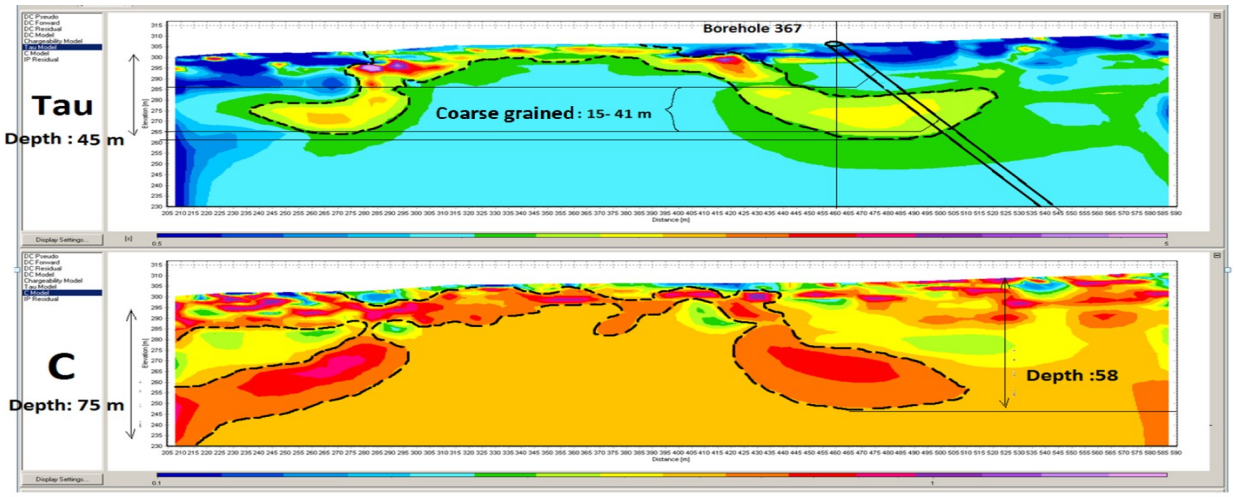

Figure 33. Tau and C models from Profile C-4s-50%duty cycle wave form.

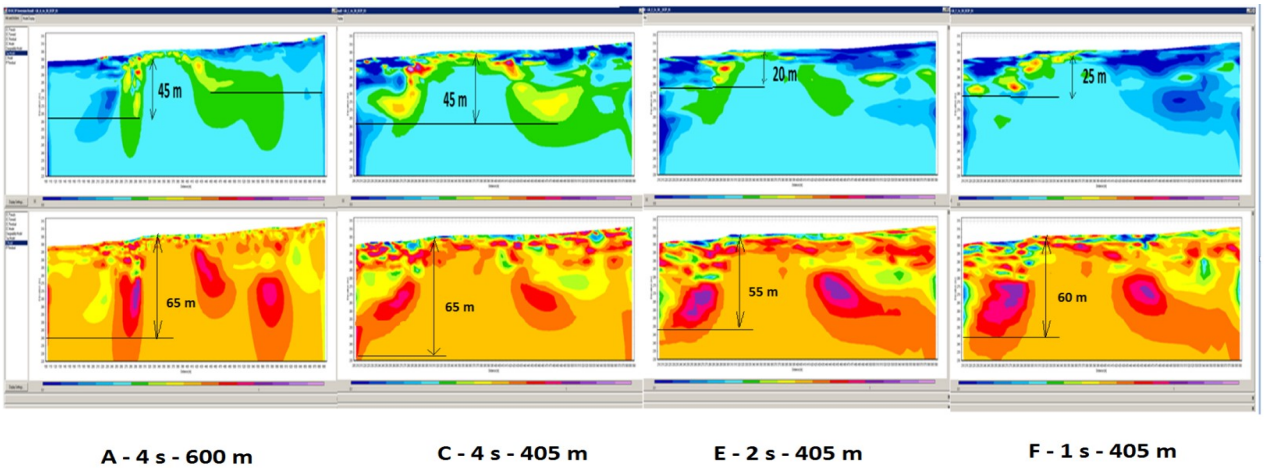

Figure 34. Comparison of Tau and C models in profile A- 4 s, C- 4 s, E- 2 s and F- 1s.

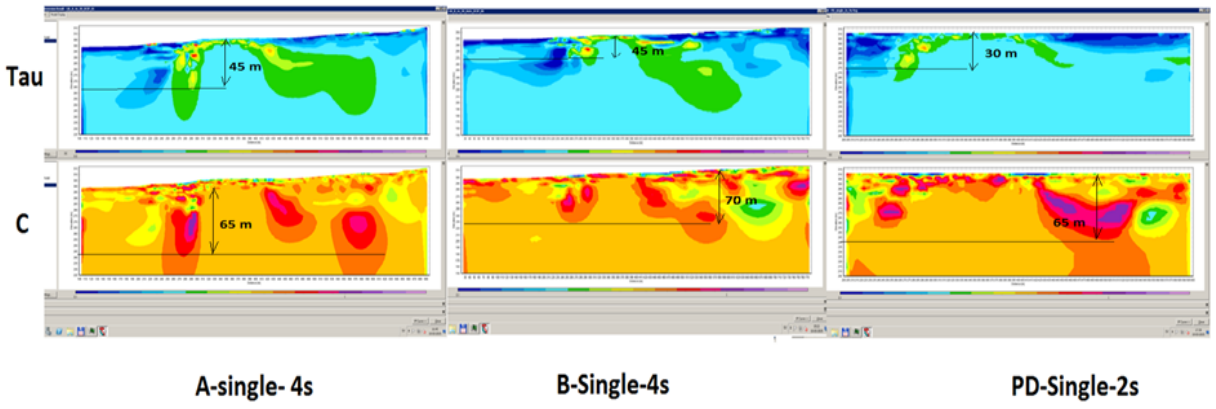

Figure 35. Comparison of Tau and C models in the single spread profiles; A, B and PD.

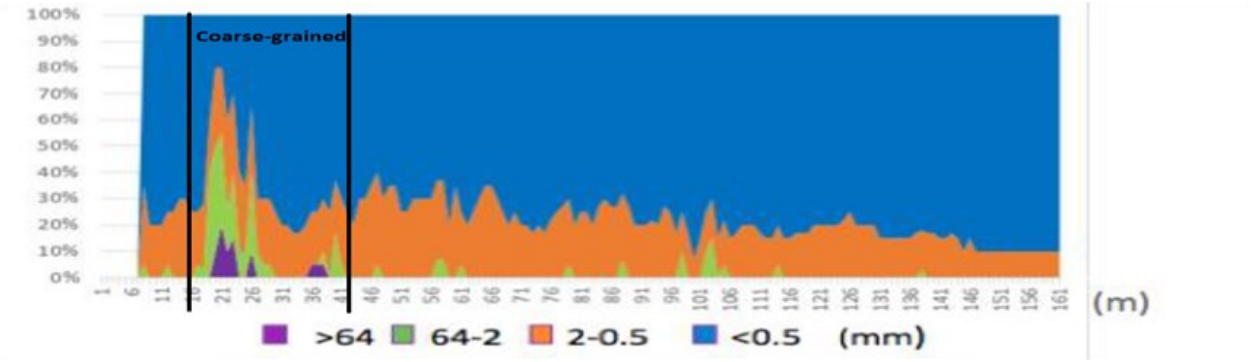

Figure 36. Graphic logging of core AIA 367, the Y-axis shows the clast abundance and X-axis shows the core in meter down the whole (Estholm, 2014).

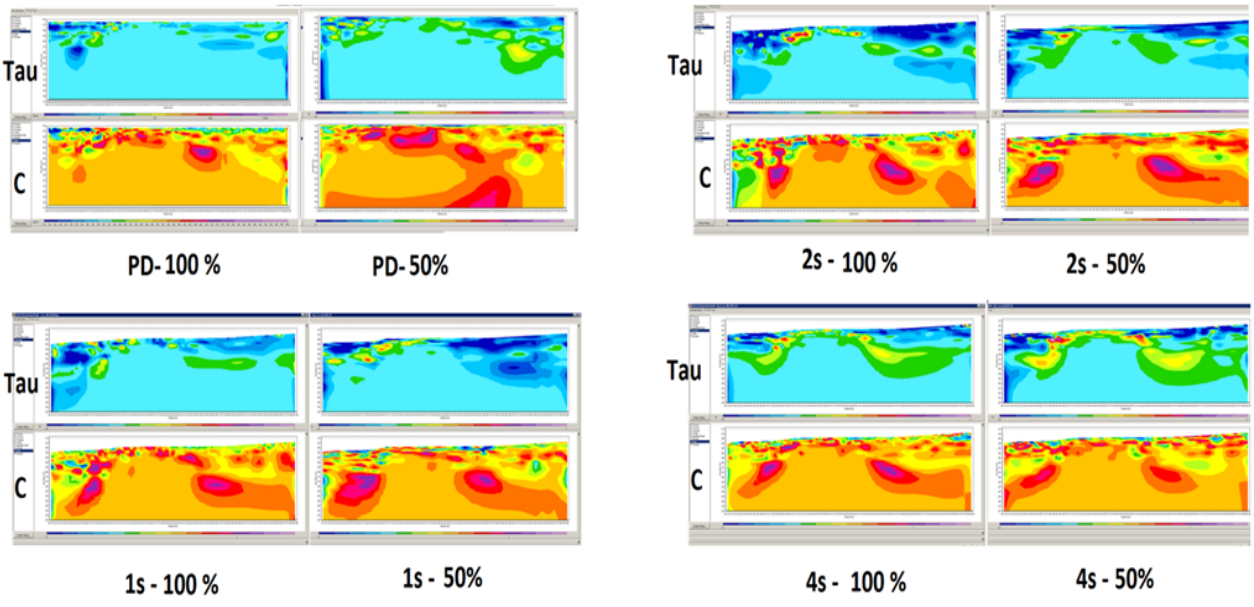

Figure 37. Comparison of Tau and C models in different waveforms (50% and 100 % duty cycle waveforms).

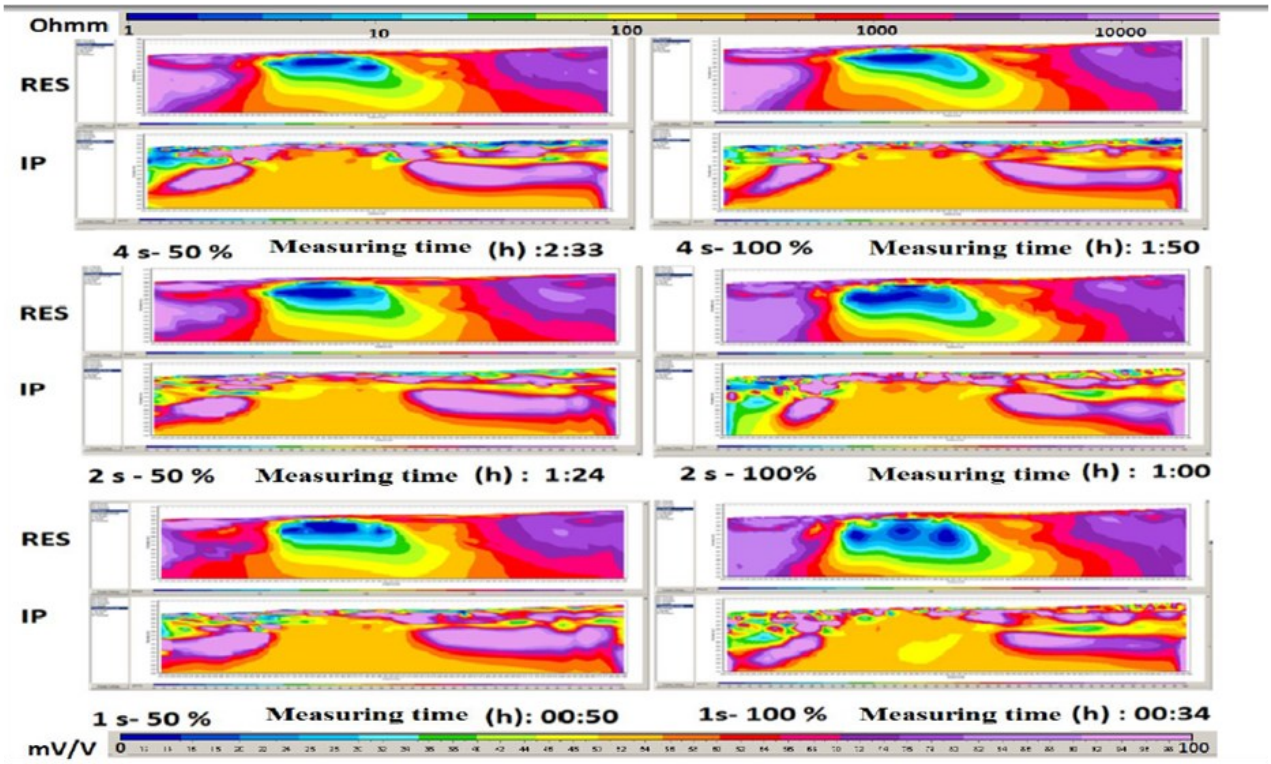

Figure 38. Inversion models for different injection times and waveforms. It appears that neither time bases nor waveforms do not have any significant effect on the final models in resistivity and IP.

6. Comparison with the previous survey

The model section from Geovista's resistivity/IP survey over line 3 is shown in Figure 39. The resistivity measurements were carried out with an ABEM LUND Imaging System and the data sets were inverted in Res2Dinv.

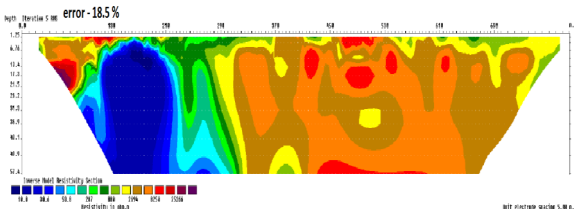

Figure 39. Geovista's 2D resistivity model over the same survey line of this study (Mattsson and Thunehed, 2013).

The 3D resistivity models were also presented in the Geovista's report, which cover the whole survey area in the planned open pit mine (see Figure 5). Figure 40 shows the single vertical slice of the 3D model over the selected survey line for this study (line 3) as well as the corresponding UTMX coordinates. The lateral extent of the mineralization zone is illustrated in Figure 41 over all of the 9 survey lines.

The suggested interval for the mineralization zone (dashed lines) from Geovista's models is from UTMX: 1727630 to UTMX: 1727775 which in our local coordinate it will be from 300 m to 453 m. This is almost the same interval that our resistivity models are suggesting for the ore zone (local: 305 m to 450 m).

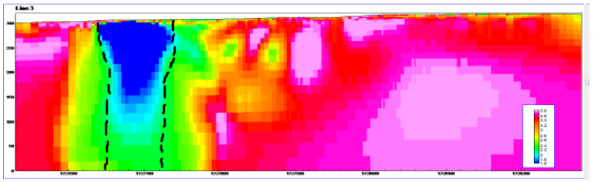

Figure 40. Vertical slice through 3D resistivity inversion model along profile 3 (logarithmic scale [Ωm]) (Mattsson and Thunehed, 2013).

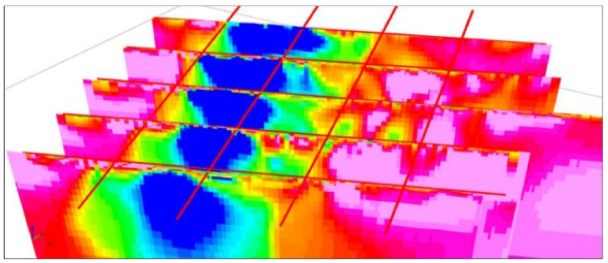

Figure 41. 3D view from south-east of vertical slices through 3D resistivity inversion models (Mattsson and Thunehed, 2013).

The resistivity models from this study inverted in Res2Dinv and AarhusInv are compared to Geovista's models in Figure 42 and 43. Since there are some distance differences in our measurements, it was tried to match the models based on the UTM coordinates.

Even though Geovista's inverted models present quite high residual (18.5%), they illustrate a same interval for the mineralization zone and bedrock as the models from this study.

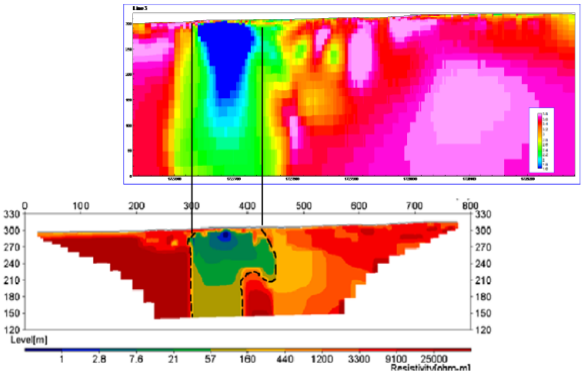

Figure 42. Comparison of resistivity models form this survey (Profile B - Res2Dinv) and Geovista's survey.

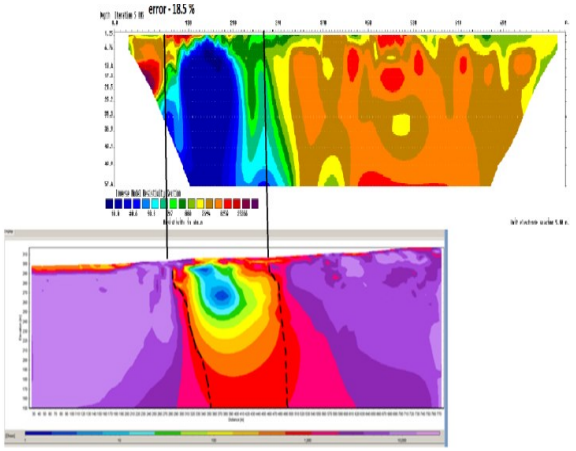

Figure 42. Comparison of resistivity models form this study (Profile B - AarhusInv) and Geovista's survey.

The suggested location of the mineralization zone, based on this study, is marked with a red circle, along the purple coordinate lines in Figure 44 in the Liikavaara area (local coordinates :between 305 to 450 m, UTMX between 1727635.95 to 1727771.843).

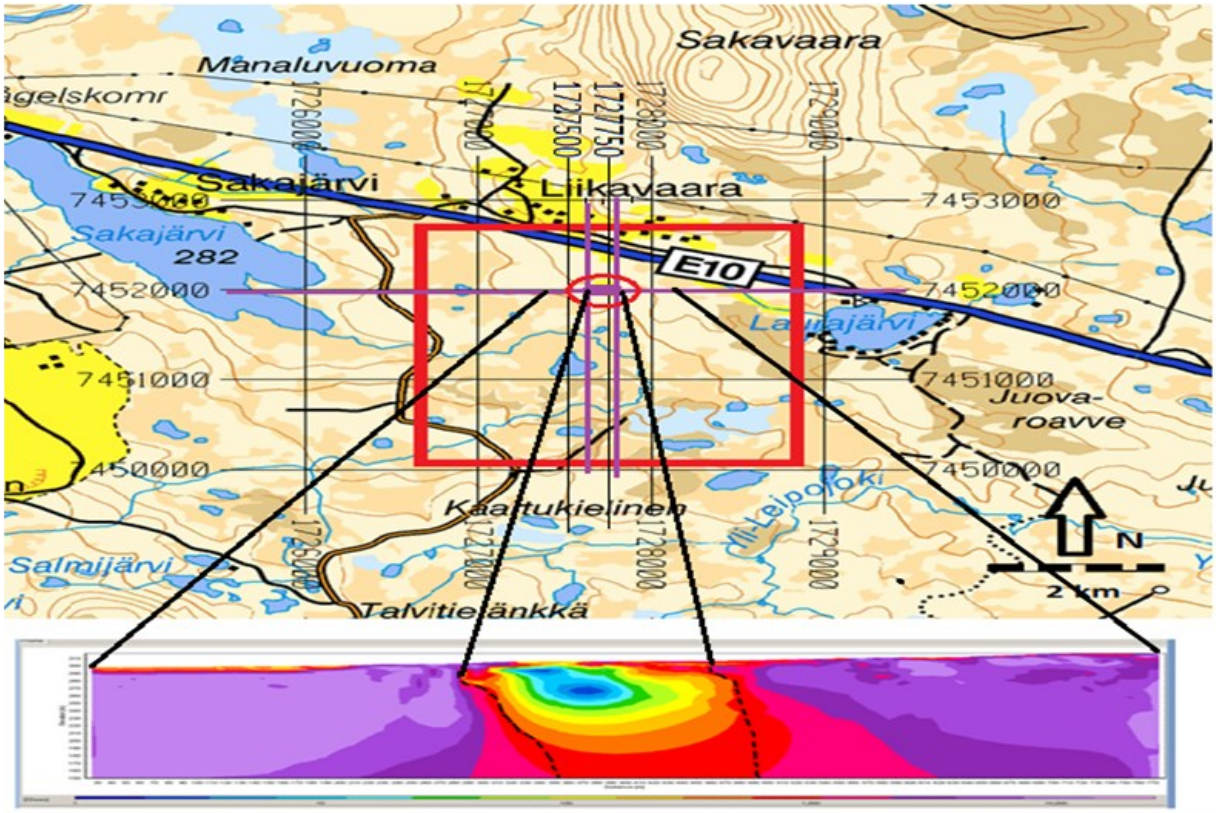

Figure 44. Suggested location of the mineralization zone (in UTM coordinates) based on the resistivity model in this survey.

7. Discussion

All the assessments in this section are based on the results that so far have been presented in the study:

- Mineral exploration

All the measurements over the Liikavaara mineralization zone are inverted in two different softwares; Res2Dinv and AarhusInv and both softwares clearly display the target zone. However, there are some possibilities (ex. filtering data, applying 100% duty cycle waveforms etc.) and also extra information (parameter C and Tau) which can be gained only in Aarhus Workbench software.

All of the resistivity models represent the mineralization zone in; local between 305 to 450 m, UTMX between 1727635.95 to 1727771.843, with approximate depth of 130 m below the surface. The very high conductive zone, in the central part of the mineralization zone, is supposed to be more iron rich than the other parts which shows lower conductivity in which by getting further from the core of the zone, the proportion of copper/iron is increasing until the border of host rock wall.

The IP models suggest a halo of disseminated ore which is surrounding the ore zone (local 240 to 305 m; UTMX 1727575.036 to 1727635.95 and local 410 to 620 m; UTMX 1727735.006 to 1727931.436) deep down to 70 m. The other two parameters Tau and C also confirm the presence of disseminated ores in different textures (grain size and grain size distribution) and probably presence of gold, copper and zinc in the areas with anomaly in both parameters. All the data sets were compared with the previous survey and it was well-matched with the identified interval for the mineralization zone and the host rock.

- Data quality

The mineralization segment is determined by remarkably highly conductive material (sulfides). This high conductivity results in very small potential differences reading between the potential electrodes and this leads to some highly disturbed decay curves in the IP measurements as it can be seen in the 'Raw data presentation' section. This condition made the comparison difficult and more ambiguous. Thus comparison of measured data over the host rock could be more helpful.

Coupling effects are another problematic phenomenon which could affect the quality of IP curves during the measurements. In this study both types of electromagnetic coupling (inductive and capacitive coupling) are expected to affect the IP data due to the presence of a highly conductive zone. It was attempted to reduce the influence of capacitive coupling by separating current and potential cables. As result, the quality of IP curves improved in some cases specifically in the first time windows (see Figure 21). As illustrated in Figures 21, 22 and 23 the single spreads have a bigger range of dispersion for the decay curves, in which some have been exceeded 10000 mV/V, such noisy curves can be also seen in the separated spreads but in a limited range in comparison with the single spreads.

The two different arrays that were carried out in the field were compared from different point of view. The multiple- gradient array generally presents a better data quality in both IP curves and the residual of the final models, whilst in the pole-dipole array a huge number of disturbed curves were presented in the raw data and more filtering was needed. However, the penetration depth was much higher, in which the 400 m profile of pole dipole has almost the same penetration depth of 800 m profile in gradient array.

Generally, applying 100 % duty cycle waveform in some measurements gave us better results in the data quality, especially in the pole-dipole measurement. Based on the presented results; decreasing the time of measurement to half, higher signal to noise ration and consequently fewer noisy curves in raw data are the advantages of applying this type of waveforms (see presentation of IP curves in Workbench- page 35). However, not all the inversions residuals for this type of waveform show a better result than 50% duty cycle waveform. But this should be also considered that residual depends on different factors and can differ by changing some settings before the inversion. Thus residual should not be the only factor that we compare for evaluating the data quality.

Although different injection time does not show any effect on the final inversion models in resistivity and IP, parameters C and Tau show sensitivity for duration of time base. As it was shown in section 'Tau and C parameters'; decreasing the time base, causes diminished anomalies in Tau and partly in C, which is mainly due to two factors: 1) decreasing signal level with shorter acquisition time, and the tau/ C differences may be masked by ambient noise and 2) decreasing resolution on the spectral parameters with shorter acquisition time ranges, without changes in the relative noise content.

Whilst single or separated spreads or type of waveforms do not have any significant effect on these two parameters, except for the pole-dipole one, in which applying 50% duty cycle waveform, shows an artificial anomaly in C parameter.

8. Conclusions

This study shows that the acquired IP data are of higher quality when applying 100 % duty cycle waveform. This is significant almost in all the measurements.

Separation of current and potential cables also helped to increase the data quality to some extent. This improvement is more clear in the first time windows over the host rock and this is probably because the capacitive coupling is decreasing with time. However, the IP disturbance caused by the high conductive mineralization zone hardly improved (this zone may not be an ideal case to compare the data quality for different spreads).

Tau and C which are new parameters for interpretation of mineral texture can give us even more detailed information on the measured data.

Even though, different injection time does not show any effect on the final models in resistivity and IP, Tau & C parameters appear to be sensitive to the duration of current injections. Measurement with single/separated spreads or different waveforms does not have any significant effect on these two parameters.

Moreover correlation of sulfur content matched well with the inverted models in both softwares, which confirms the applicability of the DCIP method in mineral exploration.

Both softwares used in this study gave us a similar overview of the subsurface. Although Res2Dinv provides a convenient way for inverting resistivity and IP data, the possibility of inverting measurements in 100 % duty cycle waveform, modeling parameters Tau and C and filtering IP decay curves by user is now available only in AarhusInv /Workbench software.

9. Acknowledgments

First of all I would like to thank my supervisors, Torleif Dahlin (Engineering Geology, Lund university), Ulf Söderlund (Geocentrum, Lund University), and my co-supervisors Paal Ahnfelt (Boliden Mineral AB) and Per-Ivar Olsson (Engineering Geology, Lund university). Per Hedbolm and Jimmie Lahti from ABEM instrument AB who prepared extra equipments and help during the field work in Liikavaara, and special thanks to Gianluca Fiandaca from Aarhus University who provided us a great support for Workbench and AarhusInv software. I am also really grateful for this opportunity that Boliden AB Company (geophysical exploration department) provided for me to conduct my master thesis as a part of Liikavaara mining project. Finally I would like to say thank you to all at the department of Engineering Geology and Geology.

10. Reference

ABEM, 2012, Instruction Manual for Terrameter LS: Sweden.

Anderson, N., Croxton, N., Hoover, R., and Sirles, P., 2008, Geophysical Methods Commonly Employed for Geotechnical Site Characterization Washington, DC Transportation Research Board, p. 35.

Bertin, J., 1976, Experimental and Theoretical Aspect of Induced polarization Presentationm and application of the IP Method Case Histories, Volume 1: Berlin, p. 247.

Butler, D. K., 2005, Near surface geophysics, Tulsa, Oklahama, U.S.A, Society of exploration geophysicists, 723 p.:

Dahlin, T., and Leroux, V., 2012, Improvement in time-domain induced polarization data quality with multi -electrode systems by separating current and potential cables: Near Surface Geophysics, v. 10, p. 545-565.

Dahlin, T., and Zhou, B., 2006, Multiple-gradient array measurements for multichannel 2D resistivity imaging: Near Surface Geophysics, p. 113-123.

Estholm, M., 2014, Identification of the host rocks and environment of formation of Liikavaar

Cu-Au deposit Norrbotten Sweden [Bachelor thesis Bachelor]: Stockholm University, 31 p.

Fiandaca, G., Ramm, J., Binley, A., Gazoty, A., Christiansen, A. V., Auken, E., and 2013, Resolving spectral information from time domain induced polarization data through 2-D inversion: Geophysical Journal International v. 192, p. 631-646.

Hitzman, M., 2000, Iron oxide copper-gold deposits: What where when and whay, Australian Mineral Foundation: Adelaid, p. 9-25.

Jones, F., 2007, Geophysics foundations: Physical properties: Chargeability, UBC Earth and Ocean Sciences.

Loke, M. H., 2014, Tutorial : 2-D and 3-D electrical imaging surveys, http://www.geotomosoft.com, p. 172.

Malmqvist, D., and Parasins, D. S., 1972, Aitik Geophysical documentation of a third-generation copper deposit in north Sweden: Geoexploration v. 10, p. 149-200.

Martinsson, O., 2004, Geology and metallogeny of the northern Norrbotten Fe-Cu-Au-ore province, Luleå Sweden, Society of Economic Geologists Guidebook Series, 129-146 p..

Mattsson, H., and Thunehed, H., 2013, Deformation zone model for the planned Liikavaara open pit: S, GeoVista AB, p. 45.

Milsom, J., and Eriksen, A., 2011, Field Geophysics, A John Wiley and Sons, Ltd., Publication, 287 p.:

Monro, D., 1988, The geology and genesis of the Aitik copper–gold deposit Arctic Sweden [PHD PHD]: University of Wales College of Cardiff.

Morrison, and Gasperikova, 2012, DC Resistivity and IP field systems, data processing and interpretation: California Berkeley, University of California Berkeley Department of Earth and Planetary Science.

Olsson, P.-I., Dahlin, T., Fiandaca, G., and Auken, E., 2014, Measuring Time Domain Spectral IP in the Ontime – Decreasing Acquisition Time and Increasing Signal-to-noise Ratio, 20th European Meeting of Environmental and Engineering Geophysics: Athens, Greece.

Paul, C. R., 2006, Introduction to Electromagnetic Compatibility, Wiley Series in Microwave and Optical Engineering.

Pridmore, D. F., and Shuey, R. T., 1976, The electrialencal resistivity of galena, pyrite, and chalcopyrite: American Mineralogist, v. 61, p. 248-259.

Reynolds, J. M., 2011, An Introduction to Applied and Environmental Geophysics, Wiley-Blackwell, 710 p.

Sharma, P., 1997, Environmental and Engineering Geophysics, Cambridge, Cambridge University Press.

Sumner, J. S., 1976, Principles of induced polarization for geophysical exploration, Amesterdam, Elsevier Scientific Publishing Company, 277 p.:

Telford, W. M., Geldart, L. P., and Sheriff, R. E., 1990, Applied Geophysics, Cambridge Cambridge University Press, 792 p.:

Wanhainen, C., 2005, Origin and Evolution of the PalaeoproterozoicAitik Cu-Au-Ag Deposit, Northern Sweden [PHD Doctoral]: Luleå University of Technology.

Wanhainen, C., Broman, C., Martinsson, O., and Magnor, B., 2012, Modification of a Palaeoproterozoic porphyry-like system: Integration of structural, geochemical, petrographic, and fluid inclusion data from the Aitik Cu–Au–Ag deposit, northern Sweden: Elsevier, v. 48, p. 306-331.

Wightman, W. E., Jalinoos, F., Sirles, P., and Hanna, K., 2003, Application of Geophysical Methods to Highway Related Problems: Lakewood California, Central Federal Lands Highway Division.

Zweifel, H., 1976, AITIK - GEOLOGICAL DOCUMENTATION OF A DISSEMINATED COPPER DEPOSIT, Stockholm Sweden, C DAVIDSONS BOKTRYCKERI AB, C NR 720, 79 p.

11. Appendix

11.1 Logging data for boreholes 365, 364, 363,376 and 370:

Table 1. Logging data AIA 365 (120m)

Borehole 365	Rock type	Minerals	Common Structure	Sulfide content%
From 0 – 3.9 m	soil			
From 3.9 – 8.6 m	Biotite schist	Chalcopyrite, Pyrite, Pyrrhotite, Quartz, Scheelite	Weathered , Veins	1.59
From 8.6 – 13 m	Biotite schist	-"-	Fractured, Weathered , Veins	3.7
From 13 - 18 m	Biotite schist	-"-	Trace of minerals	1.83
From 18 - 23 m	Biotite schist	-"-	-"-	1.29
From 23 - 28 m	Biotite schist	-"-	-"-	0.81
From 28 – 33 m	Biotite schist	-"-	-"-	1.02
From 33 - 38 m	Biotite schist	-"-	Veins	1.49
From 38 – 43 m	Biotite schist	-"-	Veins	1.01
From 43 – 48 m	Biotite schist	Quartz , Calcite	Stripes	1.35
From 48 – 53 m	Biotite schist	Chalcopyrite, Pyrite, Pyrrhotite, Quartz, Scheelite	Veins	1.81
From 53 – 58 m	Andesite	Chalcopyrite, Pyrite, Pyrrhotite, Quartz, Biotite	Altered	0.81
From 58 – 63 m	Andesite	Chalcopyrite, Pyrite, Pyrrhotite, Quartz, Biotite, Calcite	Altered, Stripes	1.36
From 63 – 68 m	Andesite	-"-	-"-	1.38
From 68 – 73 m	Andesite	-"-	-"-	1.12
From 73– 78 m	Andesite	Chalcopyrite, Pyrite, Pyrrhotite, Quartz, Biotite, Calcite, Sheelite	-"-	0.96
From 78- 81m	Andesite	-"-	-"-	0.85
From 81- 83.4	Andesite	Chalcopyrite, Pyrrhotite, Quartz, Biotite-Amphibo, Sheelite	-"-	0.92
From 83.4 -87.7m	Biotite schist	Chalcopyrite, Pyrite, Pyrrhotite, Quartz, Ni minerals , Sheelite	Stripes, Trace of minerals	1.11
From 87.7- 92 m	Biotite schist	Chalcopyrite, Pyrite, Pyrrhotite, Quartz, Calcite, Sheelite	Stripes, Veins	2.52
From 92- 97 m	Biotite schist	-"-	Fractured, Weathered , Stripes	1.13
From 97- 102 m	Biotite schist	-"-	Weathered , Stripes	1.19
From 102-106.5	Biotite schist	-"-	-"-	1.14
From 106.5-111	Biotite schist	-"-	Stripes, Veins	1.48
From 111-116	Biotite schist	-"-	-"-	1.62
From 116-121	Biotite schist	Chalcopyrite, Pyrite, Pyrrhotite, Quartz, Sheelite	Veins	1
From 121-126	Biotite schist	-"-	-"-	1.35
From 126-131	Biotite schist	Pyrite, Pyrrhotite, Quartz, Sheelite	Trace of minerals	0.98
From 131-136	Biotite schist	-"-	-"-	1.05
From 136-141	Biotite schist	Chalcopyrite, Pyrite, Pyrrhotite, Quartz, Sheelite	Veins	1.24

Table 2. Logging data AIA 364

Borehole 364	Rock type	Minerals	Common Structures	Sulfide content%
From 0 - 6.9 m	soil			
From 6.9 – 12 m	Turbidite	Pyrite, Quartz, Calcite, Epidote	Altered, Weathered, Stripes, Spots, Fractured, Weak Druse	0.25
From 12 – 17 m	Turbidite	-"-	-"-	0.22
From 17 – 21 m	Turbidite	-"-	-"-	0.27
From 21 – 24 m	Turbidite	-"-	-"-	0.17
From 24 – 29 m	Turbidite	Pyrite, Microcline, Calcite, Epidote	Weathered, Stripes, Fractured	0.18
From 29 – 34 m	Turbidite	Pyrite, Quartz, Calcite, Epidote	Stripes, Spots	0.07
From 34 – 39 m	Turbidite	-"-	-"-	0.1
From 39 – 43 m	Turbidite	Pyrite, Microcline, Calcite, Epidote	Altered, Weathered, Stripes, Spots, Fractured	0.12
From 43 – 48 m	Turbidite	-"-	-"-	0.06
From 48 - 53 m	Turbidite	Microcline, Quartz, Calcite, Epidote	Stripes, Fractured, Altered	0.08
From 53 – 58 m	Turbidite	-"-	-"-	0.11
From 58 – 62 m	Turbidite	Microcline, Quartz, Calcite, Epidote, Pyrite	Weathered, Fractured, Stockwork/net	0.08
From 62 – 67 m	Turbidite	-"-	-"-	0.1
From 67 – 72 m	Turbidite	-"-	-"-	0.21
From 72-82	Turbidite	Microcline, Quartz, Chalcopyrite, Epidote, Pyrite	Weathered, Fractured, Altered	0.07

Table 3. Logging data AIA 363

Borehole **363**	Rock type	Minerals	Common Structures	Sulfide content%
From 0 – 4.6 m	soil			
From 4.6 – 9.6 m	Turbidite	Epidote,Chalcopyrite, Pyrite, Quartz, Calcite	Weathered, Fractured, Stockwork/ net	0.24
From 9.6 – 13.2 m	Turbidite	-"-	-"-	0.25
From 13.2 – 17 m	Turbidite	Epidote, Pyrite	Weathered, Fractured	0.09
From 17 - 22 m	Turbidite	Pyrite	Weathered, Fractured	0.38
From 22 – 27 m	Turbidite	Microcline, Quartz, Calcite, Epidote, Pyrite	Altered, Weathered, Fractured, Stockwork/net	0.14
From 27 – 30 m	Turbidite	-"-	-"-	0.06
From 30 – 33.2 m	Turbidite	-"-	-"-	0.29
From 33.2 – 37.8m	Aplite+ Pegmatite veins	Microcline, Tourmaline, pyrite	Altered, veins Weathered, Fractured, Stripes	0.42
From 37.8 – 40.5m	Turbidite	Microcline, pyrite	Weathered, Fractured	0.02
From 40.5 – 45 m	Turbidite	pyrite	Weathered	0.04
From 45 – 49 m	Turbidite	Quartz	Weathered, Fractured, Stripes	0.02
From 49 – 54 m	Turbidite	Quartz, Calcite, Epidote, Pyrite	Altered, Fractured, Stripes	0.03
From 54 – 57 m	Turbidite	-"-	-"-	0.07
From 57 – 61.7 m	Conglomerate	Pyrite	Weathered	0.07
From 61.7 – 64.9m	Turbidite	Epidote	Altered	0.06
From 64.9 – 68 m	Conglomerate + Pegmatite veins	Epidote, Pyrite	Weathered, veins	0.08
From 68 – 71 m	Conglomerate	-"-	-"-	0.03

Table 4. Logging data AIA 367

Borehole **367**	Rock type	Minerals	Structure	Sulfide content%
From 0 – 5.6 m	soil			
From 5.6 – 7.5 m	Conglomerate	Epidote, Pyrite Chalcopyrite, Microcline	Altered	0.18
From 8 – 12.5 m	Conglomerate	Epidote, Pyrite Calcite, Microcline	Altered, Weathered, Fractured, Stripes	0.19
From 12.5 – 17.5 m	Conglomerate	Epidote, Pyrite Chalcopyrite, Microcline, Calcite	Weathered, Fractured, Stripes	0.3
From 17.5 – 22.5 m	Conglomerate	Epidote, Pyrite Chalcopyrite, Microcline, Calcite	Altered, Stripes	0.18
From 22.5 – 27.5m	Conglomerate	Epidote, Pyrite Chalcopyrite, Microcline, Quartz	Stripes	0.39
From 27.5 – 32 m	Conglomerate	Epidote, Pyrite Chalcopyrite, Quartz, Microcline, Calcite	Stripes, Altered	0.3
From 32 – 37 m	Turbidite	Pyrite, Quartz, Microcline, Calcite	Stripes	0.1
From 37 – 42 m	Turbidite + Pegmatite veins	Epidote, Pyrite Chalcopyrite, Quartz, Microcline, Calcite	Stripes, Veins	0.3
From 42 – 47 m	Turbidite	Pyrite Chalcopyrite, Quartz, Microcline, Calcite	Stripes	0.11
From 47 – 57 m	Turbidite	Pyrite, Epidote Quartz, Microcline, Calcite	Stripes	0.05
From 57 – 61 m	Turbidite	Pyrite Chalcopyrite, Quartz, Microcline, Calcite	Weak Altered and veins	0.09
From 61 – 66 m	Turbidite	Pyrite, Epidote, Microcline, Calcite	Altered, Stripes	0.1
From 66 – 70 m	Turbidite	-"-	-"-	0.1

Table 5. Logging data AIA 370 (Hanging wall):

Borehole **370**	Rock type	Minerals	Common Structure	Sulfide content
From 0 – 5.7m	soil			0
From 5.7 – 19m	Conglomerate	Calcite	Druse	0
From 19 – 27 m	Conglomerate	Epidote, Micro-cline, Calcite	Spots	0
From 27 - 29 m	Conglomerate	Quartz	Weak veins	0
From 29 – 44 m	Conglomerate	Quartz	Weak veins	0
From 44 – 56 m	Conglomerate	Epidote, Microcline	Altered, Weathered	0
From 56 – 70 m	Conglomerate	Epidote, Quartz	Altered, Fractured	0

11.2 Geometry factors and penetration depth for multiple gradient arrays

Table 7. Median depth penetration (focus depth) and geometry factor for different electrode arrays. *L* is total lay-out length excluding remote electrodes, and ***a*** the smallest inter electrode distance. Separation factor's' is defined as the maximum number of potential readings for a single current injection (in this case we have s=7) and n-factor is defined as the smallest relative spacing between a current electrode and a potential electrode. This table is based on an electrode spacing of one, but it scales linearly so the same relative relations hold for other layout lengths (Dahlin pers.communication).

Array	L	a	s-factor	n-factor	Median depth	Geometry factor
Multiple gradient	1	0.1111	7	1	0.060	1.35
Multiple gradient	1	0.1111	7	2	0.113	3.66
Multiple gradient	1	0.1111	7	3	0.166	5.98
Multiple gradient	1	0.1111	7	4	0.190	6.98

11.3 Inverted model sections (2D Inversions)

11.3.1 Res2Dinv results

11.3.1.1 Multiple Gradient- Single spread

A- Single spread, IP 4s , 50% duty cycle waveform

RES::

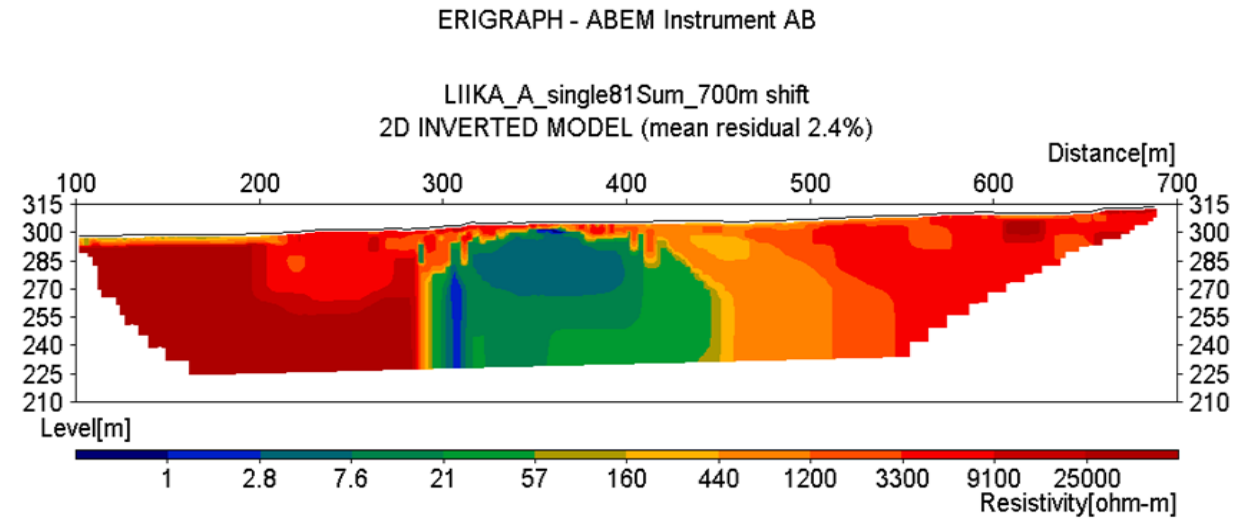

Data file: LIIKA_A_single81Sum_700m shift Model file: LIIKA_A_single81Sum_700m shift.RHO (mean residual = 2.

IP :

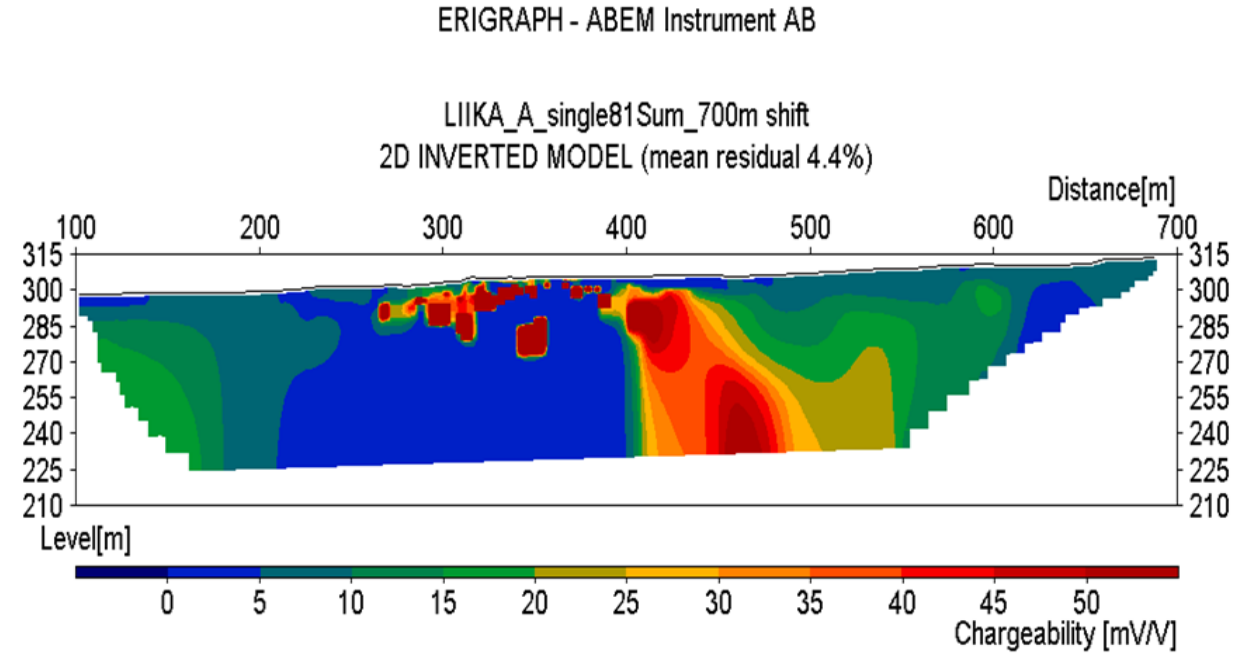

Data file: LIIKA_A_single81Sum_700m shift Model file: LIIKA_A_single81Sum_700m shift.RHO (mean residual = 4.

B- Single spread , 800m XL , IP 4s , 50% duty cycle waveform, Profile length: 800m

RES:

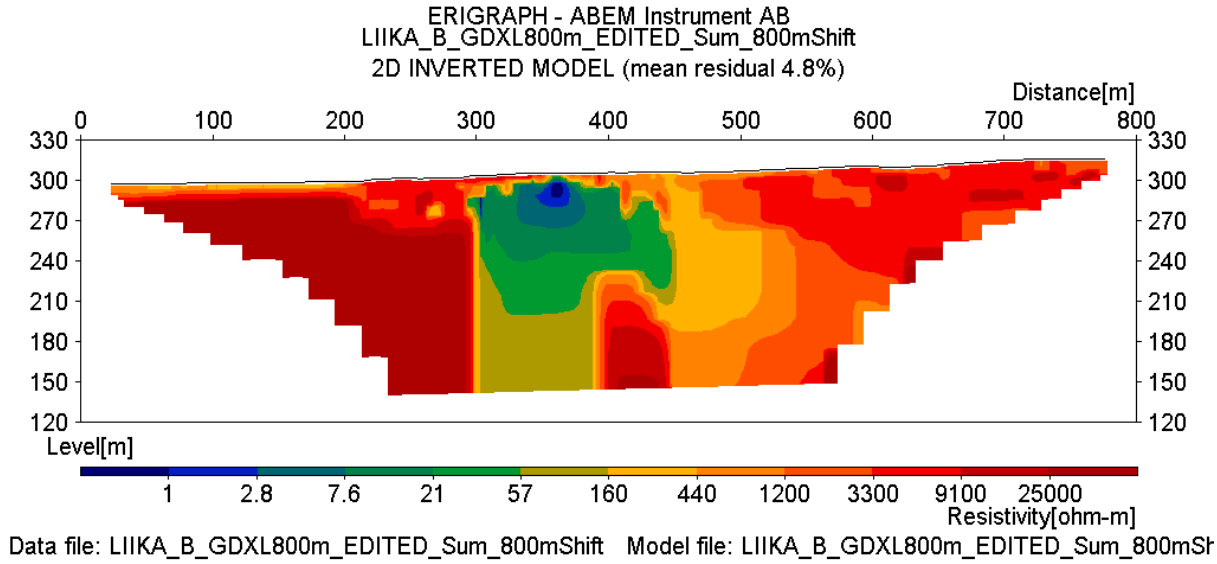

IP:

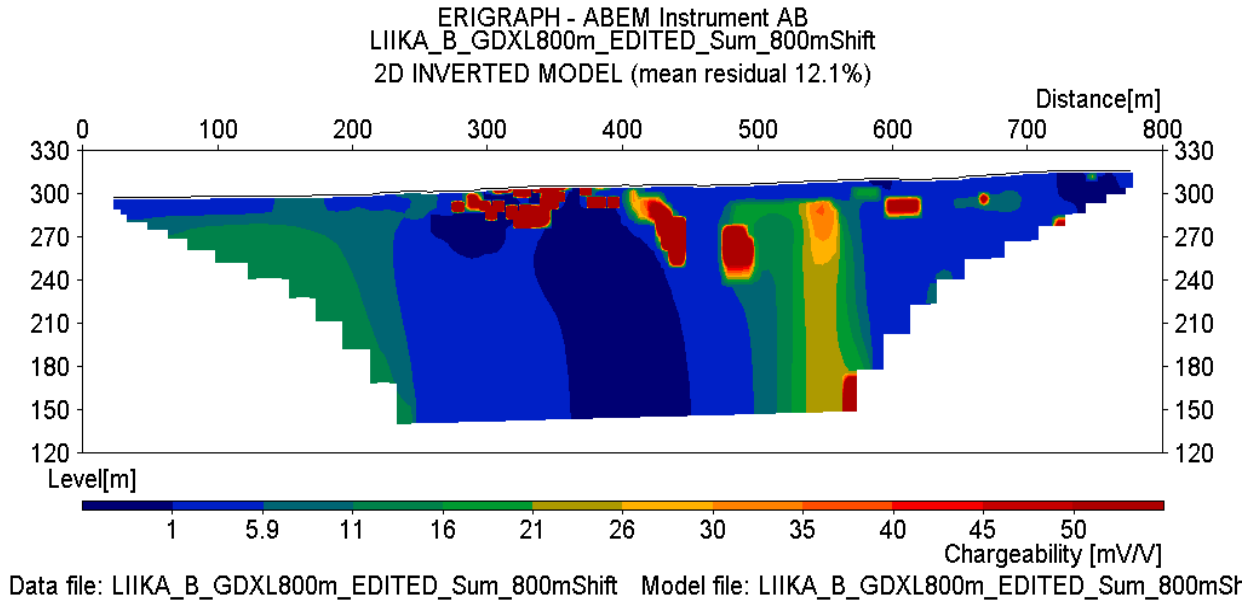

11.3.1.2 Multiple Gradient- Separated spreads

C - Separate spread , IP 4s, 50% duty cycle waveform, Profile length: 405m

RES:

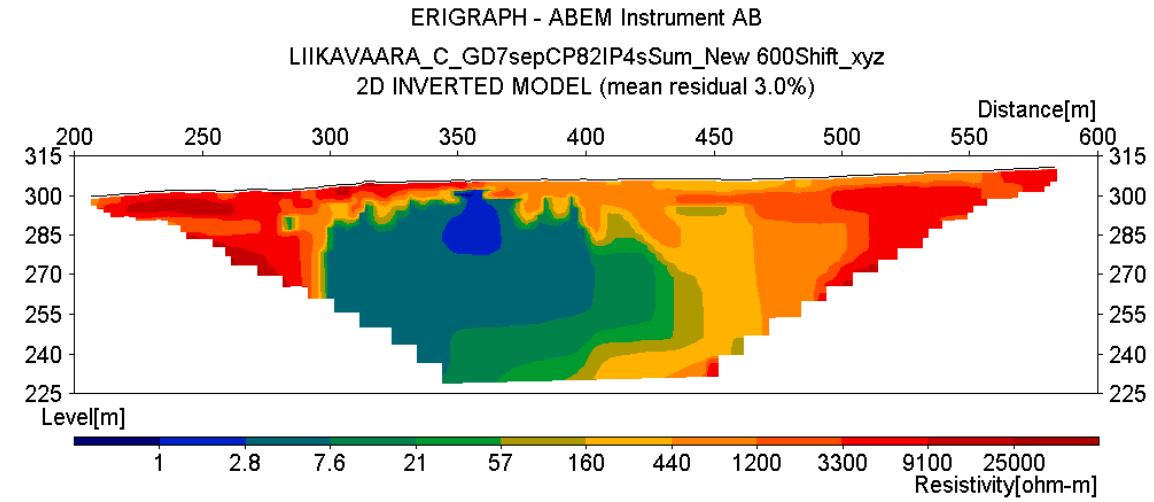

Data file: LIIKAVAARA_C_GD7sepCP82IP4sSum_New 600Shift_xyz Model file: LIIKAVAARA_C_GD7sepCP82IP4

IP:

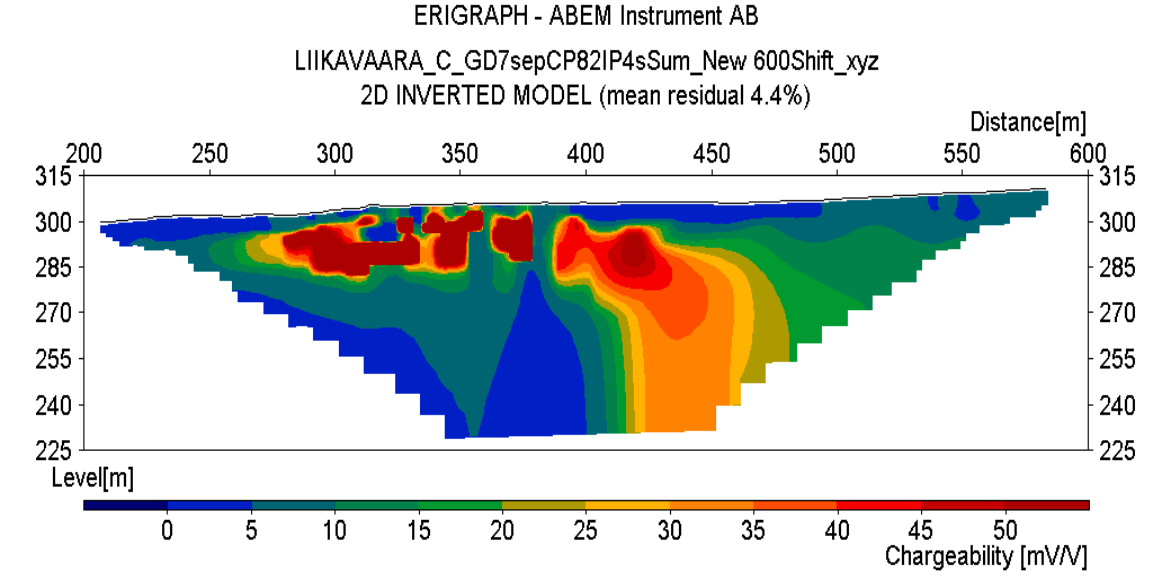

Data file: LIIKAVAARA_C_GD7sepCP82IP4sSum_New 600Shift_xyz Model file: LIIKAVAARA_C_GD7sepCP82IP4

E - Separate spread , IP 2s, 50% duty cycle waveform , Profile length: 405 m

RES:

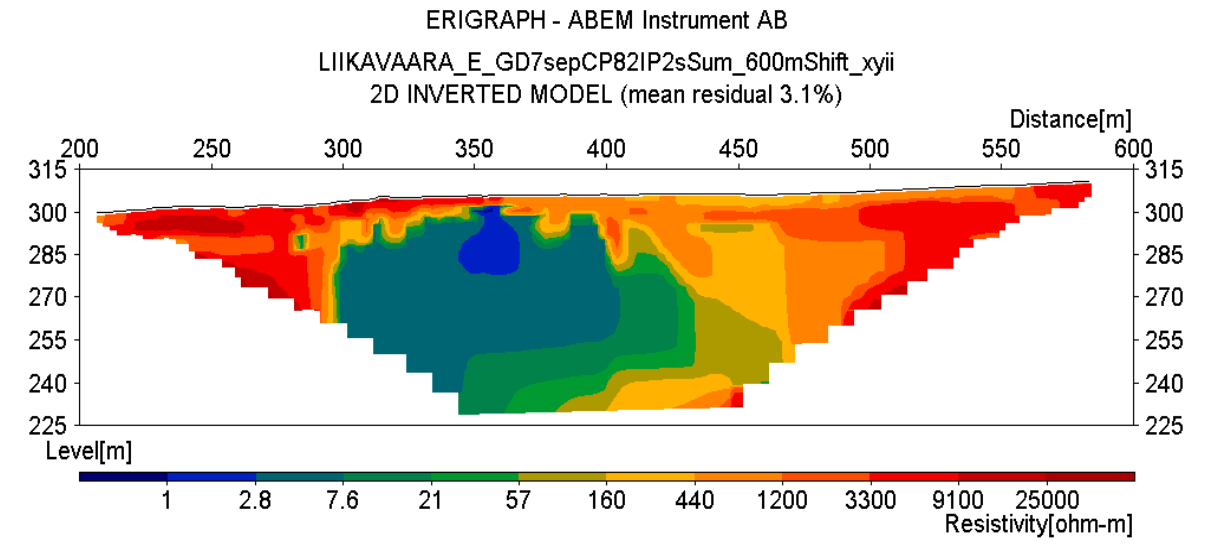

Data file: LIIKAVAARA_E_GD7sepCP82IP2sSum_600mShift_xyii Model file: LIIKAVAARA_E_GD7sepCP82IP2sSu

IP:

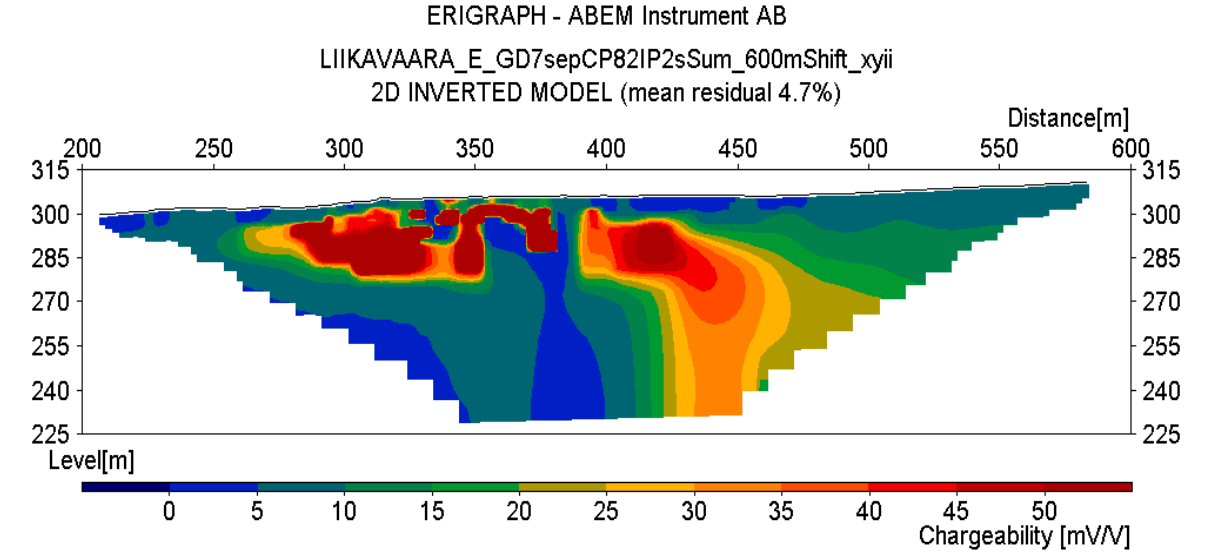

Data file: LIIKAVAARA_E_GD7sepCP82IP2sSum_600mShift_xyii Model file: LIIKAVAARA_E_GD7sepCP82IP2sSu

F - Separate spread , IP mode 1s , 50% duty cycle waveform, Profile length: 405 m

RES:

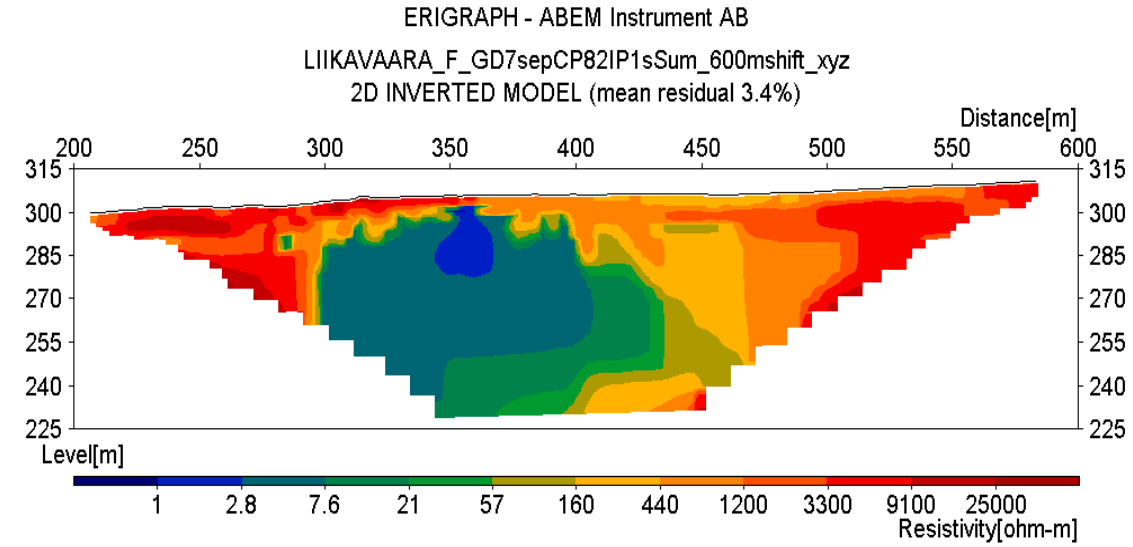

Data file: LIIKAVAARA_F_GD7sepCP82IP1sSum_600mshift_xyz Model file: LIIKAVAARA_F_GD7sepCP82IP1sSu

IP:

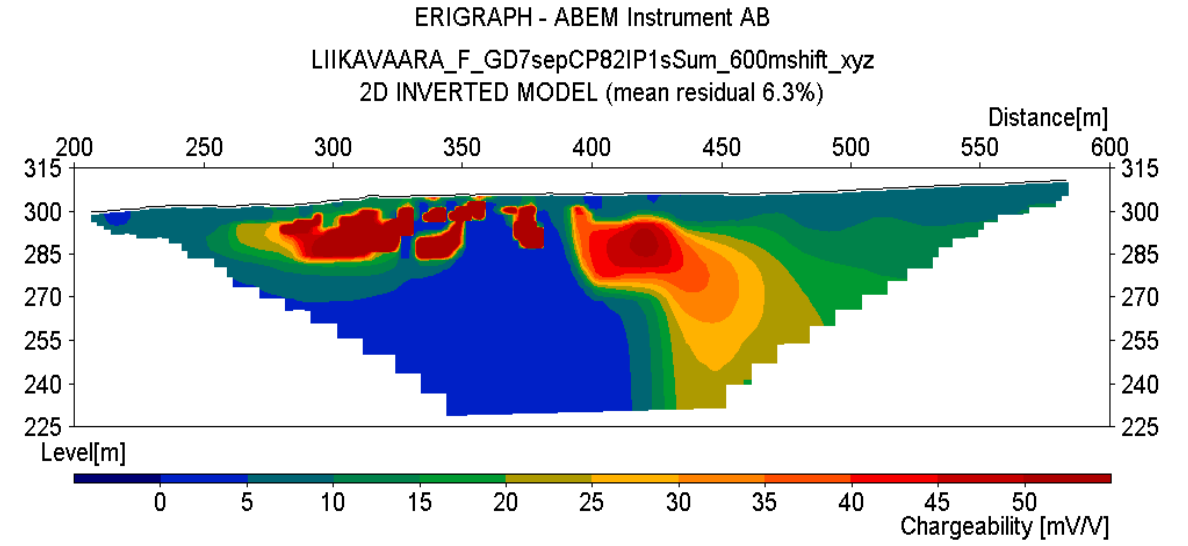

Data file: LIIKAVAARA_F_GD7sepCP82IP1sSum_600mshift_xyz Model file: LIIKAVAARA_F_GD7sepCP82IP1sSu

11.3.1.3 Pole-Dipole - Single spread

PD1 - Single spread, IP 2s , (50% duty cycle waveform) , Profile length: 400 m

RES:

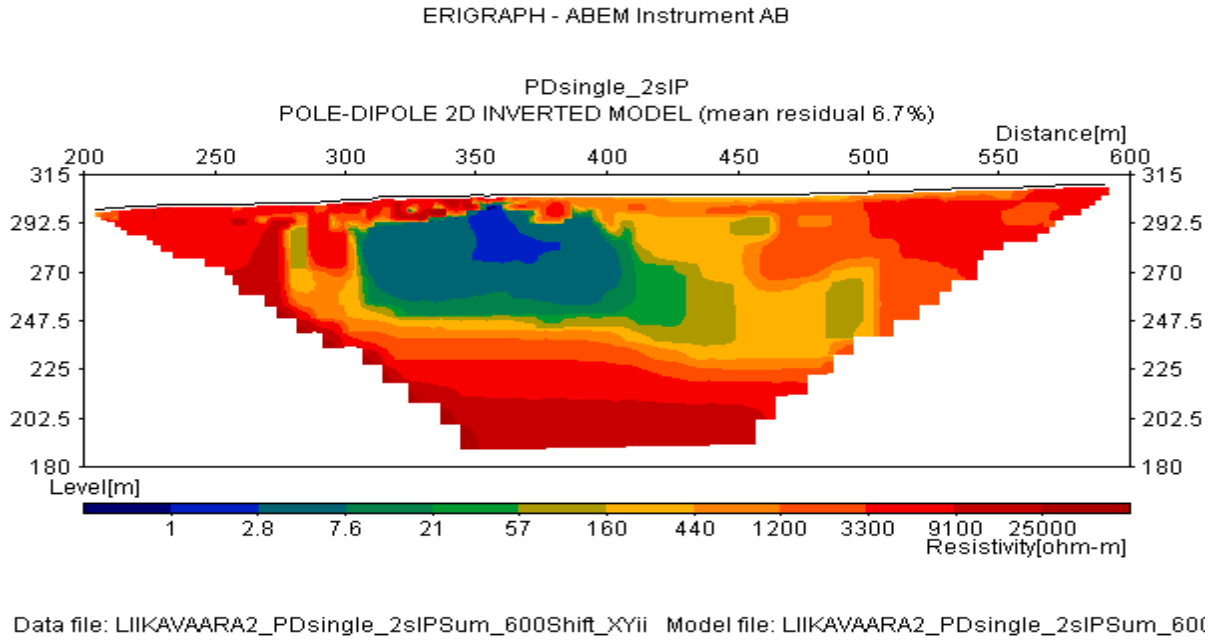

Data file: LIIKAVAARA2_PDsingle_2sIPSum_600Shift_XYii Model file: LIIKAVAARA2_PDsingle_2sIPSum_60(

IP:

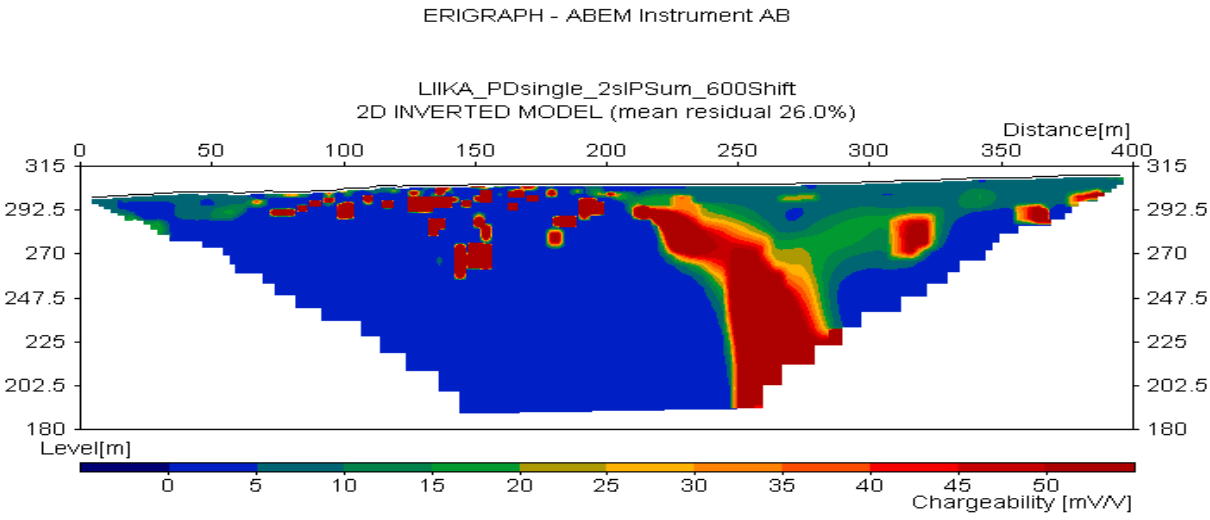

Data file: LIIKA_PDsingle_2sIPSum_600Shift Model file: LIIKA_PDsingle_2sIPSum_600Shift.RHO (mean residu

11.3.1.4 Pole-Dipole - Separate spread

PD2— Separate spread, IP 2s, (50% duty cycle waveform), Profile length: 405 m

RES:

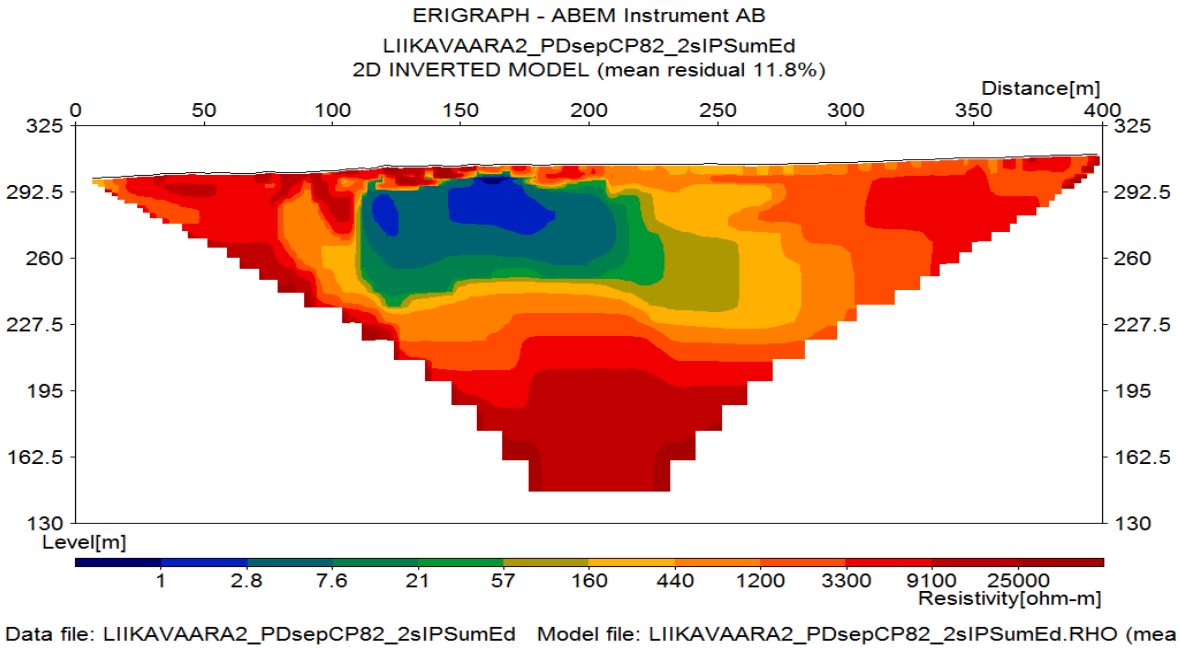

Data file: LIIKAVAARA2_PDsepCP82_2sIPSumEd Model file: LIIKAVAARA2_PDsepCP82_2sIPSumEd.RHO (mea

IP:

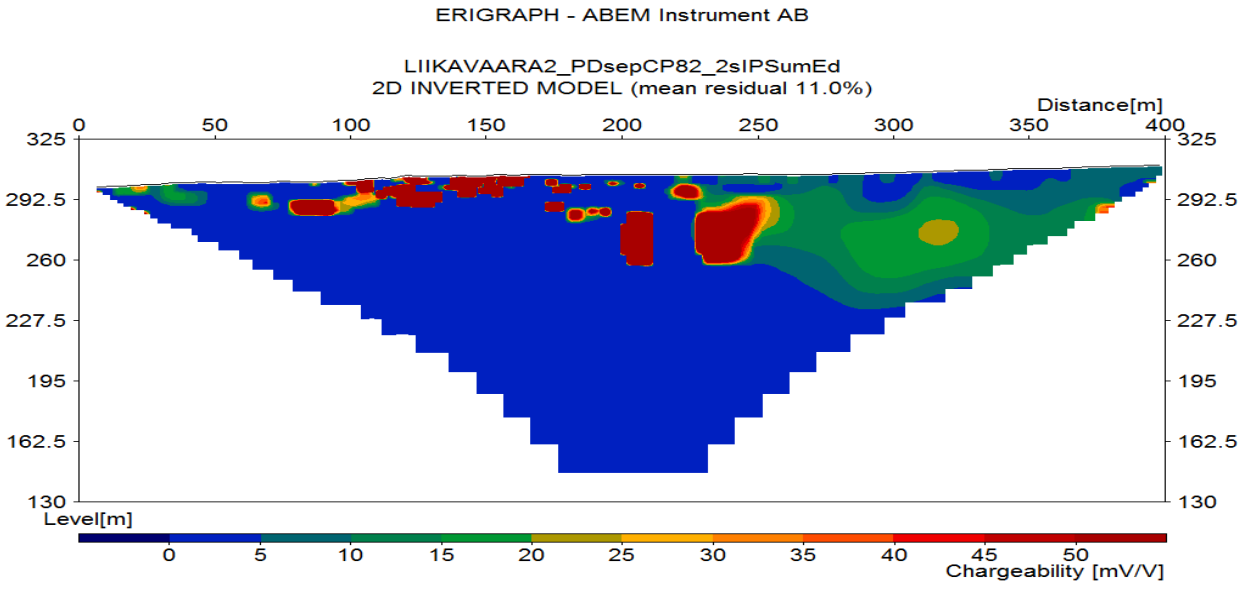

Data file: LIIKAVAARA2_PDsepCP82_2sIPSumEd Model file: LIIKAVAARA2_PDsepCP82_2sIPSumEd.RHO (mea

11.3.2 AarhusInv results

11.3.2 .1 Multiple Gradient-Single spread

A - Single spread, IP 4s , 50% duty cycle waveform, Profile length: 700m

DC and IP models:

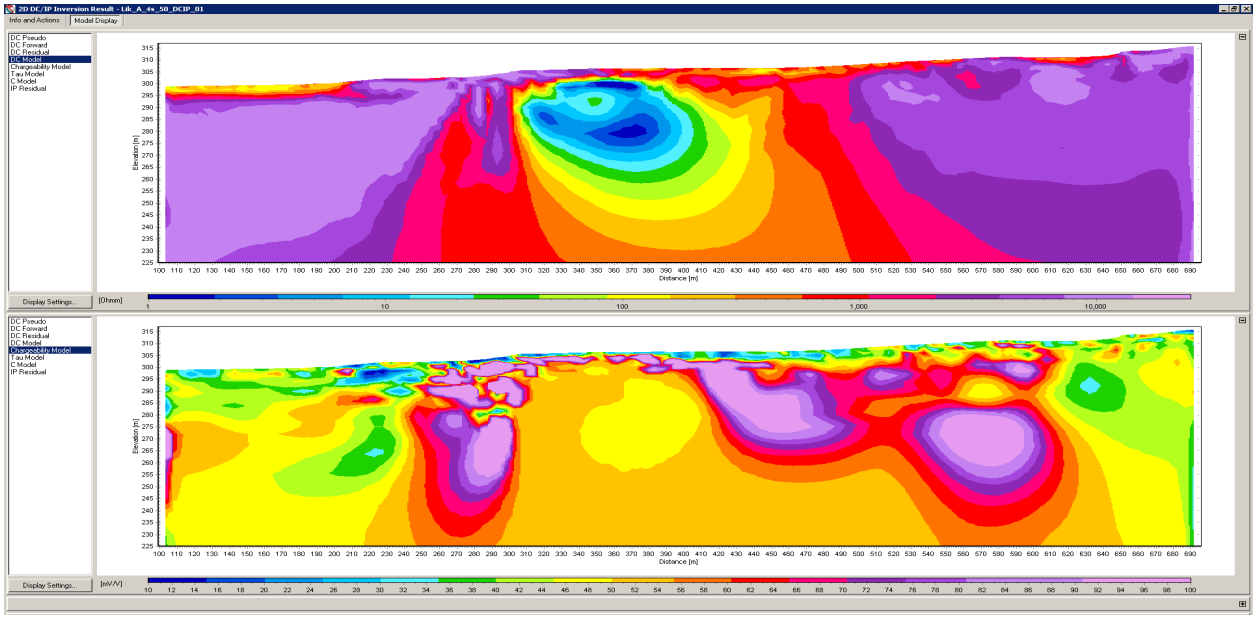

DC Residual:11.02 IP Residual:2.37

Tau and C models:

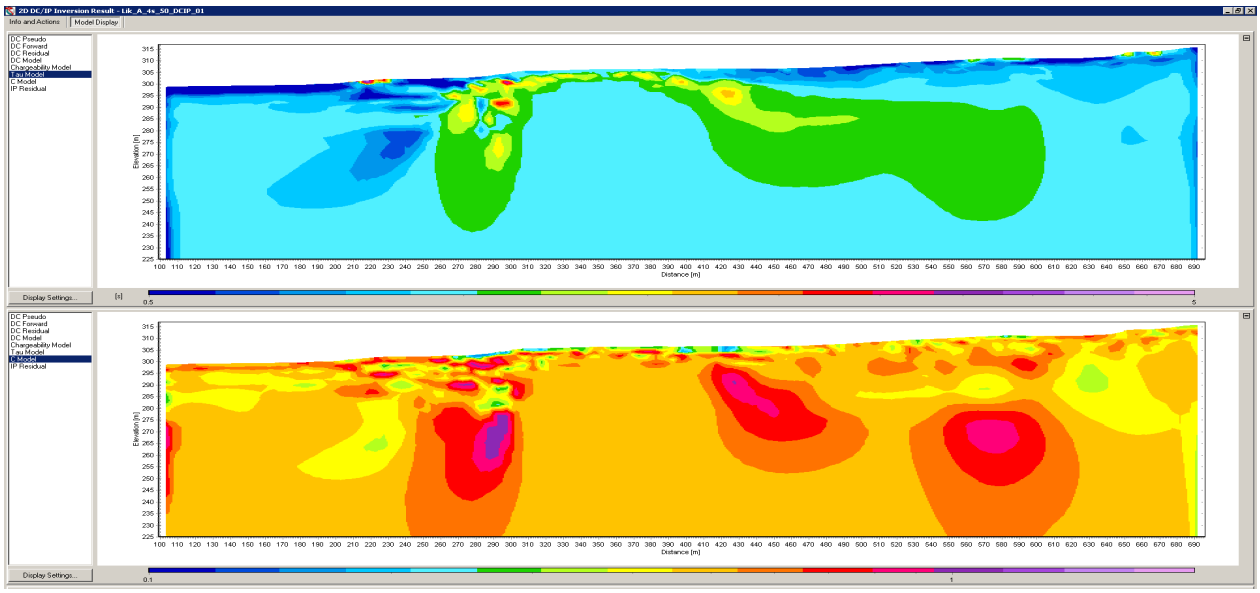

B—Single spread , 800m XL , IP 4s , 50% duty cycle waveform, Profile length: 800m

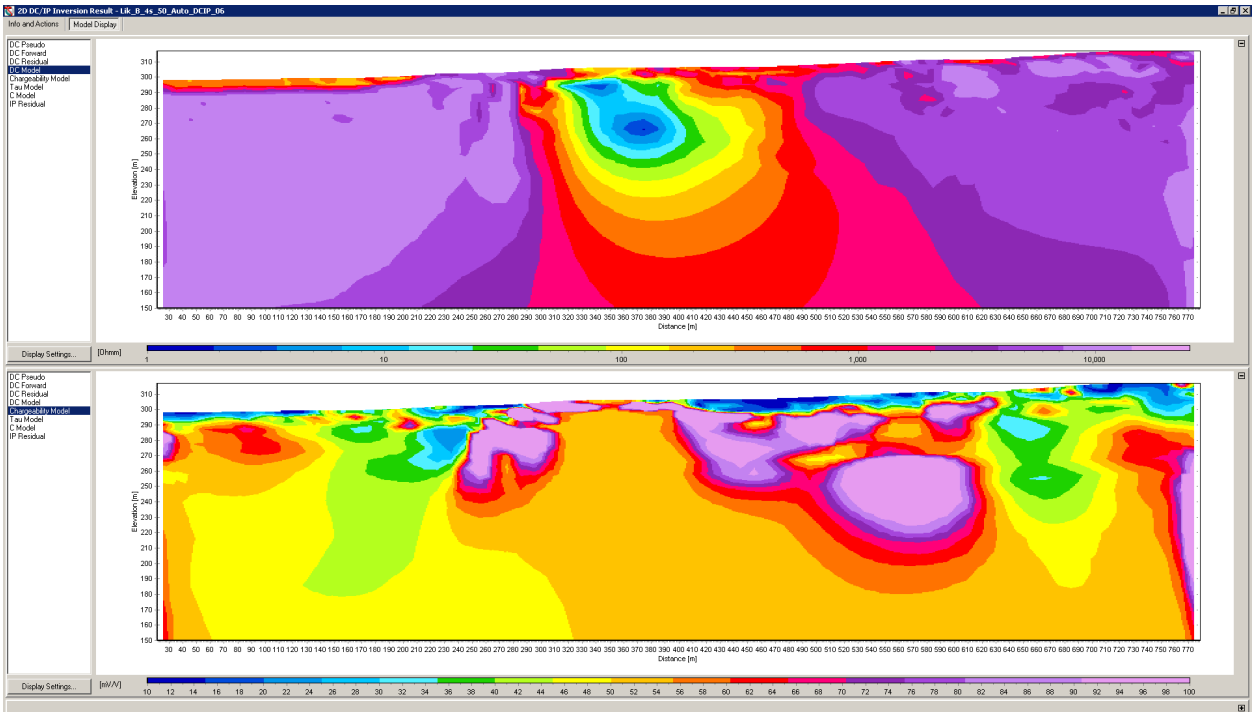

DC:11.83 IP:2.51

Tau and C modeling:

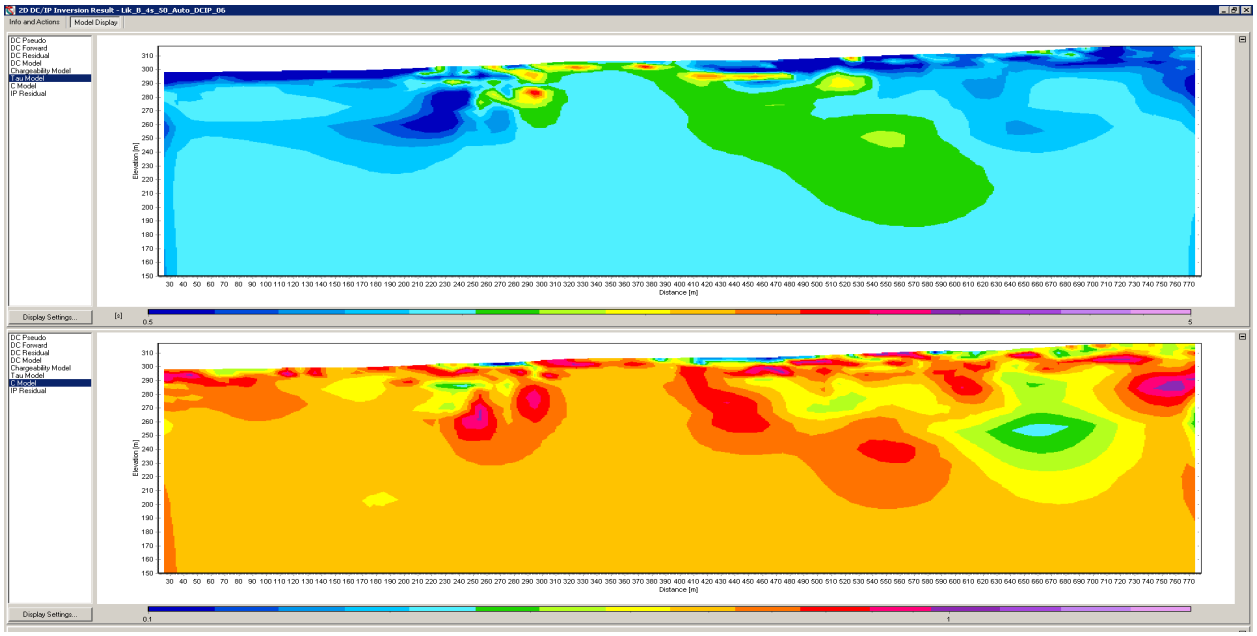

11.3.2 .2 Multiple Gradient-Separate spread

Separate spread , IP 4s, 50% duty cycle waveform, Profile length: 405m

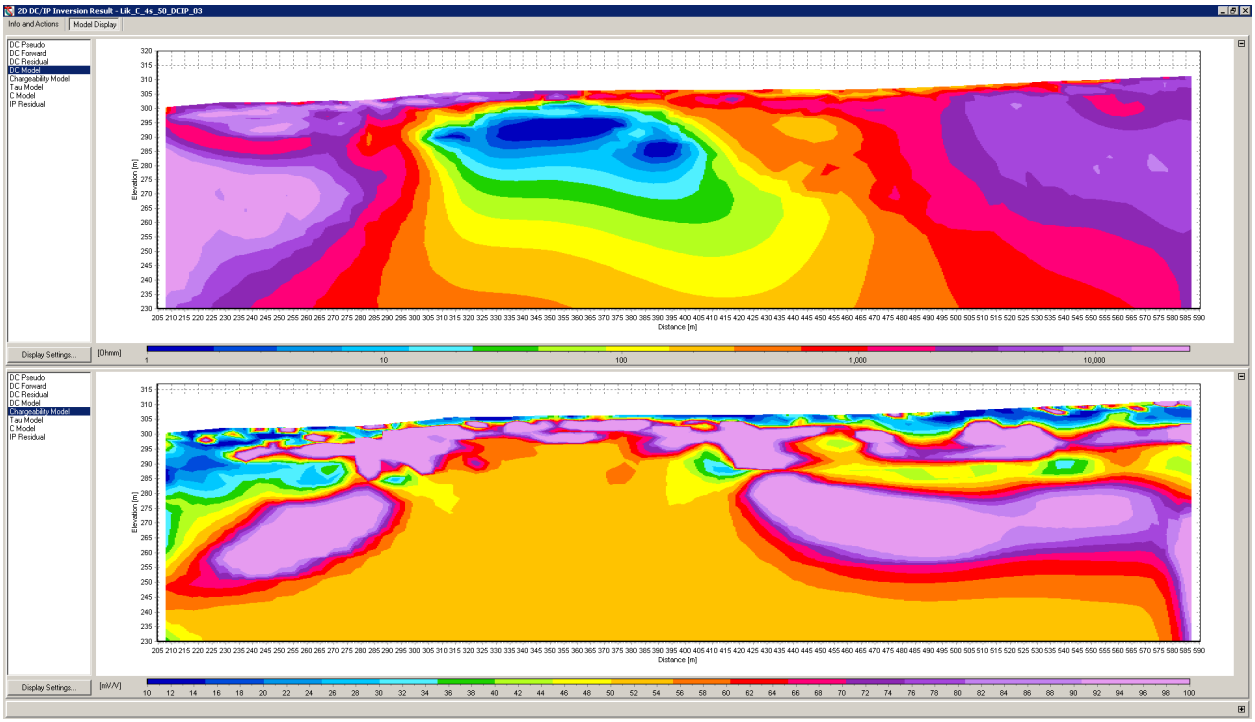

DC Residual: 5.7 IP Residual:3.11

Tau and C modeling

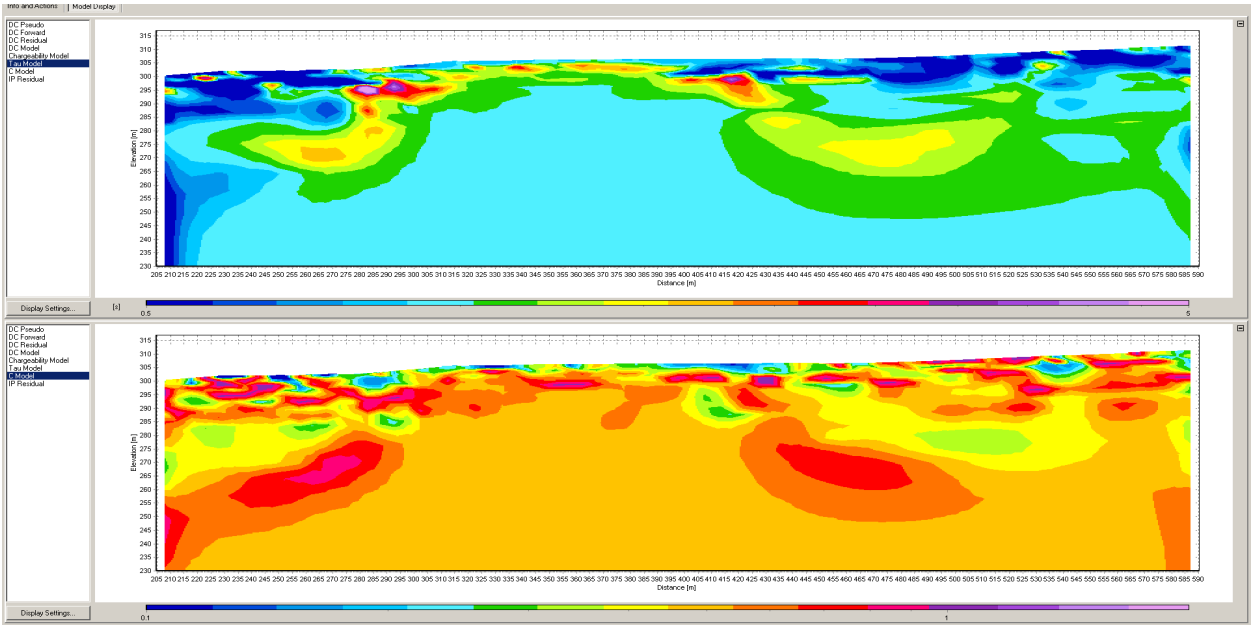

D—Separate spread , IP 4s, 100% duty cycle waveform, Profile length: 405m

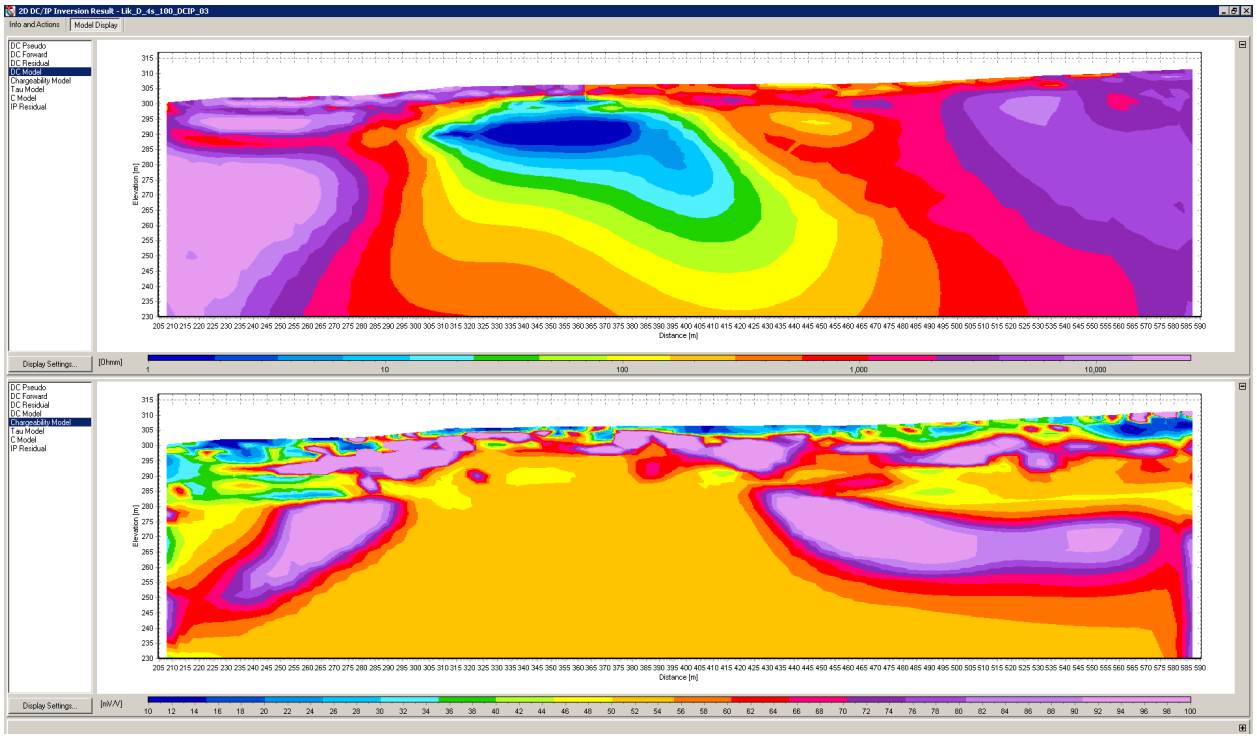

DC Residual: 6.25 IP Residual: 2.92

Tau and C models:

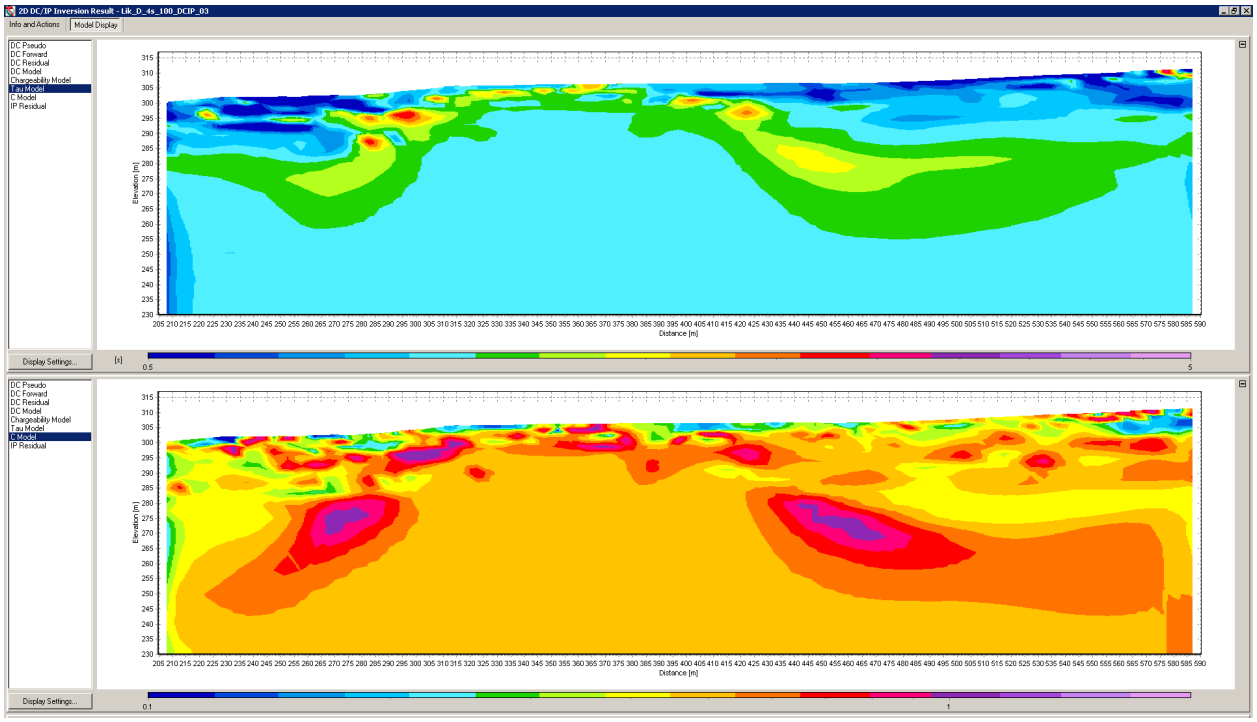

E—Separate spread , IP 2s, 50% duty cycle waveform, Profile length: 405m

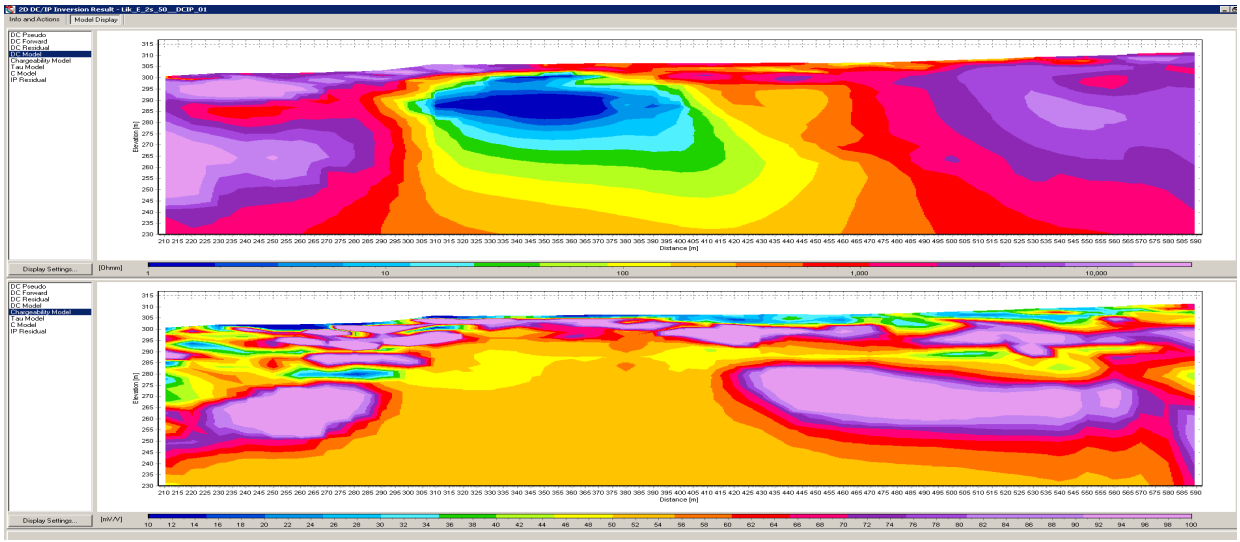

DC Residual: 9.93 IP Residual: 2.76

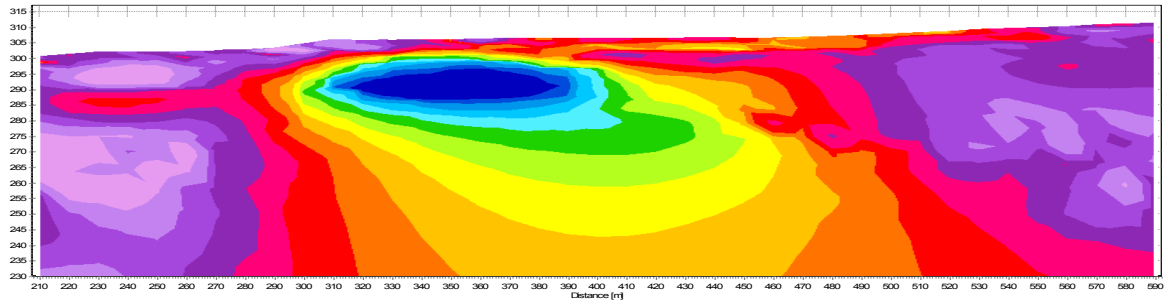

With auto filtering: max slope:1.5 ,deleting negative IP curves and DC STD :1.05 / DC Residual :4.27

Tau and C models

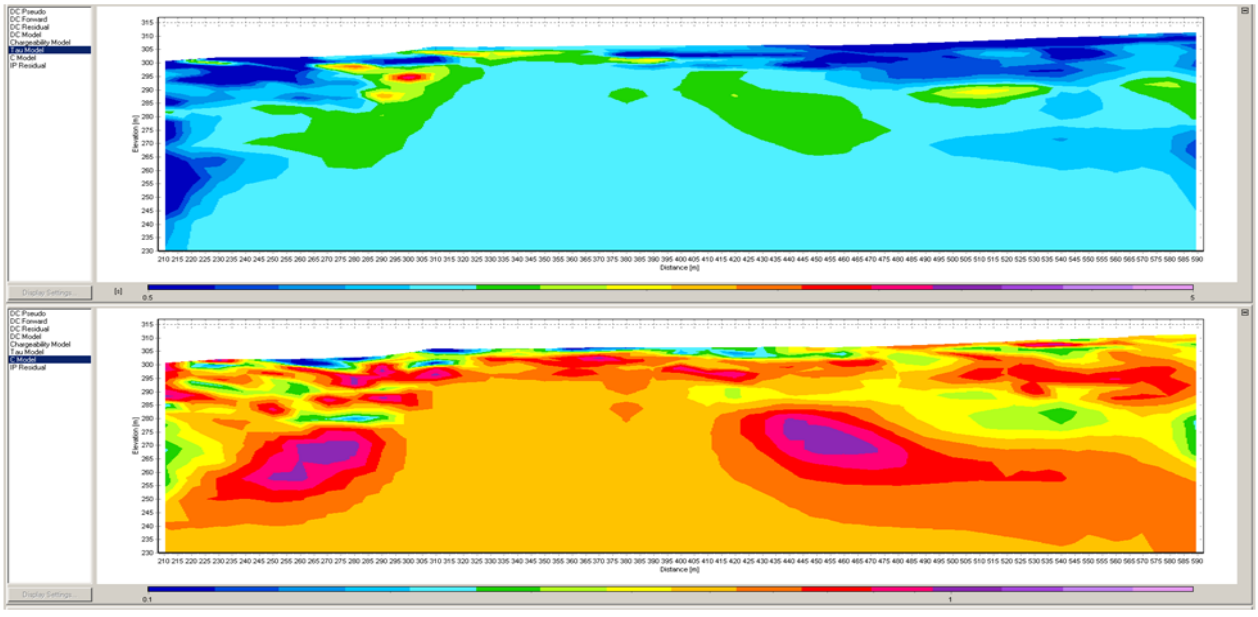

I - Separate spread , IP 2s, 100% duty cycle waveform, Profile length: 405m

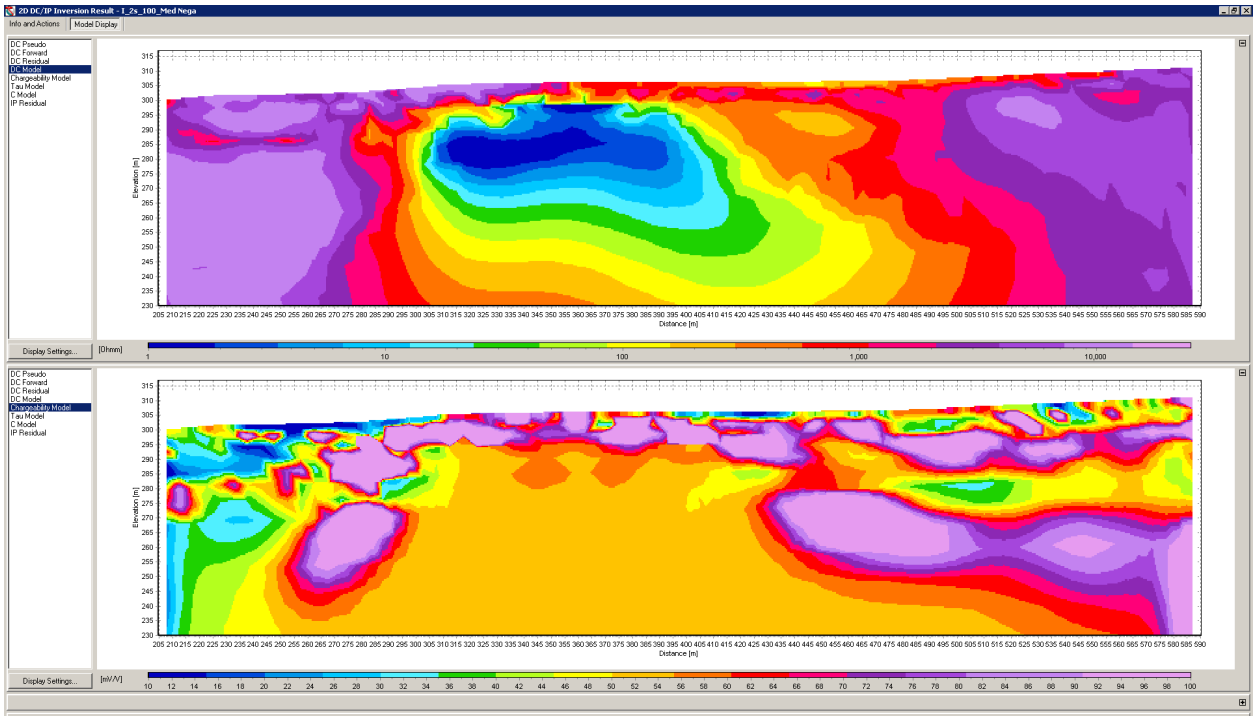

DC Residual: 7.65 IP Residual: 2.95 (With negative IP curves)

Tau and C models:

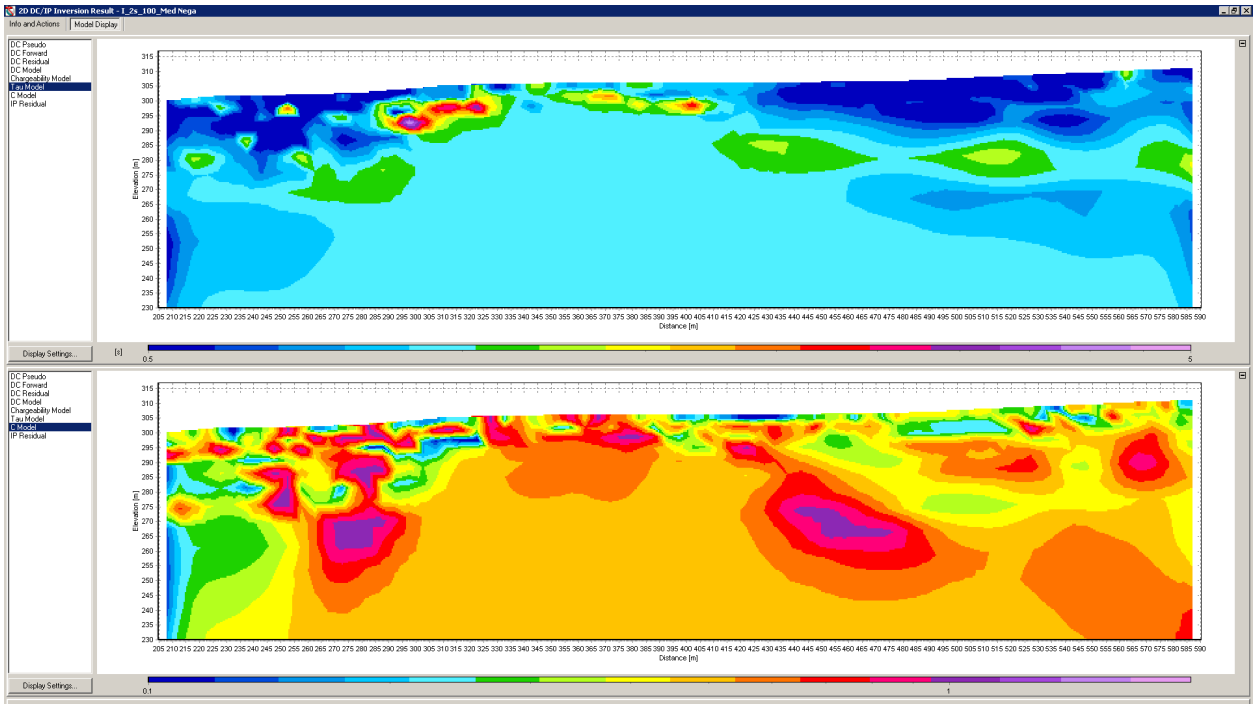

F—Separate spread , IP 1s, 50% duty cycle waveform, Profile length: 405m

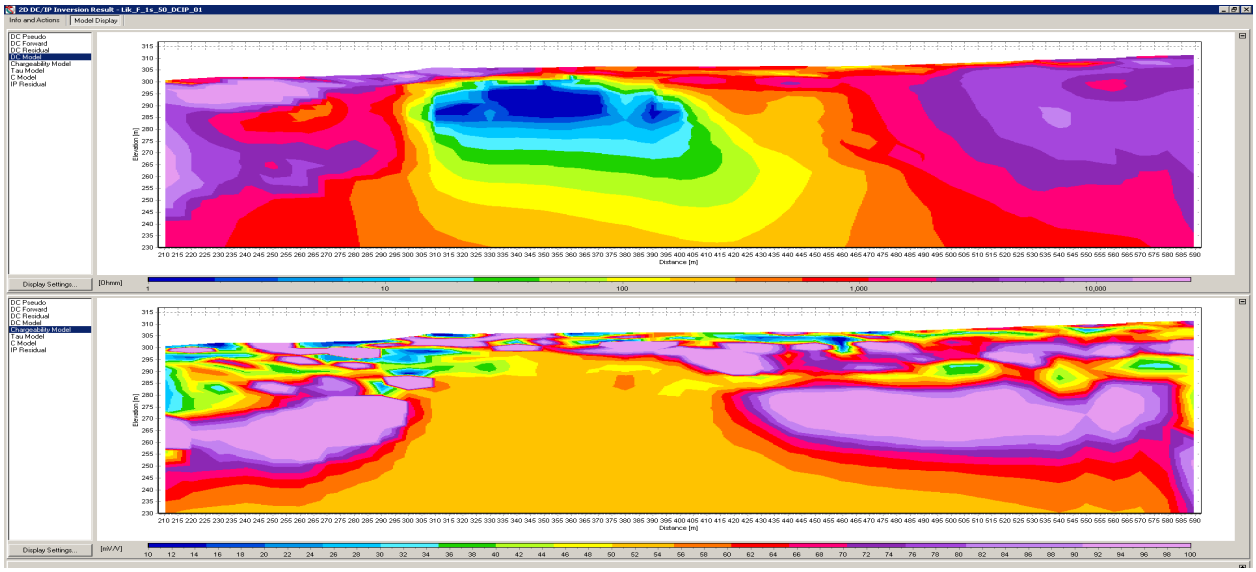

DC Residual: 10.97 IP Residual: 3.49

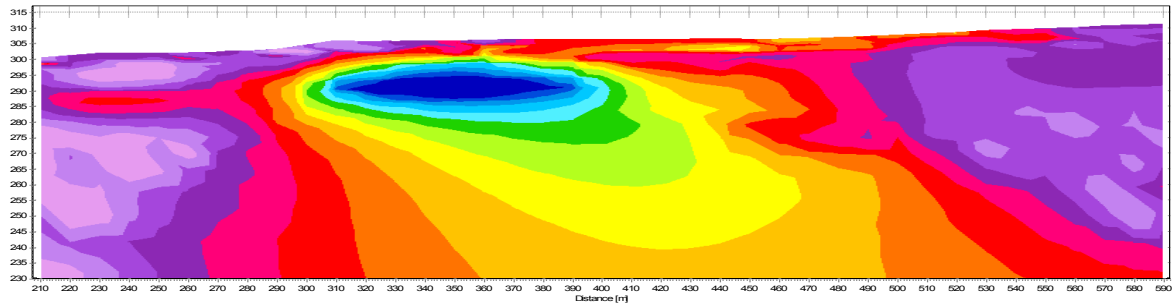

Auto filtering was applied: max slope: 1.5, deleted negative IP curves and DC STD :1.06 / DC Residual: 3.4

Tau and C models:

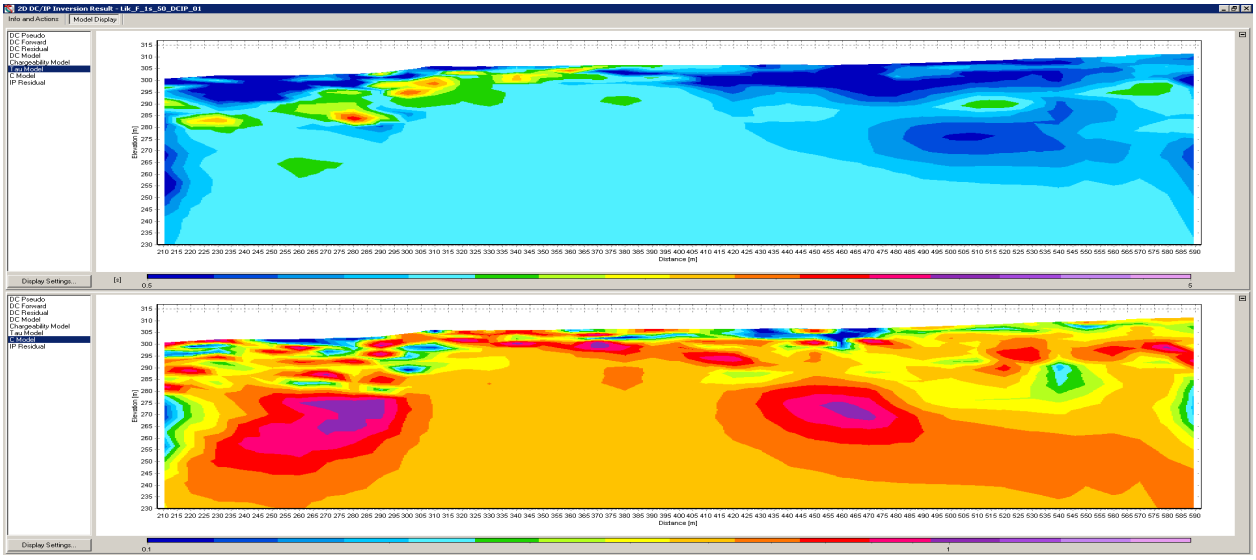

J—Separate spread , 1s, 100% duty cycle waveform, Profile length: 405m

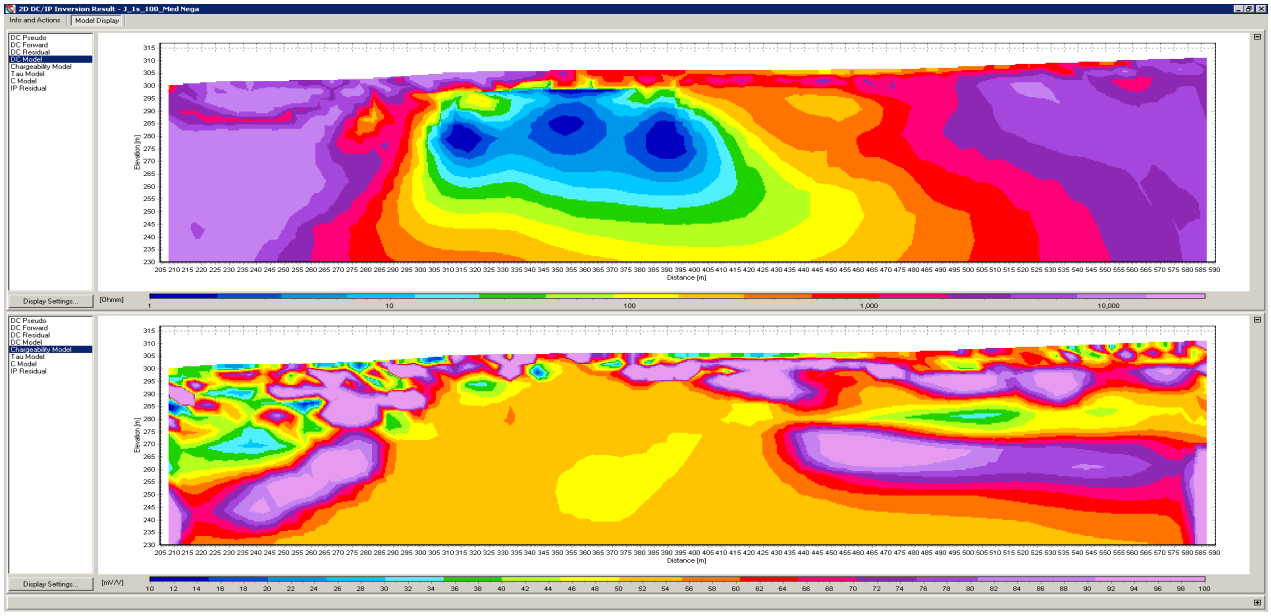

DC Residual: 7.56 IP Residual: 4.19 (with negative IP curves)

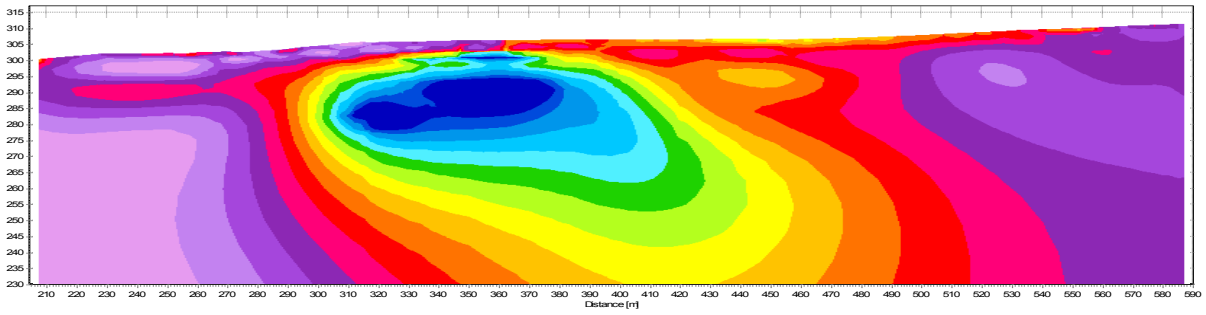

Auto filtering was applied: max slope 3, Keeping negative IP curves and DC STD :1.05 / DC Residual: 2

Tau and C modeling

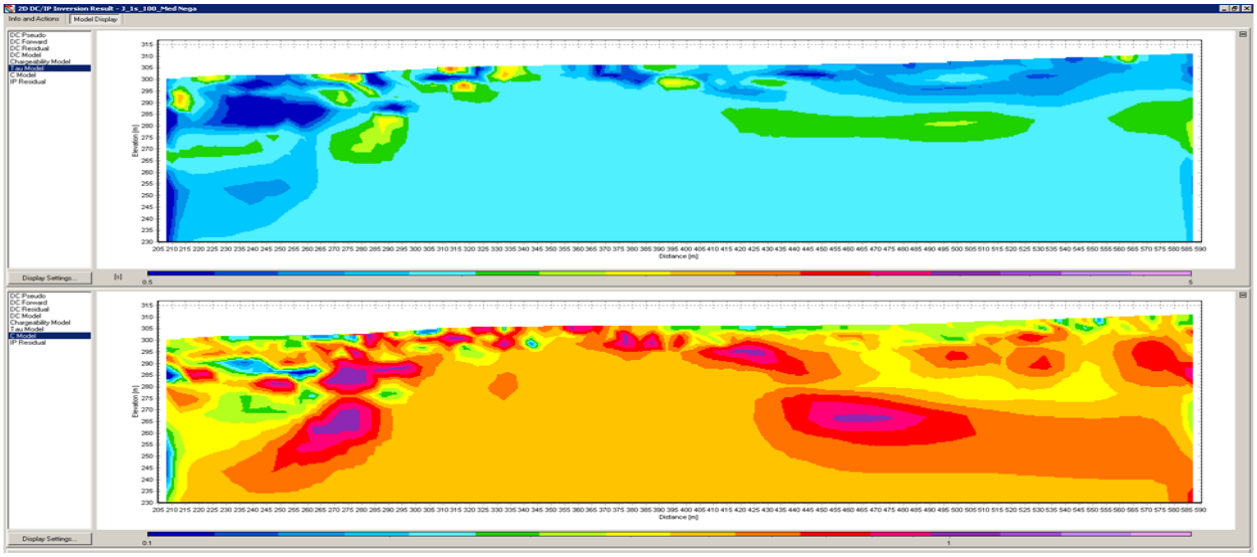

11.3.2.3 Pole Dipole array – Single spread

PD1 - 2s – single- 50% duty cycle waveform, Profile length: 400m

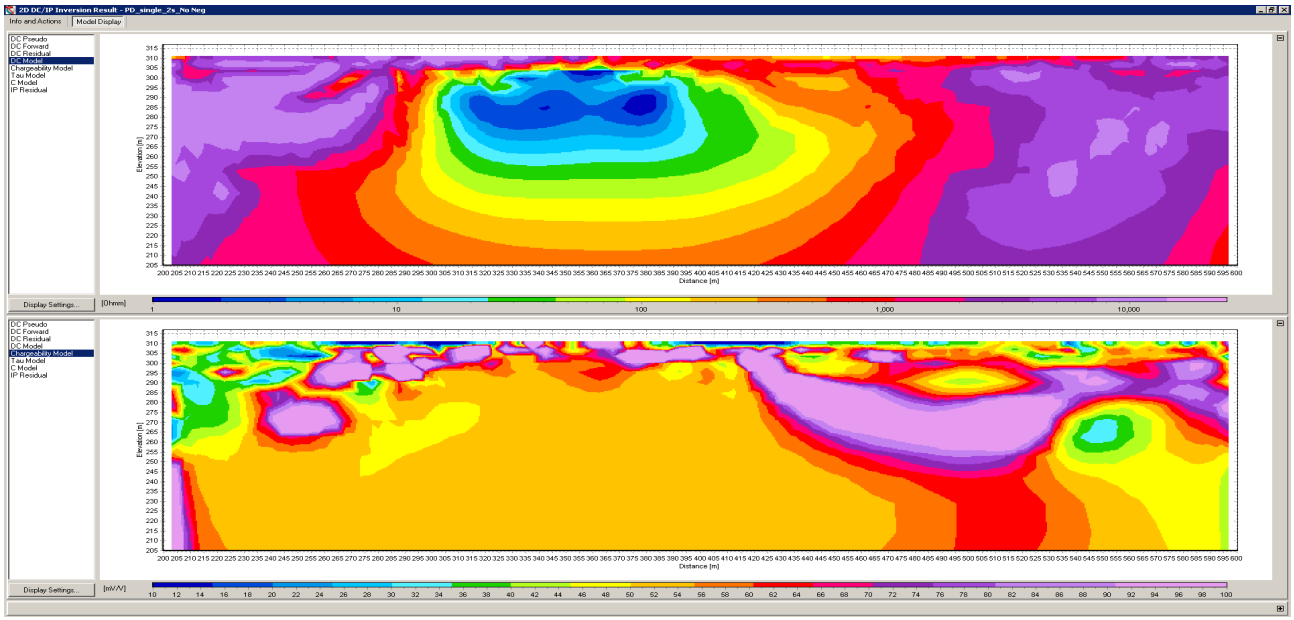

DC Residual: 7.75 IP Residual: 2.34 (No negative IP curves)

Tau and C model

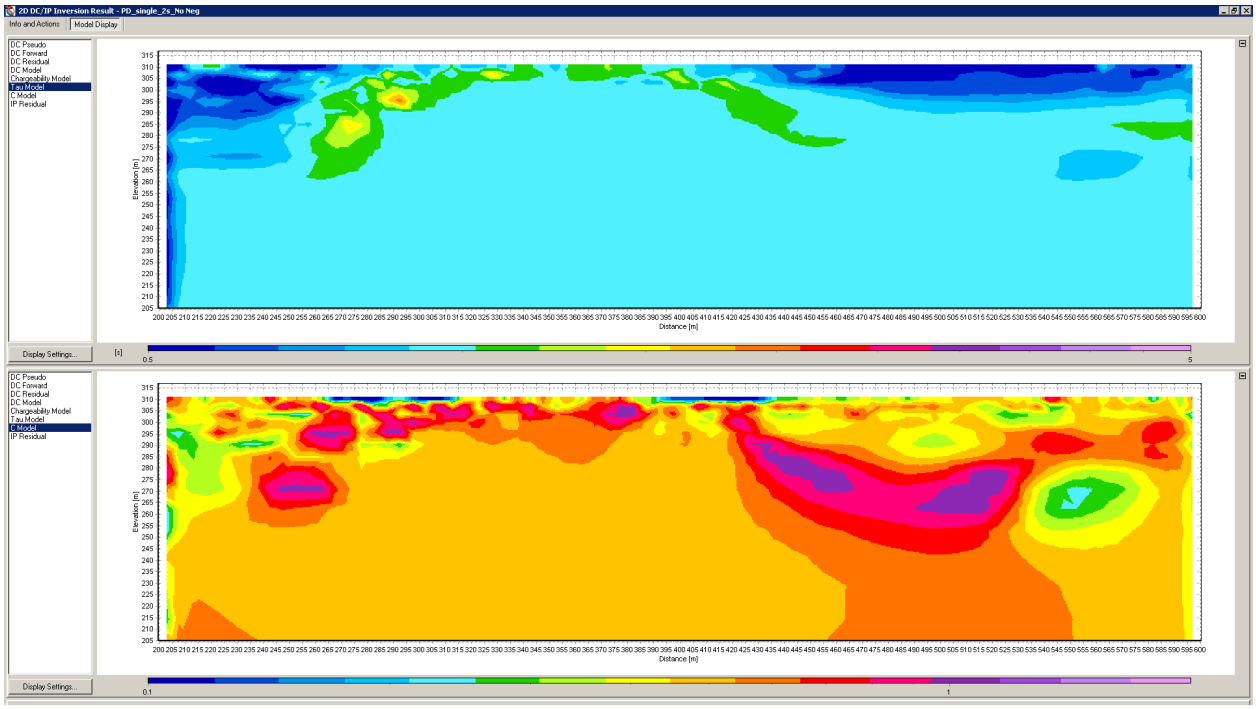

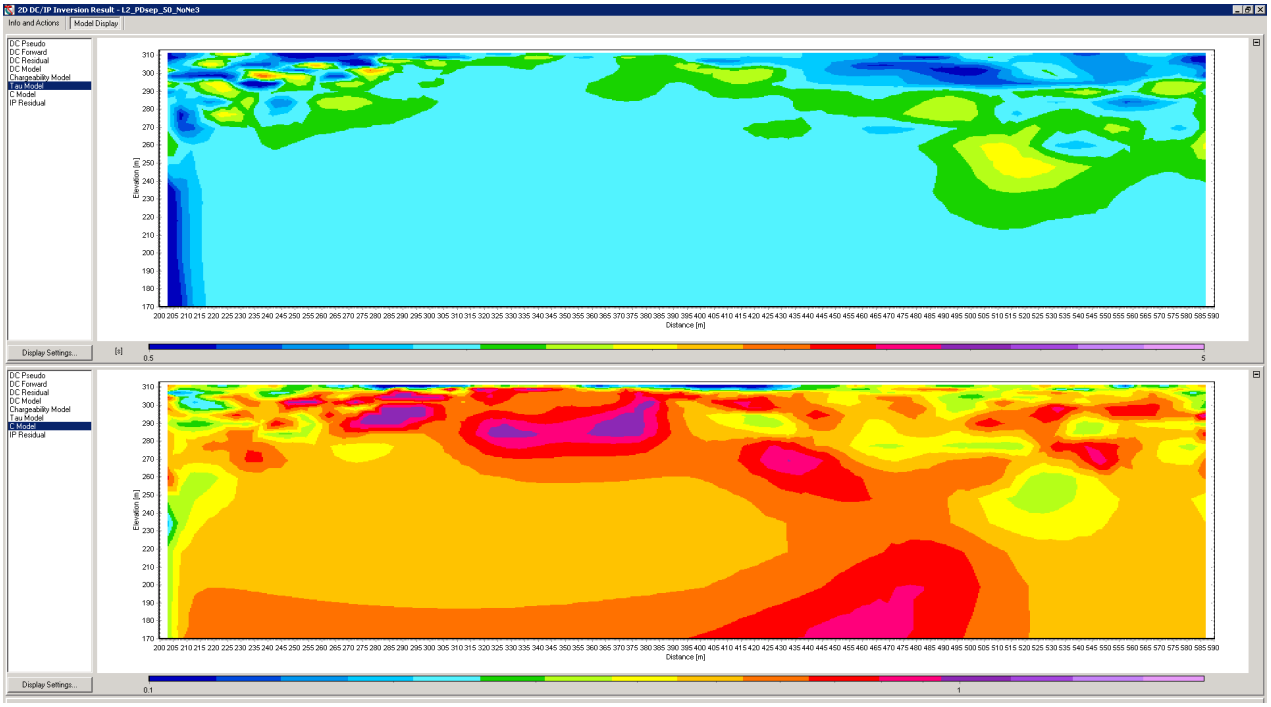
2D DC/IP Inversion Result - L2_PDsep_S0_NoNe3
Info and Actions
Model Display
DC Pseudo
DC Forward
DC Residual
DC Model
Chargeability Model
Tau Model
C Model
IP Residual
Display Settings...
Elevation [m]
Distance [m]
[s]
0.5
5
0.1
1

PD 3- 2s- separate- 100% duty cycle waveform, Profile length: 405m

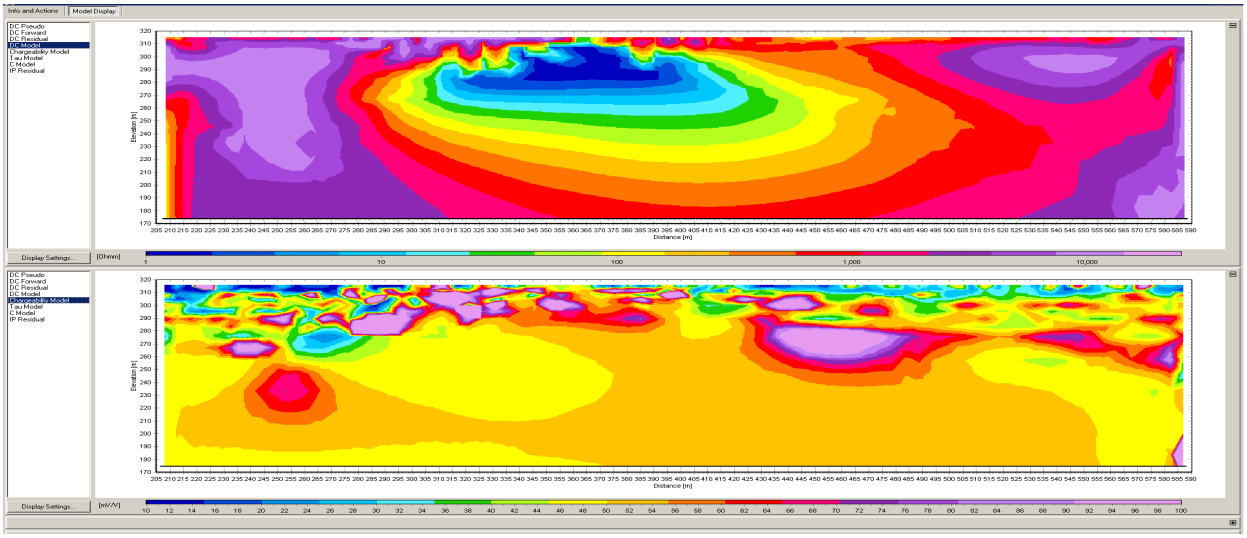

DC: 12.45 IP :3.47 (With negative IP curves)

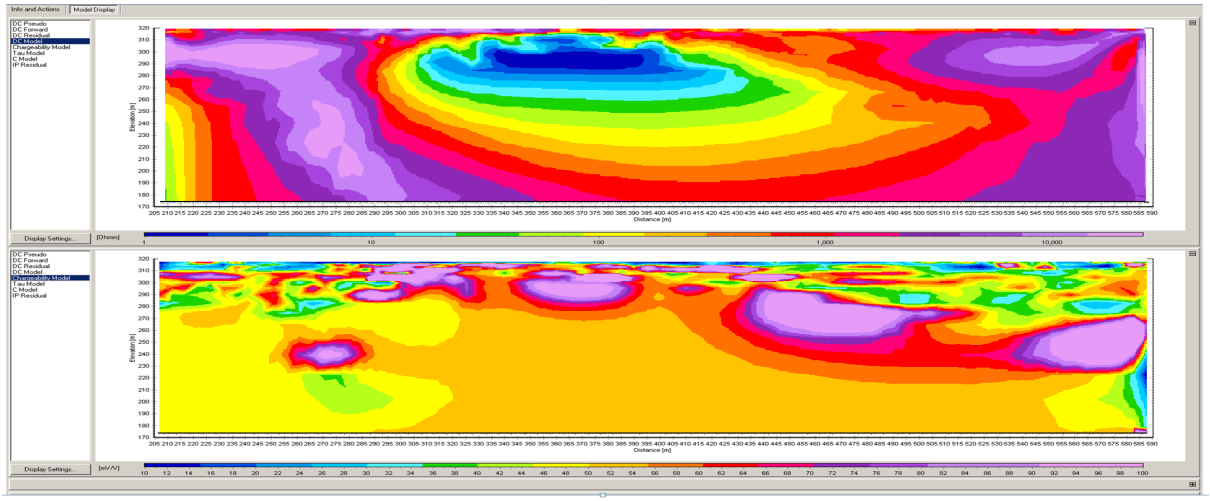

DC: 8.28 IP :2.76 (without negative IP curves)

Tau and C models

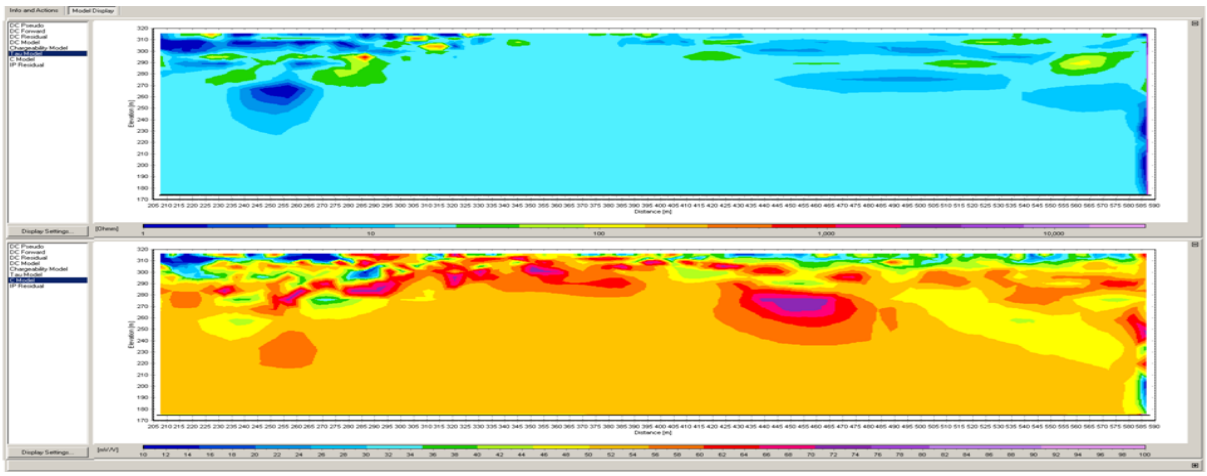

11.4 Pseudosections

11.4.1 Gradient array – 50% duty cycle waveform

Profile A:

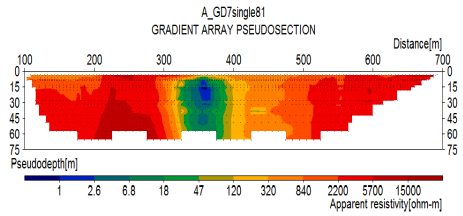

Data file: Lik_A_700m_Rec2_All

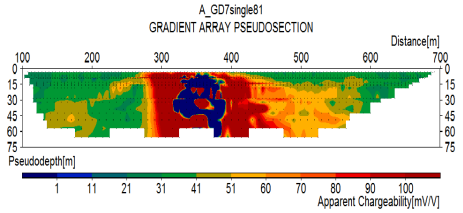

Data file: Lik_A_700m_Rec2_All

Profile B:

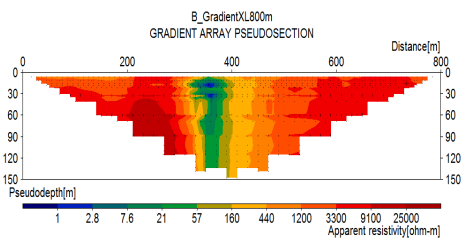

Data file: LIIKA_B_XL800m_PoALL

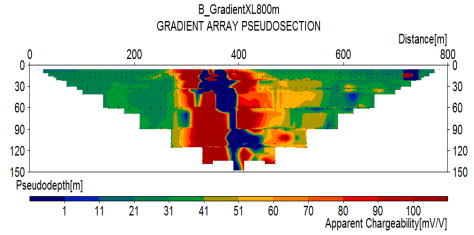

Data file: LIIKA_B_XL800m_PoALL

Profile C:

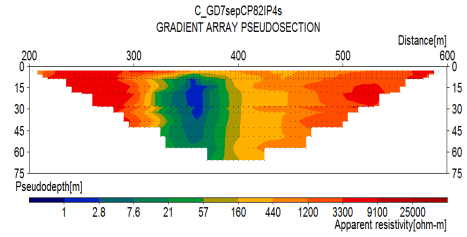

Data file: Lik_C_IP4s_Rec2_All

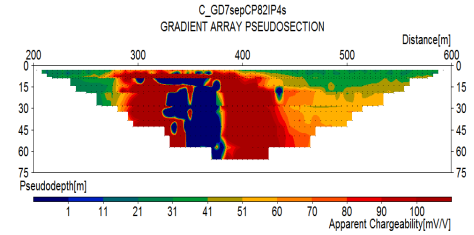

Data file: Lik_C_IP4s_Rec2_All

Profile E:

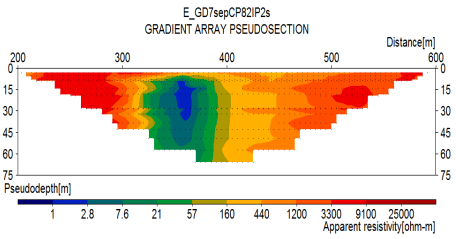

Data file: Lik_E_IP2s_Rec2_All

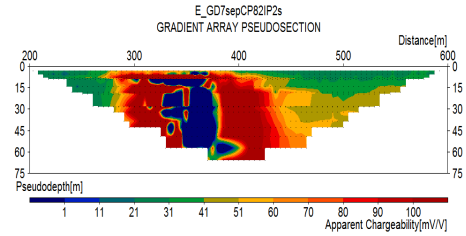

Data file: Lik_E_IP2s_Rec2_All

profile F

ERIGRAPH - ABEM Instrument AB

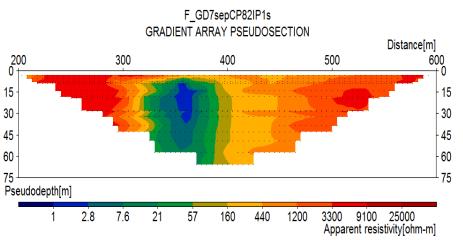

Data file: Lik_F_IP1s_Rec2_All

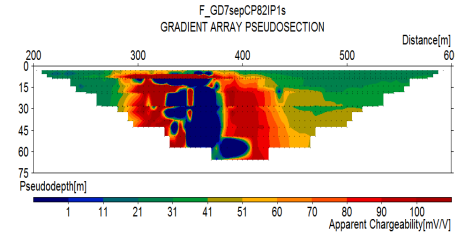

Data file: Lik_F_IP1s_Rec2_All

11.4.2 Gradient array – 100% duty cycle waveform

Profile D:

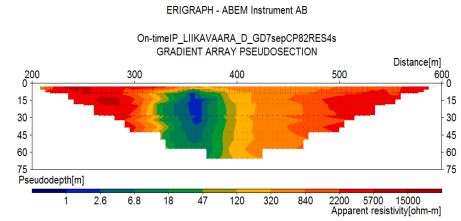

Data file: LIIKAVAARA_D_GD7sepCP82RES4s_separate_ip

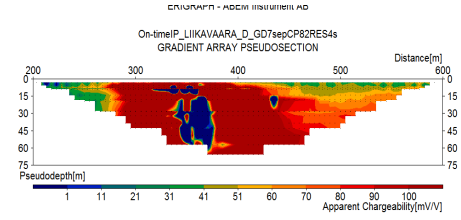

Data file: LIIKAVAARA_D_GD7sepCP82RES4s_separate_ip

Pofile I:

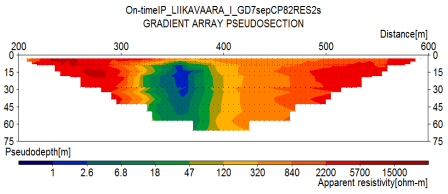

Data file: LIIKAVAARA_I_GD7sepCP82RES2s_separate_ip

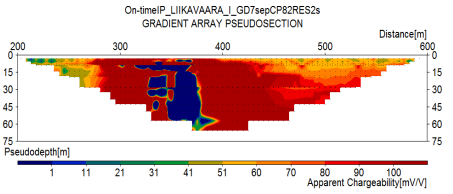

Data file: LIIKAVAARA_I_GD7sepCP82RES2s_separate_ip

Profile J:

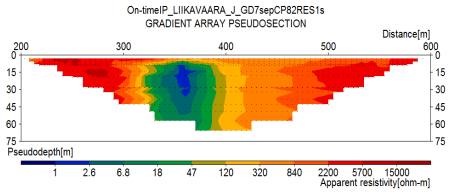

Data file: LIIKAVAARA_J_GD7sepCP82RES1s_separate_ip

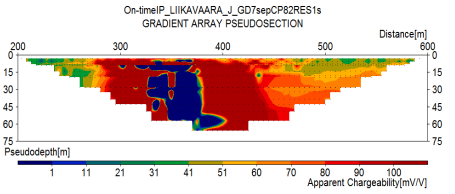

Data file: LIIKAVAARA_J_GD7sepCP82RES1s_separate_ip

11.4.3 Pole-dipole - 50% duty cycle waveform

PDsep-50%

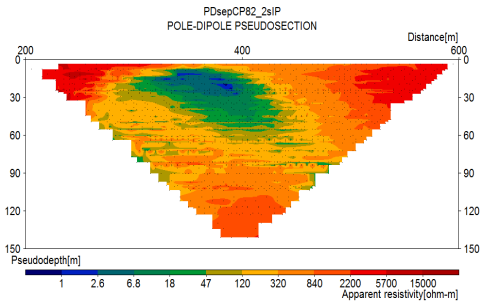

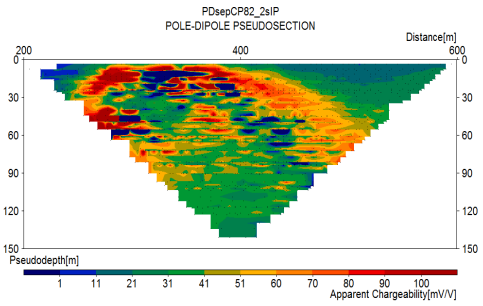

PDsingle-50%

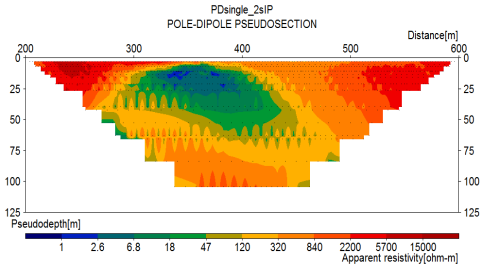

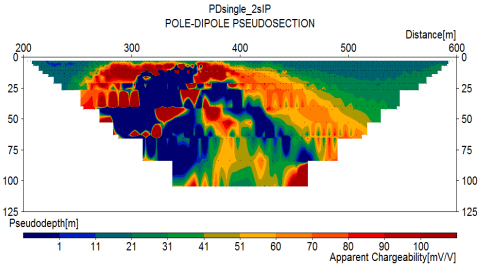

11.4.4 Pole-dipole - 100% duty cycle waveform

PDsep-100%

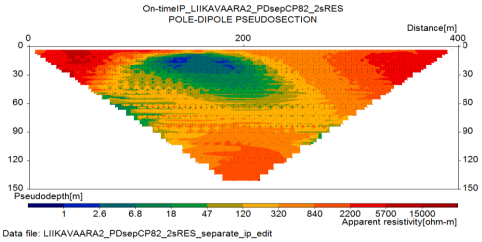

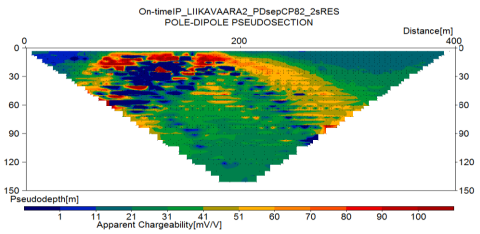

11.5 Table of UTM X coordinates and the local coordinates

Table 15. UTM X coordinates and the corresponding local coordinates (m) on the survey line.

UTM X	Local (m)	UTM X	Local (m)	UTM X	Local (m)
1727347	0	1727613	280	1727875	560
1727356	10	1727622	290	1727884	570
1727366	20	1727631	300	1727893	580
1727376	30	1727640	310	1727903	590
1727385	40	1727650	320	1727912	600
1727395	50	1727659	330	1727922	610
1727404	60	1727668	340	1727931	620
1727415	70	1727677	350	1727941	630
1727424	80	1727687	360	1727950	640
1727434	90	1727696	370	1727960	650
1727444	100	1727706	380	1727969	660
1727454	110	1727716	390	1727978	670
1727463	120	1727725	400	1727987	680
1727472	130	1727735	410	1727996	690
1727482	140	1727744	420	1728005	700
1727491	150	1727753	430	1728015	710
1727500	160	1727763	440	1728024	720
1727510	170	1727772	450	1728033	730
1727519	180	1727781	460	1728043	740
1727529	190	1727790	470	1728053	750
1727538	200	1727800	480	1728062	760
1727548	210	1727809	490	1728071	770
1727557	220	1727818	500	1728080	780
1727566	230	1727828	510	1728090	790
1727575	240	1727837	520	1728100	800
1727584	250	1727847	530		
1727594	260	1727857	540		

Tidigare skrifter i serien ”Examensarbeten i Geologi vid Lunds universitet”:

385. Adolfsson, Max, 2014: Visualizing the volcanic history of the Kaapvaal Craton using ArcGIS. (15 hp)
386. Hajny, Casandra, 2014: Ett mystiskt ryggradsdjursfossil från Åsen och dess koppling till den skånska, krittida ryggradsdjursfaunan. (15 hp)
387. Ekström, Elin, 2014: – Geologins betydelse för geotekniker i Skåne. (15 hp)
388. Thuresson, Emma, 2014: Systematisk sammanställning av större geoenergianläggningar i Sverige. (15 hp)
389. Redmo, Malin, 2014: Paleontologiska och impaktrelaterade studier av ett anomalt lerlager i Schweiz. (15 hp)
390. Artursson, Christopher, 2014: Comparison of radionuclide-based solar reconstructions and sunspot observations the last 2000 years. (15 hp)
391. Svahn, Fredrika, 2014: Traces of impact in crystalline rock – A summary of processes and products of shock metamorphism in crystalline rock with focus on planar deformation features in feldspars. (15 hp)
392. Järvin, Sara, 2014: Studie av faktorer som påverkar skredutbredningen vid Norsälven, Värmland. (15 hp)
393. Åberg, Gisela, 2014: Stratigrafin i Hanöbukten under senaste glaciationen: en studie av borrkärnor från IODP’s expedition nr 347. (15 hp)
394. Westlund, Kristian, 2014: Geomorphological evidence for an ongoing transgression on northwestern Svalbard. (15 hp)
395. Rooth, Richard, 2014: Uppföljning av utlastningsgrad vid Dannemora gruva; april 2012 - april 2014. (15 hp)
396. Persson, Daniel, 2014: Miljögeologisk undersökning av deponin vid Getabjär, Sölvesborg. (15 hp)
397. Jennerheim, Jessica, 2014: Undersökning av långsiktiga effekter på mark och grundvatten vid infiltration av lakvatten – fältundersökning och utvärdering av förhållanden vid Kejsarkullens avfallsanläggning, Hultsfred. (15 hp)
398. Särman, Kim, 2014: Utvärdering av befintliga vattenskyddsområden i Sverige. (15 hp)
399. Tuvesson, Henrik, 2014: Från hav till land – en beskrivning av geologin i Skrylle. (15 hp)
400. Nilsson Brunlid, Anette, 2014: Paleoekologisk och kemisk-fysikalisk undersökning av ett avvikande sedimentlager i Barsebäcks mosse, sydvästra Skåne, bil dat för ca 13 000 år sedan. (15 hp)
401. Falkenhaug, Jorunn, 2014: Vattnets kretslopp i området vid Lilla Klåveröd: ett kunskapsprojekt med vatten i fokus. (15 hp)
402. Heingård, Miriam, 2014: Long bone and vertebral microanatomy and osteohistology of ’Platecarpus’ ptychodon (Reptilia, Mosasauridae) – implications for marine adaptations. (15 hp)
403. Kall, Christoffer, 2014: Microscopic echinoderm remains from the Darriwilian (Middle Ordovician) of Västergötland, Sweden – faunal composition and applicability as environmental proxies. (15 hp)
404. Preis Bergdahl, Daniel, 2014: Geoenergi för växthusjordbruk – Möjlig anläggning av värme och kyla i Västskåne. (15 hp)
405. Jakobsson, Mikael, 2014: Geophysical characterization and petrographic analysis of cap and reservoir rocks within the Lund Sandstone in Kyrkheddinge. (15 hp)
406. Björnfors, Oliver, 2014: A comparison of size fractions in faunal assemblages of deep-water benthic foraminifera—A case study from the coast of SW-Africa.. (15 hp)
407. Rådman, Johan, 2014: U-Pb baddeleyite geochronology and geochemistry of the White Mfolozi Dyke Swarm: unravelling the complexities of 2.70-2.66 Ga dyke swarms on the eastern Kaapvaal Craton, South Africa. (45 hp)
408. Andersson, Monica, 2014: Drumliner vid moderna glaciärer — hur vanliga är de? (15 hp)
409. Olsenius, Björn, 2014: Vinderosion, sanddrift och markanvändning på Kristianstadsslätten. (15 hp)
410. Bokhari Friberg, Yasmin, 2014: Oxygen isotopes in corals and their use as proxies for El Niño. (15 hp)
411. Fullerton, Wayne, 2014: REE mineralisation and metasomatic alteration in the Olserum metasediments. (45 hp)
412. Mekhaldi, Florian, 2014: The cosmic-ray events around AD 775 and AD 993 - Assessing their causes and possible effects on climate. (45 hp)
413. Timms Eliasson, Isabelle, 2014: Is it pos-

sible to reconstruct local presence of pine on bogs during the Holocene based on pollen data? A study based on surface and stratigraphical samples from three bogs in southern Sweden. (45 hp)

414. Hjulström, Joakim, 2014: Bortforsling av kaxblandat vatten från borrningar via dagvattenledningar: Riskanalys, karaktärisering av kaxvatten och reningsmetoder. (45 hp)
415. Fredrich, Birgit, 2014: Metadolerites as quantitative P-T markers for Sveconorwegian metamorphism, SW Sweden. (45 hp)
416. Alebouyeh Semami, Farnaz, 2014: U-Pb geochronology of the Tsineng dyke swarm and paleomagnetism of the Hartley Basalt, South Africa – evidence for two separate magmatic events at 1.93-1.92 and 1.88-1.84 Ga in the Kalahari craton. (45 hp)
417. Reiche, Sophie, 2014: Ascertaining the lithological boundaries of the Yoldia Sea of the Baltic Sea – a geochemical approach. (45 hp)
418. Mroczek, Robert, 2014: Microscopic shock-metamorphic features in crystalline bedrock: A comparison between shocked and unshocked granite from the Siljan impact structure. (15 hp)
419. Balija, Fisnik, 2014: Radon ett samhällsproblem - En litteraturstudie om geologiskt sammanhang, hälsoeffekter och möjliga lösningar. (15 hp)
420. Andersson, Sandra, 2014: Undersökning av kalciumkarbonatförekomsten i infiltrationsområdet i Sydvattens vattenverk, Vombverket. (15 hp)
421. Martin, Ellinor, 2014: Chrome spinel grains from the Komstad Limestone Formation, Killeröd, southern Sweden: A high-resolution study of an increased meteorite flux in the Middle Ordovician. (45 hp)
422. Gabrielsson, Johan, 2014: A study over Mg/Ca in benthic foraminifera sampled across a large salinity gradient. (45 hp)
423. Ingvaldson, Ola, 2015: Ansvarsutredningar av tre potentiellt förorenade fastigheter i Helsingborgs stad. (15 hp)
424. Robygd, Joakim, 2015: Geochemical and palaeomagnetic characteristics of a Swedish Holocene sediment sequence from Lake Storsjön, Jämtland. (45 hp)
425. Larsson, Måns, 2015: Geofysiska undersökningsmetoder för geoenergisystem. (15 hp)
426. Hertzman, Hanna, 2015: Pharmaceuticals in groundwater - a literature review. (15 hp)
427. Thulin Olander, Henric, 2015: A contribution to the knowledge of Fårö's hydrogeology. (45 hp)
428. Peterffy, Olof, 2015: Sedimentology and carbon isotope stratigraphy of Lower–Middle Ordovician successions of Slemmestad (Oslo-Asker, Norway) and Brunflo (Jämtland, Sweden). (45 hp)
429. Sjunnesson, Alexandra, 2015: Spårämnesförsök med nitrat för bedömning av spridning och uppehållstid vid återinfiltrationav grundvatten. (15 hp)
430. Henao, Victor, 2015: A palaeoenvironmental study of a peat sequence from Iles Kerguelen (49° S, Indian Ocean) for the Last Deglaciation based on pollen analysis. (45 hp)
431. Landgren, Susanne, 2015: Using calcein-filled osmotic pumps to study the calcification response of benthic foraminifera to induced hypoxia under *in situ* conditions: An experimental approach. (45 hp)
432. von Knorring, Robert, 2015: Undersökning av karstvittring inom Kristianstadsslättens NV randområde och bedömning av dess betydelse för grundvattnets sårbarhet. (30 hp)
433. Rezvani, Azadeh, 2015: Spectral Time Domain Induced Polarization - Factors Affecting Spectral Data Information Content and Applicability to Geological Characterization. (45 hp)

LUNDS UNIVERSITET

Geologiska institutionen
Lunds universitet
Sölvegatan 12, 223 62 Lund